SOLVENT AND STRUCTURAL EFFECTS ON ELECTRON TRANSFER IN INTERMOLECULAR CHARGE-TRANSFER COMPLEXES AND PHOTOEXCITED ORGANOSILANES

by
Brandon J. Barrett

A dissertation submitted to Johns Hopkins University in conformity with the requirements for the degree of Doctor of Philosophy

Baltimore, Maryland
June 2022

Abstract

Understanding how molecular structure and local chemical environment impact photoinduced charge transfer and the stability of donor-acceptor charge-transfer complexes is critical for controlling the formation and separation of charge pairs for applications relevant in the field of optoelectronics. The first part of this thesis discusses solvent effects on the formation of charge transfer complexes (CTC) between a fluorinated quinone acceptor and a phenylenediamine donor that results from integer charge transfer (ICT). Utilizing temperature dependent steady-state UV-Vis, we demonstrate charge separation is favorable and strongly supported in moderately polar solvent environments where ion-pair interactions aid in stabilizing complexes. Spontaneous charge separation is still observed (but is less favorable) for lower polarity solvents where charge separation is still entropically favored. These results provide insight for forming and supporting integer charge separation in environments characterized by low dielectric constants, which needs to be considered for applications involving polymer films or devices. The photoresponses of these complexes were characterized via ultrafast transient absorption spectroscopy to compare CTC photo-physics and photo-dynamics in solution phase and doped polymer films. These experiments reveal that the radical anion of the acceptor dominates the transient dynamics, with anion excited-state relaxation in solution involving rapid internal conversion to a vibrationally hot ground state. Doped polymer films are shown to support both ICT and partial charge transfer states (PCT) upon film drying. Transient responses follow the same relaxation mechanism but on faster timescales where it is concluded these complexes introduce photon losses in working materials due to rapid relaxation.

The second part of this thesis presents studies of intramolecular charge separation in hybrid σ-π organosilane molecules and how this process depends on solvent environment and chemical

structure. We have previously characterized the photophysics of a series of ester, cyanovinyl capped organosilanes which have an optical σ-π* intramolecular charge transfer transition. Charge recombination was shown to occur in the Marcus inverted region where recombination rates follow a gap-law behavior. Using transient absorption spectroscopy, charge-transfer dynamics were characterized for organosilanes consisting of di-ester and di-cyano vinyl acceptor units with weak vs. strong electron accepting ability, respectively. We find the strength of the electron acceptor governs whether electronic coupling (rather than thermodynamic driving force) will dictate the rate of charge recombination. Weak acceptors result in fast recombination in moderately polar solvents, whereas strong acceptors better stabilize photoinduced charge separation and prolonged lifetimes are observed. The charge separation lifetime in the strongest donor-acceptor pairing can be further extended in low polarity solvents with low reorganization energy, as this places back-electron transfer deeper into the Marcus inverted region. However, for weak to moderate donor-acceptor structures, this results in larger electronic couplings where very rapid recombination approaches the adiabatic limit. Collectively these findings aid in the understanding of the structure-function relationships and the role chemical environment plays for controlling charge separation in organosilanes.

Advisor: Dr. Arthur E. Bragg

Thesis Committee: Dr. Thomas J. Kempa

Dr. Paul Dagdigian

Acknowledgments

To my family and friends who helped make this possible and supported me through my educational career.

Contents

List of Tables

List of Figures

List of Schemes

Chapter 1

Introduction

1.1 Overview of Charge Transfer in Materials

Donor-Acceptor molecules or materials which can undergo charge separation in their ground or excited states have been of interest for broad application in the field of optoelectronics. For example, strong electron donating or accepting species can be paired for intermolecular ground state charge transfer (i.e. integer charge transfer forming charge separated ion pairs) which is critical for doping organic semiconductors to improve charge carrier densities and device performances. Furthermore, donor-acceptor molecules that undergo photoinduced charge-transfer have been utilized in organic photovoltaics where the associated charge transfer states play a vital role in charge separation and transfer for light-harvesting applications. Molecular materials that exhibit intramolecular photoinduced charge transfer have found applications as two-photon absorbers, nonlinear optical materials, or as chemical components in various architectures of other optoelectronic materials. The photoresponsive properties of these materials are often connected with charge-separation lifetimes that can be tuned through structure or local chemical environment.

Developing a better understanding of what controls formation of charge-separated states and how to control the lifetime of charge separation is critical to improving performance in the various material applications mentioned above. Characterization of this type requires applications of steady-state and time-resolved optical spectroscopies to interrogate these properties related to charge transfer. The work described in this thesis focuses on two separate classes of electron donor-acceptor systems. The first parts describe studies of formation and stability of intermolecular charge transfer complexes between a strong quinone acceptor and phenylamine donor as well as the associated ultrafast photodynamics of the resultant charge-transfer complex.

The second part to this thesis discusses the photodynamics of a novel class of organosilane which exhibits intramolecular charge transfer upon photoexcitation; this work presents how molecular structure and chemical environment can be used to control charge recombination dynamics in these species. The following parts of this chapter provide a brief overview of relevant background for studies of these materials.

1.2 Fundamentals of Photoinduced Dynamics

1.2.1 Overview of Light Absorption, Transition Dipoles, and Photoinduced Relaxation Pathways

Understanding the principles of light-matter interactions and subsequent relaxation processes is critical for characterizing photo-induced dynamics in photo-responsive materials. This section overviews the requirements for a molecule to absorb a photon and the various relaxation mechanisms that can occur in order to release the energy imparted through photoexcitation.

To begin we will consider absorption of ultraviolet (UV) and visible energy photons through electronic transitions. In order for an interaction (electronic transition) to occur between incident photons and a molecule, there must be a non-zero transition dipole moment to couple two quantum mechanical states. This is expressed in terms of the transition dipole moment operator $\vec{\mu}$:

$$\vec{\mu}_{fi} = \int \psi_f^* \vec{\mu} \psi_i \, d\tau \neq 0 \tag{1.1}$$

where a nonzero product is required between the initial state ψ_i and final state ψ_f for absorption to occur. For dipole-allowed transitions, dipole moments aligned to the polarization of incident light are preferentially excited, where the strength of a transition is dependent on the relative

alignment of electromagnetic field $\vec{E}$ and the transition dipole moment $\vec{\mu}$ and has a $\cos^2\theta$ dependence according to the following:

$$I \propto |\vec{\mu}|^2 \left|\vec{E}\right|^2 \cos^2\theta \tag{1.2}$$

Other factors such as orbital symmetries (which determine electronic transition dipole moments), and Franck-Condon overlaps of vibrational states contribute to the strength of an electronic transition at a given excitation wavelength.

Following the absorption of light, different radiative or non-radiative deactivation processes can occur. Electronic transitions generally populate vibrational levels of the excited state above the state's zero-point energy (vibrationless level); this is generally due to the displacement between potential energy landscapes along one or more nuclear coordinate (will be discussed in terms of Franck-Condon factors below). Relaxation from these initial "hot" excited states involves vibrational cooling (and/or structural reorganization) on a femto- to pico- second timescale. This process lowers the total energy of the systems via a combination of intra and intermolecular vibrational energy transfer, ultimately resulting in heat transfer to surroundings when considering samples in condensed phases and is discussed in later Chapters of this thesis.

Following fast vibrational cooling, a system can proceed to spontaneously release energy from an excited singlet state through the radiative decay process of fluorescence. While not of concern to the studies within this thesis, it is noted that intersystem crossing between an excited singlet and triplet state can occur due to sufficient spin-orbit coupling. These deactivation pathways are also in competition with fast nonradiative processes. Of particular relevance to the work in this thesis is the process of internal conversion, where deactivation occurs via population transfer between electronic states of the same spin multiplicity (i.e. $S_1 \rightarrow S_0$). The rate of internal

conversion is determined by the energy differences (or gap) between the electronic states involved according to the following "gap law":

$$k_{IC} \propto e^{(-\Delta E/h\nu)} \tag{1.3}$$

where h is Planck's constant and ν is the vibrational frequency of energy-accepting vibrational modes. It follows from this relationship that the rate of internal conversion is highest for states that are close in energy. A Jablonski diagram illustrating these various deactivation pathways and associated rates is presented in Figure 1.1.

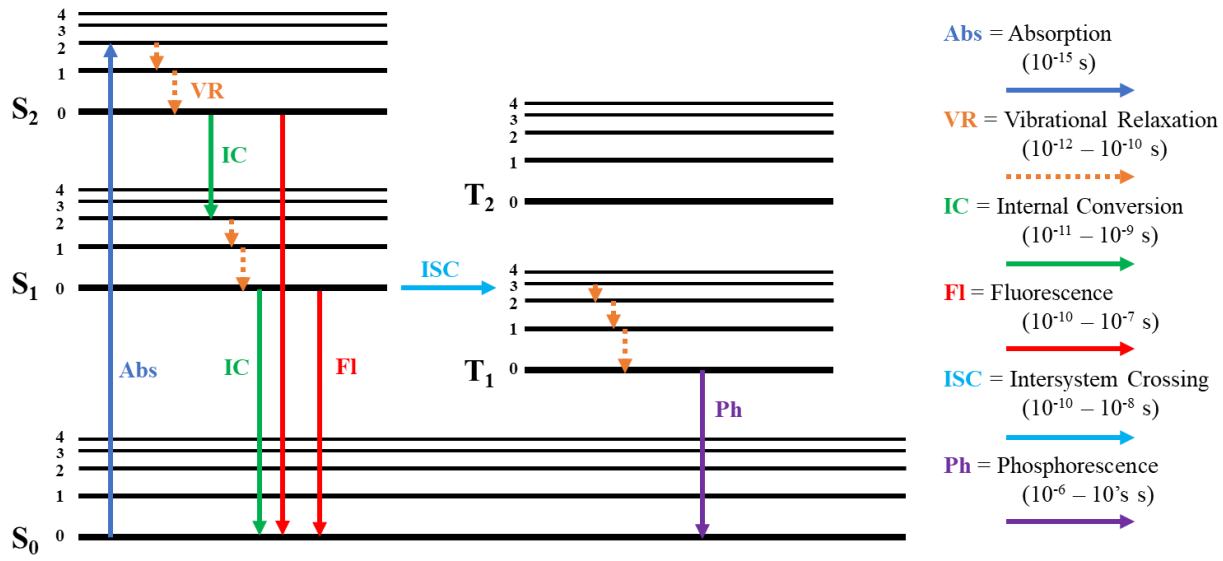

Figure 1.1. Jablonski diagram displaying various excited-state deactivation pathways following the absorption of light.

1.2.2 The Born-Oppenheimer Approximation and Franck-Condon Principle

The prior section viewed absorption and related deactivation energies visually using energy-level descriptions. In order to gain a more quantitative understanding of state energetics for complex potential energy surfaces, we must consider a quantum mechanical treatment of the system in terms of its electronic and nuclear coordinates. This requires the use of the time-independent Schrödinger equation:

$$\hat{H}|\psi(r;R)\rangle = E|\psi(r;R)\rangle \tag{1.4}$$

where E is the eigen solution corresponding to the energy for a specific state of a system represented by the wavefunction $\psi(r;R)$, which is described by its electronic and nuclear coordinates, for the eigen equation involving the Hamiltonian operator $\hat{H}$. For multielectronic molecular systems, the Hamiltonian includes contributions of kinetic and potential energies of the electrons, nuclei, and their interactions according to the following:

$$\hat{H} = \hat{T}_N + \hat{T}_e + \hat{V}_{NN} + \hat{V}_{ee} + \hat{V}_{eN} \tag{1.5}$$

where $\hat{T}$ is the kinetic energy terms for electrons and nuclei (denoted by N and e subscripts), and $\hat{V}$ is the potential energy contributions for interactions between electrons, nuclei, and each other. Exact solution to problems involving multi electrons are not possible analytically and require further simplifications to be invoked in order to approximate potential energy surfaces and related energies of complex systems. The Born-Oppenheimer approximation is therefore introduced which treats electronic and nuclei coordinates separately. The basis for this comes from the fact that electronic and nuclear motion occur on different timescales due to differences in unit mass, where the heavy nuclei may be viewed as stationary on the timescale of fast electronic motion.

The wavefunctions then used in the time independent Schrödinger equation are expressed as:

$$\psi_{n,\nu_n} = \psi_n(r;R)\chi^n_{\nu_n}(R) \tag{1.6}$$

Here ψ_{n,ν_n}, the vibronic wavefunction, is comprised of an electronic wavefunction $\psi_n(r;R)$ that depends solely on the electronic coordinates "r" and is only parameterized by the nuclear coordinates "R", along with the nuclear wavefunctions $\chi^n_{\nu_n}(R)$ which include vibrational and rotational contributions. This separation allows one to solve for electronic wavefunctions in the time-independent Schrödinger Equation with application of the electronic operator of the

Hamiltonian. This provides energy solutions as a function of nuclei positions, which can then be solved at a series of nuclear coordinates to construct the potential energy surface associated with each electronic state of a molecule. For nonlinear polyatomic molecules there are 3N-6 nuclear degrees of freedom which must each be solved in order to build the complex multi-dimensional surface. Generally, a 2-dimensional cut along a specified coordinate is used to model excited state topology.

Following this we can now revisit electronic transitions in the context of the Born-Oppenheimer approximation. While a non-zero transition dipole moment is still required to couple two electronic states, as described in Equation 1.1, the nuclear coordinates must also be considered. As the nuclear motion is approximated to be stationary compared to electronic motion, electronic transitions can be thought of as an instantaneous process and is visualized as a "vertical" transition onto the excited state surface. The strength of the transition will be dictated by the overlap of the associated wavefunctions. Considering Equation 1.1, and taking into account the wavefunction separability due to the Born-Oppenheimer approximation, the transition dipole moment can then be fully described by the product of the electronic transition dipole and vibrational wavefunction as follows:

$$\mu_{i\to f,\nu_i\to\nu_f} = \int \psi_f^*(r;R)\hat{\mu}\psi_i(r;R)\,d\tau \int {\chi_{\nu_f}^f}^*(R)\chi_{\nu_i}^i(R)\,d\tau \tag{1.7}$$

where *i* and *f* indicate the initial and final state for the electronic and vibrational wavefunctions. The strength of a transition to different vibronic states is represented by the square of the overlap between the vibrational wavefunctions, this is referred to as the Franck-Condon factor:

$$FCF_{\nu_i\to\nu_f} = \left[\int {\chi_{\nu_f}^f}^*(R)\chi_{\nu_i}^i(R)\,d\tau\right]^2 \tag{1.8}$$

An illustration of vertical electronic transitions between excited state surfaces, and the corresponding vibrational wavefunctions for determining FCFs is presented in Figure 1.2.

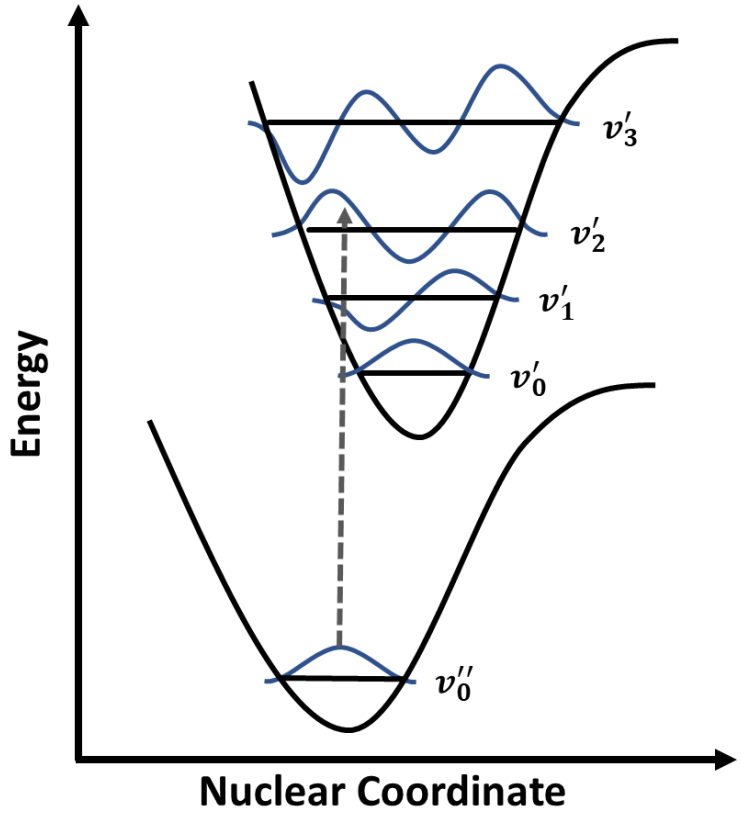

Figure 1.2. Schematic demonstrating the Franck-Condon principle for overlap between ground and excited-state vibrational wavefunctions for a vertical excitation.

1.2.3 Wave Packets

The details of electronic transitions in the context of the Born-Oppenheimer approximation described above consider single transitions at a set frequency of incident light. While utilizing ultrafast laser spectroscopy to investigate excited-state photodynamics, multiple vibrational states can be populated due to the broadband excitation pulses being used. This comes as a result of the time-bandwidth product; simply put, as time duration of a pulse is shorter (i.e. generation of well-defined ultrafast femtosecond pulses), the corresponding energy spread of the pulse is broader. It is for this reason that a superposition (i.e. wavepacket) of several vibrational modes is generated. This results in constructive and destructive interference of the associated vibrational

wavefunctions which exhibit a certain time dependence in the excited state. The following mathematical expression defines a nuclear wavepacket constructed from various vibrational wavefunctions:

$$\Psi(t) = \sum_n A_n \psi_n e^{(-iE_n t/\hbar)} \quad (1.9)$$

where n indexes the vibrational wavefunctions included in the wavepacket, E_n is the energy associated with each wavefunction, and A_n is a constant scaling factor for contributions from the electronic dipole moment and FCFs. The differences in the time dependence of contributing wavefunctions causes and evolution of the nuclear wavepacket which will traverse the potential energy surface (anharmonic well) periodically returning towards its original nuclear coordinates, providing information about the structural evolution on the potential energy surface.

1.3 Overview of Intermolecular Charge Transfer Complexes and Their Applications

Intermolecular charge transfer complexes are comprised of electron donating and accepting chromophores which exhibit charge transfer character in their ground states. This is a result of efficient mixing between the highest occupied molecular orbital (HOMO) of the donor and lowest unoccupied molecular orbital (LUMO) of the acceptor, which are relatively close in energy. A simple mathematical representation of ground and excited state wavefunctions for charge transfer complexes is shown here:

$$\Psi_G(D,A) = a\Psi_0(DA) + b\Psi_1(D^+A^-) \quad \Psi_E(D,A) = a^*\Psi_1(D^+A^-) + b^*\Psi_0(DA) \quad (1.10)$$

where $\Psi_G(D,A)$, represents ground-state wavefunctions, $\Psi_E(D,A)$ the excited-state wavefunctions, constructed as a linear combination of wavefunctions for neutral or charge transfer character ($\Psi_0(DA)$ and $\Psi_1(D^+A^-)$), a representation based on Mulliken's description of donor-acceptor complexes.[1] These are generally referred to as hybridized CT states where overlap of

frontier orbitals is the basis of CT formation. Based on this representation of state mixing (using the scalar coefficients a and b) the degree of charge transfer between donor and acceptor is represented by the following:

$$\lambda = \frac{b^2}{a^2+b^2} \tag{1.11}$$

It follows from this then that three classes of CTCs can form, 1) integer charge transfer complex (ICT) when $\lambda = 1$, 2) an optical charge transfer complex when $\lambda = 0$, or 3) partial charge transfer complex (PCT) for values of λ in between these. An energy-level schematic is shown in Figure 1.3 for comparison of ICT vs PCT. These complexes are characterized by new features that arise in ground-state absorption of the donor-acceptor pair which are not found in individual donor or acceptor spectra, and may correspond to the optical transitions of ICT or PCT states. The frequency for this transition (E_{CT}) is related to ionization energy of the donor (IE_D), electron affinity of the acceptor (EA_A), and the coulombic interaction of the complex (W) through the following expression:

$$E_{CT} = IE_D - EA_A - W \tag{1.12}$$

As a result the electron donating and accepting strengths of donor and acceptor species is important for tuning transition frequencies and also contribute to whether or not ICTs or PCTs are preferentially formed,[2] which is critical for generating free charge carriers for applications involving organic semi-conductors (OSCs).

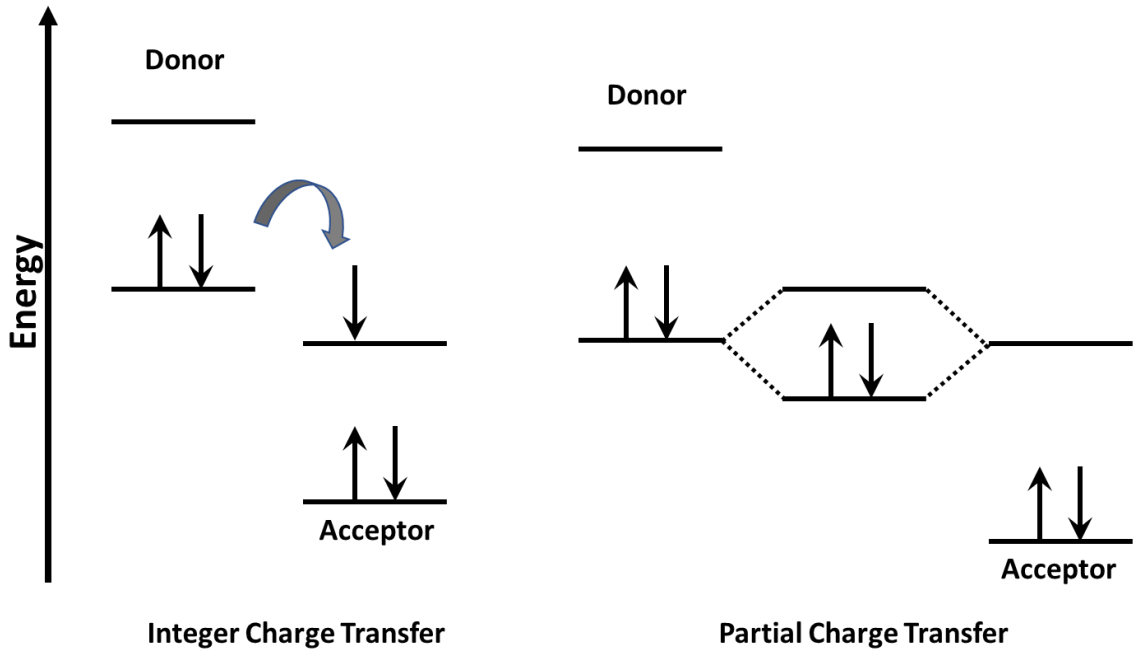

Figure 1.3. HOMO and LUMO energy level diagrams for donor-acceptor charge transfer complexes, integer charge transfer (charge separated ion pairs, left) and partial charge transfer (hybridized orbitals, right).

Electron donor and acceptor strength dependence on ICT vs PCT formation has been highlighted in studies of doped polymer film blends where conjugated polymers act as electron donors for donor-acceptor complex formation. Well-studied examples include blends of poly(3-hexylthiophene) (P3HT) and quaterthiophene (4T) with the molecular p-dopant 7,7,8,8-tetracyanoquinodimethane (TCNQ) and its fluorinated derivatives (F_XTCNQ x = 1, 2, 4); increased acceptor electron affinity is correlated with more fluorine substituents. ICT states are preferentially formed in blends with P3HT as observed by the presence of characteristic absorption features of the acceptor radical anion. In contrast, only PCT states appear for all acceptor chromophores in blends with 4T (higher ionization energy) where a broad red-shifted absorption band is observed.[3] The radical anion absorption spectrum for ICTs involving theses quinone acceptors are well known.[3-5]

For this reason, F_4TCNQ has been widely used as a p-type dopant in blends of conjugated organic polymers. Several studies have focused on how processing methods,[6] dopant ratio,[7-8] and film morphology[9-10] impact generation of ICT vs PCT states. One study showed that ICTs are the initial kinetically favored state, but over time transform into the more thermodynamically preferred PCT.[11] This was demonstrated using time dependent FTIR spectra of films collected over the course of days. Since the cyano groups on these quinone chromophores are sensitive to electron density, shifts in the CN stretching mode can be monitored to evaluate the degree of charge transfer according to the following equation:

$$\delta = \frac{2\Delta\nu}{\nu_0}\left(1 - \frac{\nu_1^2}{\nu_0^2}\right)^{-1} \tag{1.13}$$

where ν_0 and ν_1 are the frequencies for neutral F_4TCNQ and $F_4TCNQ^{\cdot-}$ as part of an ICT with values of 2227 cm^{-1} and 2194 cm^{-1}, respectively.[12-13] Even though PCT states may be thermodynamically preferred in certain film blends, the film microstructure and electronic structure has been shown to influence densities of states available for ICT vs PCT formation in studies of F_4TCNQ doped regioregular P3HT (crystalline film domains where ICT is preferred) and regiorandom P3HT (amorphous film domains where PCT is favored). As a whole, there have been numerous studies that demonstrate ICT is the dominate doping mechanism for conjugated polymers, unlike their molecular or oligomeric counterparts.[6] Other review articles are present in the literature for a more comprehensive discussion of applications and processing of CTC materials.[7, 14-17]

While extensive work has addressed principles of dopant design, doping mechanisms, and material processing for designing efficient materials for optoelectronic applications, the photoresponses of CTC based systems are less studied. One recent study used ultrafast transient absorption spectroscopy to probe polaron dynamics generated from ICT states in F_4TCNQ doped

P3HT. Through excitation-dependent measurements it was shown that films have both "free" and "trapped" polarons present across the conjugate polymer backbone.[18]

The radical anion photoresponses of TCNQ in solution and gas phase have also been explored. It is reported that fast internal conversion $D_1 \rightarrow D_0$ occurs followed by a slower vibrational cooling of a "hot" ground state.[19] These process occur on a much faster timescale (femtoseconds) in the gas phase and have been reported for other quinone based anions from time-resolved photoelectron spectroscopy.[20-22] Dianion formation in TCNQ and F_4TCNQ crystals has also been reported from anion precursors where charge separation lifetimes on the order of microseconds are reported.[4] We draw comparisons to some of the material presented in these abovementioned studies in Chapter 4 where the dynamics of F_4TCNQ-based CTCs are interrogated in condensed phases (solutions and films).[23]

A final remark is made on equilibrium formation constants for charge transfer complexes. Studies by Benesi and Hildebrand in 1949 on complex formation between iodine and aromatic hydrocarbons lead to the formulation of the Benesi-Hildebrand (BH) analysis for determining equilibrium constants (K_{CT}) and extinction coefficients (ε) for donor-acceptor complexes.[24] This method uses excess donor or acceptor concentrations in solution in order to derive an approximate linear relationship between donor concentration and CTC absorption. Linear fits in [Donor] vs *Abs* provides estimates to K_{CT} and ε and has generally been applied for interrogating weak donor-acceptor pairs which do not exhibit ICT. A more accurate approach has been proposed since these early studies which utilizes nonlinear regression to fit an exact solution for an equilibrium expression of a CT complex (Equation 1.14); like in the BH method, *Abs* can be related to K_{CT} and ε by use of Beer's Law:

$$K_{CT} = \frac{[AD]}{[A][D]} \tag{1.14}$$

This is described in detail elsewhere and the accuracy of this method has been tested for different donor-acceptor complexes across a range of concentrations.[25] The work presented in Chapter 3 utilizes this method to characterize the formation and stability of F_4TCNQ-based CTCs in various solution environments.

1.4 Overview of Intramolecular Charge Transfer Complexes and Their Application

The previous section discussed aspects of intermolecular electron transfer, in terms of ground-state charge-transfer complexes, formed either by hybridization of frontier orbitals (as PCT states) or fully charge-separated pairs (ICT states) and their importance for applications in optoelectronics. In this section we consider electron transfer processes that can occur within a single chromophore, namely photoinduced intramolecular charge transfer. A brief discussion of Marcus theory is introduced to discuss how chemical structure and solvent reorganization impact the rate of electron transfer, specifically the process of charge recombination (back electron transfer) as is relevant to studies presented in Chapter 5. Following this, an introduction to hybrid organosilane materials is provided. Donor-acceptor chromophores of these systems have been synthesized and their photophysical responses investigated for applications in molecular optoelectronics.

In the 1950's Marcus formulated his semi-classical theory for electron transfer which relates the rate of electron transfer to certain thermodynamics properties according to the following equation:

$$k_{ET} = \left(\frac{\pi}{\hbar^2 \lambda k_B T}\right)^{\frac{1}{2}} |V_{DA}|^2 \, exp\left(-\frac{(\Delta G^0 + \lambda)^2}{4\lambda k_B T}\right) \tag{1.15}$$

where λ is a reorganization energy associated with the change in charge distribution during the electron transfer, ΔG^0 is the thermodynamic free energy difference (driving force), and V_{DA} is an

electronic coupling between the reactant and product states.[26-27] With this prescription, it was realized that three "regimes" of electron transfer should exist; these are referred to as the normal regime ($\Delta G^0 < \lambda$), the barrierless regime ($\Delta G^0 = \lambda$), and the inverted regime ($\Delta G^0 > \lambda$). These regimes of the semi-classical expression are represented by a gaussian curve, where electron transfer rates will increase with changes in the driving force towards the upper limit of the barrierless regime, but should then decrease as the driving force continues to become larger (in a given chemical environment). Figure 1.4 shows representations of each region and the gaussian dependence on electron transfer rates.

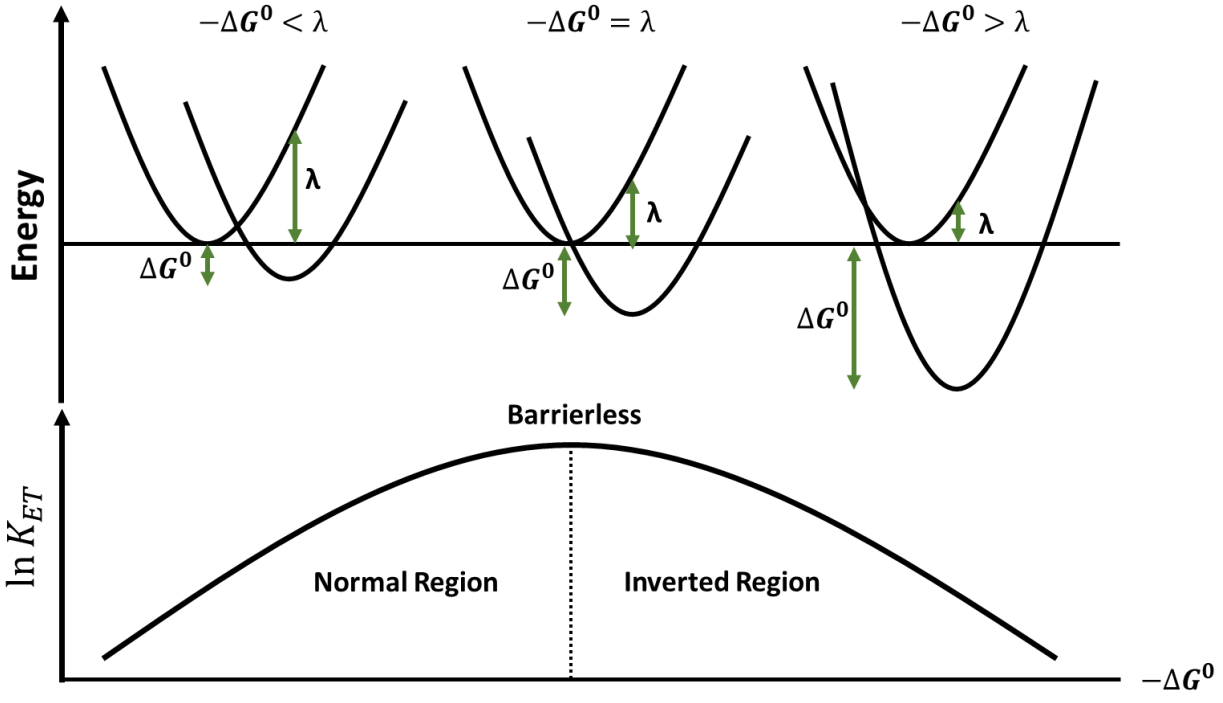

Figure 1.4. Diagram (top) representing the normal, barrierless, and inverted regimes for electron transfer. Gaussian curve for electron transfer rates and its dependence on driving force (bottom).

The reorganization energy of the system is comprised of two parts, the inner sphere (intramolecular reorganization) and outer sphere (solvent reorganization) energies. The inner-sphere reorganization energy is associated with changes in one or more intramolecular structural

coordinates between the reactant and product states. The inner sphere reorganization is defined as follows:

$$\lambda_i = \frac{1}{2} f(\Delta q_e)^2 \tag{1.16}$$

where *f* is the spring constant associated with these vibrational modes and Δq_e is the change in equilibrium bond length upon electron transfer. The outer sphere reorganization is defined as the following:

$$\lambda_o = (\Delta e)^2 \left\{\frac{1}{2a_1} + \frac{1}{2a_2} - \frac{1}{R}\right\}\left\{\frac{1}{\varepsilon_\infty} - \frac{1}{\varepsilon_0}\right\} \tag{1.17}$$

Here Δe refers to the amount of charge transfer, a_1 and a_2 are the radii of donor and acceptor species, *R* is the separation distance between each species, ε_∞ is the optical dielectric constant, and ε_0 the static dielectric constant. The first two terms of this expression provide details about the solvation energy for a given solvent dielectric as a response to charge-separation; the third term relates to the free energy associated with stabilization of the charge pairs at a separation distance *R*. Total reorganization energy can be determined from the absorption and emission spectra of emissive charge-transfer states such as those described in Chapter 5.[28]

We next consider the electronic coupling term of Equation 1.15. The mechanism of electron transfer can be separated into two types, through bond or through space. For the purpose of this thesis, we will restrict ourselves to a brief discussion of through-bond charge transfer, where two commonly accepted mechanism are described: superexchange (long range) or sequential (hopping) electron transfer. While orbital overlap is of importance in both processes, the difference between these two mechanisms is the role of the bridge. Superexchange occurs if the bridging unit can be considered as a single chromophore in which electronic coupling displays an exponential decay with distance[29]:

$$V_{DA} = V_0 e^{\left(-\frac{\beta(N-1)}{2}\right)} \quad or \quad V_{DA} = \frac{\alpha_{DB}\alpha_{BA}}{\Delta E_{DB}} \tag{1.18}$$

Here V_0 is the coupling element for the donor and acceptor pair at van der Waals separation, β is an attenuation factor, and N is the number of bonds between donor and acceptor groups. For the superexchange mechanism, the electronic coupling potential can also be written in terms of orbital coupling (α) between the donor and first bridge unit (α_{DB}), the last bridge unit and the acceptor (α_{BA}), and the energetic difference between active orbitals on the donor and bridge, ΔE_{DB}. The rate of electron transfer is therefore dependent on separation distance; however, studies have observed a lesser fall off in the rate of electron transfer than anticipated, or systems where β varied with distance or solvent polarity. In these cases it was suggested that individual bridging units could act as redox centers where electron transfer could switch to a hopping mechanism.[29] These two mechanisms are represented in Figure 1.5.

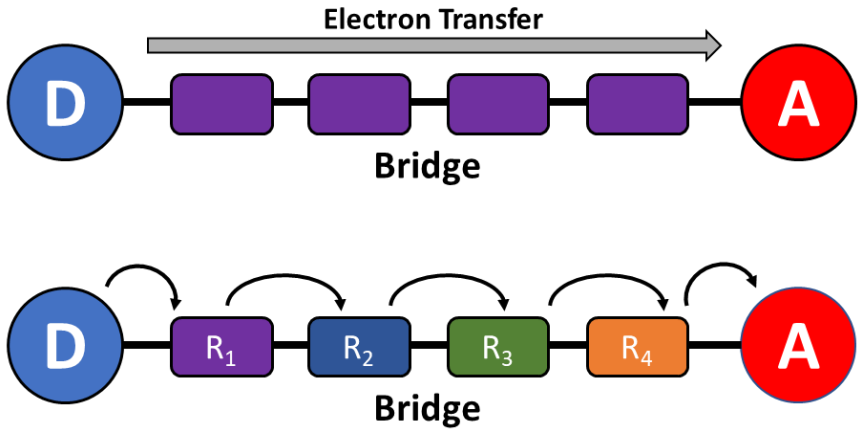

Figure 1.5. Diagrams of long-range through bond electron transfer. (top) superexchange and (bottom) hopping mechanisms.

Many studies have been conducted to test the validity of Equation 1.15, with a special interest towards validating the existence of the inverted region. In the seminal work conducted by Closs and Miller, the existence of the Marcus inverted region was verified using pulse radiolysis

to study long range intramolecular electron transfer in donor-bridge-acceptor organic structures. By varying the covalently bound donor, thereby changing the driving force for electron transfer, they verified electron transfer occurring in both the normal and inverted region.[30-31] The gaussian-like curves were also shown to shift in response to changing solvent polarity (i.e. solvent reorganization energy).

However, these and a host of studies have determined that the activation energies for electron transfer in the normal region were lower than predictions would suggest from Equation 1.15, as well as deviating from gaussian like behavior. This was suggested to be the result of excess thermal energy being transferred to intramolecular vibrational modes associated with the product state. Similarly, with the observation of increased rates in the inverted region, quantum mechanical extensions to this semiclassical model were constructed to involve charge transfer to various vibrational levels of the product state. One improved model, from a Golden Rule starting point, incorporated the role of high frequency solvent or intramolecular vibrational modes through Franck-Condon weighted density of states and is defined as follows[32]:

$$k_{ET} = \frac{2\pi|V|^2}{\hbar\sqrt{4\lambda k_B T}} \sum_{n=0}^{\infty} e^{-S^2} \frac{S^n}{n!} \exp\left[-\frac{(\Delta G_0 + \lambda + n\hbar\omega)^2}{4\lambda k_B T}\right] \quad (1.19)$$

Here, we have the same driving force, electronic coupling, and reorganization energy terms, as well as the frequency ($\hbar\omega$) and displacement (captured by the Huang-Rhys Factor $S = \lambda_i/\hbar\omega$) along the Franck-Condon active vibrational mode(s) for charge transfer. This model is better suited to describe the deviations from the gaussian nature of Equation 1.15 as it relates to the inverted region, where it has been shown to generate an exponential gap law behavior. Figure 1.6 presents potential energy wells related to various states for photoinduced charge transfer.

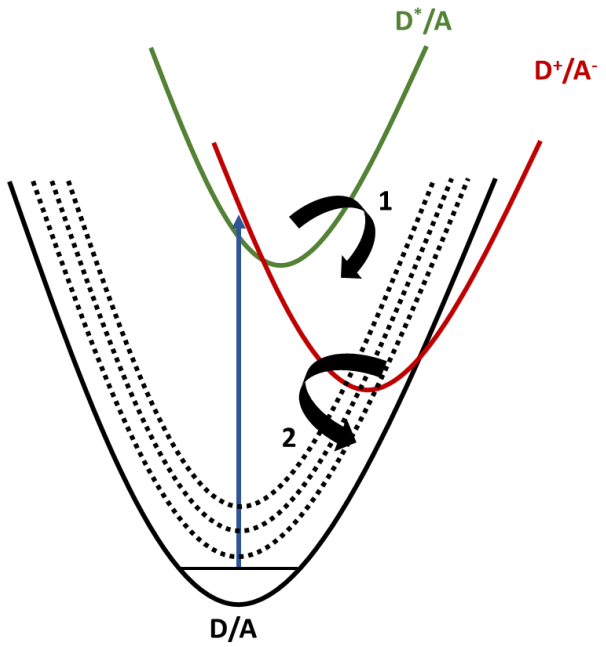

Figure 1.6. Schematic of photoinduced charge transfer. Photoexcitation of the ground-state donor (D/A) prepares a local excited-state (D^*/A) for electron transfer to a charge separated state (D^+/A^-). Higher energy vibrational modes that may be important for charge recombination back to the ground-state are shown as the dotted red potential wells.

Following these developments for theories of electron transfer, several studies have utilized ultrafast spectroscopies to interrogate photoinduced charge transfer phenomena in a host of organic or inorganic systems. These investigations generally focus on structure-function relationships for varying parameters found in Equation 1.19 in order to tune electron transfer rates. Some general approaches involve varying the chemical structure of donor, acceptor, or bridging units by incorporation of electron donating or accepting functional groups.[33-35] Another approach could be to vary the electronic coupling between donor and acceptor units. This may be achieved by variation of chain length or bridging chemical structure, as well as by using chemical tethers to influence orbital overlaps between individual units (refer to Equation 1.18).[29] An alternative method is to change the chemical environment (for a fixed driving force) to alter rates of electron

transfer.[36-37] Some of these ideas are considered for studies presented in Chapter 5 involving photoinduced intramolecular charge transfer of organosilane systems.

1.5 Overview of Organosilanes

Organo-, oligo-, and poly-silanes are hybrid molecules consisting of a few or many silicon atoms (in chains or cycles) bound to organic substituents. In the 1960's Gilman et. al. demonstrated that permethylated organosilanes of various chain lengths exhibit unique spectral properties which arise when Si-Si bonds are present with organic π-conjugated substituents. It was shown by varying the conjugation of the organic capping units in disilanes (e.g. trimethyl to triphenyl substituents) that the peak absorption red shifts by up to 50 nm (~200 to 247 nm respectively), a more dramatic shift than is observed in carbon analogues. Also, the molar absorptivity showed a five-fold increase (~7,000 to 33,000 L mol-1 cm-1).[38] Based on these findings it was proposed that the sigma conjugated silicon chains could couple with the π-conjugated organic substituents through silicon's vacant d-orbitals that are suitably overlapped with π-orbitals.[38] This extended σ-π conjugation would lead to the red shifting observed with the addition of π-conjugated vs. non-conjugated substituents. Later West et. al. demonstrated intermolecular charge-transfer behavior between linear and cyclic permethylated oligosilanes and the electron acceptor tetracyanoethylene (TCNE).[39] This work was the first to demonstrate that charge transfer can occur from σ-conjugated electron donors to π-conjugated electron acceptors, and arises from the lower ionization potential of the Si chain compared to that of the sigma-bonding network of carbon.

Due to these unique characteristics, the synthesis and characterization of aryl or vinyl functionalized oligosilanes has been of interest to the scientific community. It is important to note

that there is greater structural flexibility of the tetrahedron silicon backbone compared to π-conjugated systems, and hence variations in molecular conformation can impact the energetics and photophysics of organosilanes.[40] Due to their long-range sigma-bonding orbital interactions and flexibility, six stable conformers relative to any neighboring pair of Si atoms have been proposed in studies on linear chain organosilanes.[41] One can treat the orbital interactions using a modification to Hückel theory wherein not only are $\beta_{vicinal}$ and $\beta_{geminal}$ orbital interactions important, but $\beta_{1,3}$ and $\beta_{1,4}$ interactions must be considered.[40, 42-43] Figure 1.7 presents a diagram for molecular conformation and orbital interaction responsible for hybrid σ-π conjugation.

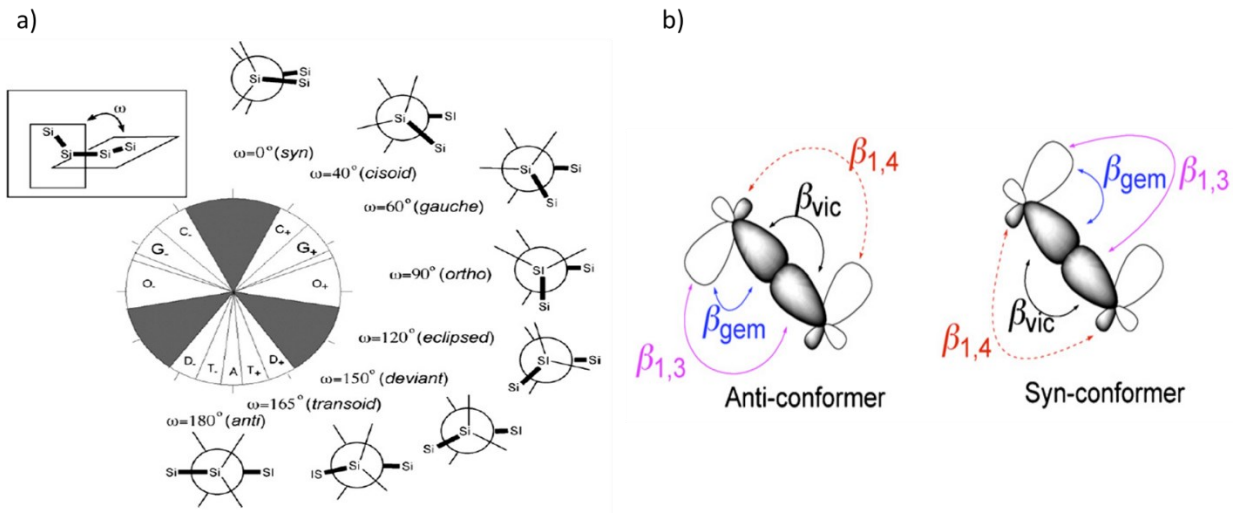

Figure 1.7. (a) Conformers designated for oligosilanes (greyed-out regions represent nonstable geometries). (b) Orbital interactions about the dihedral angle in an oligosilane backbone which are important to consider for analyzing conformers and electronic transitions.[42]

More recently, the photophysics of organosilanes have been explored through the lens of structure-response relationships. There has been recent interest in pi-disilane-pi architectures, as these can display large hyperpolarizabilities for nonlinear optical applications.[44-46] Furthermore strong emission has been shown to occur in disilane-bridged organosilanes following aggregation, a processes known as aggregated induced emission.[47-49] These structures have also been used as

bridging units in studies of porphyrin-fullerene dyads, common systems for modeling artificial photosynthesis.[50]

In collaboration with the Klausen group, our lab has investigated a new class of cyano(ester)vinyl capped oligosilanes (shown in Figure 1.8), in which the silane chain acts as the electron donor. The charge transport and photoinduced charge transfer behaviors have been characterized. Thin films of these hybrid molecules were shown to exhibit higher conductivities than films made with their σ- or π- conjugated components.[51] Furthermore, new absorption features were present in compounds where the silane chain is covalently bound to the organic acceptor. Steady-state emission spectra demonstrated large solvatochromic shifts as solvent polarity was increased. Large changes in dipole moment between the ground and excited states were confirmed through Lippert analysis of absorption and emission data. The steady-state absorption and emission supported that this new absorption feature should be related to a σ-π^* optical charge transfer transition.[52]

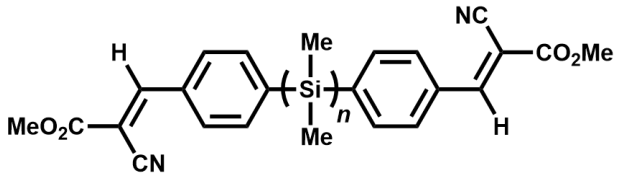

Si2s-E,C (n=2, ester-cyano-vinyl)

Figure 1.8. Acceptor-Donor-Acceptor oligosilane. The variable silane chain (n indicates number of Si atoms in the chain) acts as the electron rich acceptor for photoinduced charge transfer to the electron poor ester-cyano-vinyl acceptor unit.

Intramolecular charge transfer, from electron rich silane to electron deficient cyano groups, was confirmed by comparing Raman active features in femtosecond stimulated Raman spectra (excited-state Raman spectroscopy) to the calculated Raman spectrum of a reduced asymmetric oligosilane.[53] The degree of charge separation was also shown to scale with silane chain length.

Photoinduced charge separation was characterized in acceptor-donor-acceptor and donor-acceptor molecules. Asymmetric charge separation was observed to occur in both cases due to structural symmetry breaking related to the flexible silane core. The lifetimes of charge separation (or charge recombination) where shown to have a structure dependent gap-law behavior and charge recombination was demonstrated to occur in the Marcus inverted region (confirmed via solvent dependent measurements).[52] The conclusions from this prior work led to the investigation of donor- and acceptor-dependent studies discussed in Chapter 5, which investigates how charge separation lifetimes can be tuned via control of parameters described in Equation 1.20.[54]

1.6 Overview of Thesis Contents

Chapter 2 provides an overview on experimental techniques employed in the studies described in Chapter 3-5. These include steady-state absorption and emission spectroscopies used to characterize charge transfer formation in donor-acceptor complexes and emissive characteristics of organosilane compounds. Time-resolved and temperature dependent UV-Vis measurements are briefly discussed for investigating stability of charge transfer complexes. Finally ultrafast spectroscopic methods and instrument layout are discussed; these were used in work described in Chapters 4 and 5 to interrogated photoresponses of CTCs and charge recombination dynamics in organosilanes.

Chapter 3 addresses questions of charge transfer formation and complex stability in F_4TCNQ-based CTCs. These studies utilize nonlinear fitting routines to analyze the changes in CTC absorption as a function of donor concentration. These pieces of data allow equilibrium constants of formation to be determined. We find large formation constants for the donor-acceptor pair, which was not surprising based on the relative electron donating and accepting strength of

each species. Temperature dependent determinations of formation constants provide insight on enthalpic and entropic contributions to formation, where complexes in high polarity solvents display strong enthalpic stabilization, whereas complexes in weakly polar environments are entropically favored.

Chapter 4 presents a study of the ultrafast photoresponses of these complexes via transient absorption spectroscopy. Questions concerning chemical environment (solution vs film) and excitation dependence are addressed. We find the acceptor anion dominates transient dynamics where excited state deactivation is shown to occur via rapid internal conversion followed by vibrational cooling of a "hot" ground state. CTC doped films were characterized by the presence of both ICTs and PCT, where transient spectra displayed similar features to solution measurements. Deactivation was assigned to the same pathways and occurred at a faster rate than in solution.

Chapter 5 provides an extension to the work summarized above for photoinduced intramolecular charge transfer in vinyl end-capped oligosilanes. Here transient absorption spectroscopy is used to characterize the recombination rates of silanes capped with diester and dicyano vinyl organic acceptors. We observe transient spectra to be highly similar to what we observed previously for mixed cyano(ester)vinyl acceptors and conclude that photoinduced charge separation also occurs in these new compounds. We also determine the strength of the organic acceptor dictates whether or not electronic coupling will dominate recombination dynamics. Finally, solvent dependent measurements were conducted to show electronic coupling and reorganization energy can be decoupled to extend charge separation lifetimes in non-polar solvent environments.

1.7 References

1. Mulliken, R. S., Molecular Compounds and Their Spectra 2. *Journal of the American Chemical Society* **1952**, *74*, 811-824.

2. Méndez, H., et al., Doping of Organic Semiconductors: Impact of Dopant Strength and Electronic Coupling. *Angewandte Chemie International Edition* **2013**, *52*, 7751-7755.

3. Mendez, H., et al., Charge-Transfer Crystallites as Molecular Electrical Dopants. *Nature Communications* **2015**, *6*.

4. Ma, L.; Hu, P.; Jiang, H.; Kloc, C.; Sun, H.; Soci, C.; Voityuk, A. A.; Michel-Beyerle, M. E.; Gurzadyan, G. G., Single Photon Triggered Dianion Formation in TCNQ and F_4TCNQ Crystals. *Scientific Reports* **2016**, *6*, 28510.

5. Zanon, I.; Pecile, C., Vibronic Structure of the near-Infrared and Visible Electronic Transitions of 7,7,8,8-Tetracyanoquinodimethane Radical Anion. *The Journal of Physical Chemistry* **1983**, *87*, 3657-3664.

6. Stanfield, D. A.; Wu, Y.; Tolbert, S. H.; Schwartz, B. J., Controlling the Formation of Charge Transfer Complexes in Chemically Doped Semiconducting Polymers. *Chemistry of Materials* **2021**, *33*, 2343-2356.

7. Salzmann, I.; Heimel, G.; Oehzelt, M.; Winkler, S.; Koch, N., Molecular Electrical Doping of Organic Semiconductors: Fundamental Mechanisms and Emerging Dopant Design Rules. *Accounts of Chemical Research* **2016**, *49*, 370-378.

8. Theurer, C. P.; Richter, M.; Rana, D.; Duva, G.; Lepple, D.; Hinderhofer, A.; Schreiber, F.; Tegeder, P.; Broch, K., Coexistence of Ion Pairs and Charge-Transfer Complexes and Their Impact on Pentacene Singlet Fission. *The Journal of Physical Chemistry C* **2021**, *125*, 23952-23959.

9. Neelamraju, B.; Watts, K. E.; Pemberton, J. E.; Ratcliff, E. L., Correlation of Coexistent Charge Transfer States in F_4TCNQ-Doped P3HT with Microstructure. *The Journal of Physical Chemistry Letters* **2018**, *9*, 6871-6877.

10. Jacobs, I. E.; Cendra, C.; Harrelson, T. F.; Valdez, Z. I. B.; Faller, R.; Salleo, A.; Moule, A. J., Polymorphism Controls the Degree of Charge Transfer in a Molecularly Doped Semiconducting Polymer. *Materials Horizons* **2018**, *5*, 655-660.

11. Watts, K. E.; Neelamraju, B.; Ratcliff, E. L.; Pemberton, J. E., Stability of Charge Transfer States in F_4TCNQ-Doped P3HT. *Chemistry of Materials* **2019**, *31*, 6986-6994.

12. Kampar, E.; Neilands, O., Degree of Charge Transfer in Donor–Acceptor Systems of the Π–Π Type. *Russian Chemical Reviews* **1986**, *55*, 334-342.

13. Meneghetti, M.; Pecile, C., Charge-Transfer Organic-Crystals - Molecular Vibrations and Spectroscopic Effects of Electron-Molecular Vibration Coupling of the Strong Electron-Acceptor $TCNQF_4$. *Journal of Chemical Physics* **1986**, *84*, 4149-4162.

14. Goetz, K. P.; Vermeulen, D.; Payne, M. E.; Kloc, C.; McNeil, L. E.; Jurchescu, O. D., Charge-Transfer Complexes: New Perspectives on an Old Class of Compounds. *Journal of Materials Chemistry C* **2014**, *2*, 3065-3076.

15. Wang, W.; Luo, L. X.; Sheng, P.; Zhang, J.; Zhang, Q. C., Multifunctional Features of Organic Charge-Transfer Complexes: Advances and Perspectives. *Chemistry-a European Journal* **2021**, *27*, 464-490.

16. Zhang, J.; Xu, W.; Sheng, P.; Zhao, G.; Zhu, D., Organic Donor–Acceptor Complexes as Novel Organic Semiconductors. *Accounts of Chemical Research* **2017**, *50*, 1654-1662.

17. Jiang, H.; Hu, P.; Ye, J.; Zhang, K. K. K.; Long, Y.; Hu, W. P.; Kloc, C., Tuning of the Degree of Charge Transfer and the Electronic Properties in Organic Binary Compounds by Crystal Engineering: A Perspective. *Journal of Materials Chemistry C* **2018**, *6*, 1884-1902.

18. Voss, M. G.; Scholes, D. T.; Challa, J. R.; Schwartz, B. J., Ultrafast Transient Absorption Spectroscopy of Doped P3HT Films: Distinguishing Free and Trapped Polarons. *Faraday Discussions* **2019**, *216*, 339-362.

19. Ma, L.; Hu, P.; Kloc, C.; Sun, H. D.; Michel-Beyerle, M. E.; Gurzadyan, G. G., Ultrafast Spectroscopic Characterization of 7,7,8,8-Tetracyanoquinodimethane (TCNQ) and Its Radical Anion ($TCNQ^{\cdot -}$). *Chemical Physics Letters* **2014**, *609*, 11-14.

20. Roberts, G. M.; Lecointre, J.; Horke, D. A.; Verlet, J. R. R., Spectroscopy and Dynamics of the 7,7,8,8-Tetracyanoquinodimethane Radical Anion. *Physical Chemistry Chemical Physics* **2010**, *12*, 6226-6232.

21. Horke, D. A.; Roberts, G. M.; Verlet, J. R. R., Excited States in Electron-Transfer Reaction Products: Ultrafast Relaxation Dynamics of an Isolated Acceptor Radical Anion. *Journal of Physical Chemistry A* **2011**, *115*, 8369-8374.

22. Horke, D. A.; Li, Q. S.; Blancafort, L.; Verlet, J. R. R., Ultrafast above-Threshold Dynamics of the Radical Anion of a Prototypical Quinone Electron-Acceptor. *Nature Chemistry* **2013**, *5*, 711-717.

23. Barrett, B. J.; Saund, S. S.; Dziatko, R. A.; Clark-Winters, T. L.; Katz, H. E.; Bragg, A. E., Spectroscopic Studies of Charge-Transfer Character and Photoresponses of F_4TCNQ-Based Donor–Acceptor Complexes. *The Journal of Physical Chemistry C* **2020**, *124*, 9191-9202.

24. Benesi, H. A.; Hildebrand, J. H., A Spectrophotometric Investigation of the Interaction of Iodine with Aromatic Hydrocarbons. *Journal of the American Chemical Society* **1949**, *71*, 2703-2707.

25. Grebenyuk, S. A.; Perepichka, I. F.; Popov, A. F., Evaluation of the Parameters of 1 : 1 Charge Transfer Complexes from Spectrophotometric Data by Non-Linear Numerical Method. *Spectrochimica Acta Part a-Molecular and Biomolecular Spectroscopy* **2002**, *58*, 2913-2923.

26. Marcus, R. A., On the Theory of Oxidation-Reduction Reactions Involving Electron Transfer .1. *Journal of Chemical Physics* **1956**, *24*, 966-978.

27. Marcus, R. A., Electron-Transfer Reactions in Chemistry - Theory and Experiment (Nobel Lecture). *Angewandte Chemie-International Edition in English* **1993**, *32*, 1111-1121.

28. Solís, C.; Grosso, V.; Faggioli, N.; Cosa, G.; Romero, M.; Previtali, C.; Montejano, H.; Chesta, C., Estimation of the Solvent Reorganization Energy and the Absolute Energy of Solvation of Charge-Transfer States from Their Emission Spectra. *Photochemical & Photobiological Sciences* **2010**, *9*, 675-686.

29. Benniston, A. C.; Harriman, A., Charge on the Move: How Electron-Transfer Dynamics Depend on Molecular Conformation. *Chemical Society Reviews* **2006**, *35*, 169-179.

30. Miller, J. R.; Calcaterra, L. T.; Closs, G. L., Intramolecular Long-Distance Electron Transfer in Radical Anions. The Effects of Free Energy and Solvent on the Reaction Rates. *Journal of the American Chemical Society* **1984**, *106*, 3047-3049.

31. Closs, G. L.; Miller, J. R., Intramolecular Long-Distance Electron-Transfer in Organic-Molecules. *Science* **1988**, *240*, 440-447.

32. Barbara, P. F.; Meyer, T. J.; Ratner, M. A., Contemporary Issues in Electron Transfer Research. *Journal of Physical Chemistry* **1996**, *100*, 13148-13168.

33. Akbarimoosavi, M.; Rohwer, E.; Rondi, A.; Hankache, J.; Geng, Y.; Decurtins, S.; Hauser, A.; Liu, S. X.; Feurer, T.; Cannizzo, A., Tunable Lifetimes of Intramolecular Charge-Separated States in Molecular Donor-Acceptor Dyads. *Journal of Physical Chemistry C* **2019**, *123*, 8500-8511.

34. Cody, J.; Mandal, S.; Yang, L. C.; Fahrni, C. J., Differential Tuning of the Electron Transfer Parameters in 1,3,5-Triarylpyrazolines: A Rational Design Approach for Optimizing the Contrast Ratio of Fluorescent Probes. *Journal of the American Chemical Society* **2008**, *130*, 13023-13032.

35. Gust, D.; Moore, T. A.; Moore, A. L., Molecular Mimicry of Photosynthetic Energy and Electron-Transfer. *Accounts of Chemical Research* **1993**, *26*, 198-205.

36. Hyun, B. R.; Bartnik, A. C.; Lee, J. K.; Imoto, H.; Sun, L. F.; Choi, J. J.; Chujo, Y.; Hanrath, T.; Ober, C. K.; Wise, F. W., Role of Solvent Dielectric Properties on Charge Transfer from Pbs Nanocrystals Molecules. *Nano Letters* **2010**, *10*, 318-323.

37. Ratera, I.; Sporer, C.; Ruiz-Molina, D.; Ventosa, N.; Baggerman, J.; Brouwer, A. M.; Rovira, C.; Veciana, J., Solvent Tuning from Normal to Inverted Marcus Region of Intramolecular

Electron Transfer in Ferrocene-Based Organic Radicals. *Journal of the American Chemical Society* **2007**, *129*, 6117-6129.

38. Gilman, H.; Atwell, W. H.; Schwebke, G. L., Ultraviolet Properties of Compounds Containing the Silicon-Silicon Bond. *Journal of Organometallic Chemistry* **1964**, *2*, 369-371.

39. Traven, V. F.; West, R., Charge-Transfer Complexing between Permethylpolysilanes and Tetracyanoethylene. *Journal of the American Chemical Society* **1973**, *95*, 6824-6826.

40. Plitt, H. S.; Michl, J., Conformational Effects on Sigma-Conjugation. Uv and IR Spectra of Matrix-Isolated Trans- and Gauche-*n*-Si_4Me_{10}. *Chemical Physics Letters* **1992**, *198*, 400-405.

41. Michl, J.; West, R., Conformations of Linear Chains. Systematics and Suggestions for Nomenclature. *Accounts of Chemical Research* **2000**, *33*, 821-823.

42. Karatsu, T., Photochemistry and Photophysics of Organomonosilane and Oligosilanes: Updating Their Studies on Conformation and Intramolecular Interactions. *Journal of Photochemistry and Photobiology C-Photochemistry Reviews* **2008**, *9*, 111-137.

43. Fogarty, H. A.; Casher, D. L.; Imhof, R.; Schepers, T.; Rooklin, D. W.; Michl, J., Sigma Bonds: Electronic Structure, Photophysics, and Photochemistry of Oligosilanes. *Pure and Applied Chemistry* **2003**, *75*, 999-1020.

44. vanHutten, P. F.; Hadziioannou, G.; Burst, R.; Feil, D., Calculation of the Hyperpolarizabilities of Silicon-Based Donor-Acceptor Compounds for Nonlinear Optics. *Journal of Physical Chemistry* **1996**, *100*, 85-94.

45. Mignani, G.; Kramer, A.; Puccetti, G.; Ledoux, I.; Soula, G.; Zyss, J.; Meyrueix, R., A New Class of Silicon-Compounds with Interesting Nonlinear Optical Effects. *Organometallics* **1990**, *9*, 2640-2643.

46. Mignani, G.; Barzoukas, M.; Zyss, J.; Soula, G.; Balegroune, F.; Grandjean, D.; Josse, D., Improved Transparency Efficiency Trade-Off in a New Class of Nonlinear Organosilicon Compounds. *Organometallics* **1991**, *10*, 3660-3668.

47. Shimada, M.; Tsuchiya, M.; Sakamoto, R.; Yamanoi, Y.; Nishibori, E.; Sugimoto, K.; Nishihara, H., Bright Solid-State Emission of Disilane-Bridged Donor-Acceptor-Donor and Acceptor-Donor-Acceptor Chromophores. *Angewandte Chemie-International Edition* **2016**, *55*, 3022-3026.

48. Usuki, T.; Shimada, M.; Yamanoi, Y.; Ohto, T.; Tada, H.; Kasai, H.; Nishibori, E.; Nishihara, H., Aggregation-Induced Emission Enhancement from Disilane-Bridged Donor-Acceptor-Donor Luminogens Based on the Triarylamine Functionality. *Acs Applied Materials & Interfaces* **2018**, *10*, 12164-12172.

49. Shimada, M.; Yamanoi, Y.; Matsushita, T.; Kondo, T.; Nishibori, E.; Hatakeyama, A.; Sugimoto, K.; Nishihara, H., Optical Properties of Disilane-Bridged Donor Acceptor

Architectures: Strong Effect of Substituents on Fluorescence and Nonlinear Optical Properties. *Journal of the American Chemical Society* **2015**, *137*, 1024-1027.

50. Sasaki, M.; Shibano, Y.; Tsuji, H.; Araki, Y.; Tamao, K.; Ito, O., Oligosilane Chain-Length Dependence of Electron Transfer of Zinc Porphyrin-Oligosilane-Fullerene Molecules. *Journal of Physical Chemistry A* **2007**, *111*, 2973-2979.

51. Surampudi, S.; Yeh, M. L.; Siegler, M. A.; Hardigree, J. F. M.; Kasl, T. A.; Katz, H. E.; Klausen, R. S., Increased Carrier Mobility in End-Functionalized Oligosilanes. *Chemical Science* **2015**, *6*, 1905-1909.

52. Zhou, J. W.; Folster, C. P.; Surampudi, S. K.; Jimenez, D.; Klausen, R. S.; Bragg, A. E., Asymmetric Charge Separation and Recombination in Symmetrically Functionalized Sigma-Pi Hybrid Oligosilanes. *Dalton Transactions* **2017**, *46*, 8716-8726.

53. Zhou, J. W.; Surampudi, S. K.; Bragg, A. E.; Klausen, R. S., Photoinduced Charge Separation in Molecular Silicon. *Chemistry-a European Journal* **2016**, *22*, 6204-6207.

54. Barrett, B. J.; Jimenez, D.; Klausen, R. S.; Bragg, A. E., Intramolecular Photoinduced Charge Transfer and Recombination Dynamics in Vinylarene Terminated Organosilanes. *The Journal of Physical Chemistry B* **2021**, *125*, 8460-8471.

Chapter 2

Methods

2.1 Introduction

Optical spectroscopies, including steady-state and transient techniques, are critical tools for characterizing photophysical and photochemical responses of molecules and materials. While more sophisticated than steady-state methods, transient spectroscopies allow one to monitor photophysical dynamics that occur in the fleeting moments after excitation of matter with light. However, photophysical relaxation processes can occur on different timescales and at different energies, and it is therefore important to choose a technique that matches the time and energy range at which the transient phenomena occurs. For example, in studies described in Chapter 5, ultrafast transient absorption spectroscopy was utilized involving the use of femtosecond pulses to monitor intramolecular charge transfer dynamics that evolve over the course of femto- to picoseconds upon UV irradiation. For even slower transient signals occurring on a seconds to minutes timescale, such as the evolution of spectral properties during material processing, time-resolved UV-Vis spectroscopy can be employed.

2.2 Steady-State Spectroscopies

One of the simplest techniques used to characterize optical properties of materials is to measure their ground-state electronic absorption spectra via UV-Vis spectroscopy. This is also a prerequisite for conducting transient spectroscopic techniques that probe excited-state dynamics since excitation pulses are required to promote a system onto an excited state surface via an optical transition determined from a ground-state UV-Vis spectra. For work presented here, UV-Vis spectra were collected using deuterium and tungsten lamps that are fiber optically coupled to one

of two spectrometers, a Stellarnet Black C-25 UV/Vis spectrometer (200-850 nm) or Blue Wave Vis-25 spectrometer (350-1100 nm). Dark background spectra and solvent reference spectra were collected prior to sample measurements under the same experimental conditions (i.e. pathlength, temperature, etc.). Sample absorbance (or optical density (OD)) was determined from the attenuation of light transmitted through the sample compared to the reference and provides information about sample absorptivity and concentration following the Beer-Lambert law:

$$A = \varepsilon c l \tag{2.1}$$

where A is the sample's absorbance at a given wavelength, ε is the molar extinction coefficient, c is the sample concentration, and l is the sample optical pathlength. A generic absorption spectrum for an organic molecule is shown in Figure 2.1 for a $S_0 \rightarrow S_1$ transition that exhibits vibronic features (excitation to different vibrational energy levels in the S_1 electronic state) with intensities arising from variation in Franck-Condon factors between ground and excited state vibrational wavefunctions.

In contrast, steady-state fluorescence spectroscopy (dispersed fluorescence) measures photon emission from a sample and is a reference free measurement. Here a wavelength is selected for excitation within the sample absorption spectrum, with emitted photons collected at 90° relative to the excitation source; emission is then measured with a spectrometer over a set wavelength range. Fluorescence spectra were collected with a Horiba Fluorolog (FL-1000, Xenon Arc lamp). Kasha's rule applies for fluorescence of most organic molecules, where fast internal conversion and/or vibrational relaxation will occur before fluorescence from the lowest vibrational level on the S_1 surface. For rigid aromatic molecules (not undergoing significant structural relaxation), a fluorescence spectrum tends to be a mirror image of the absorption spectrum, but is Stokes' shifted to longer wavelengths due to energy loss from vibrational relaxation (as shown in Figure 2.1). In

contrast, fluorescence excitation spectroscopy is complementary to absorption spectroscopy; here the excitation wavelength is scanned, and photon emission is collected at a set wavelength. This technique can aid in distinguishing what the emitting state is when there are overlapping transitions in a congested absorption spectrum. This method is used in our studies on the photoinduced charge separation in organosilanes described in the Introduction and Chapter 5.

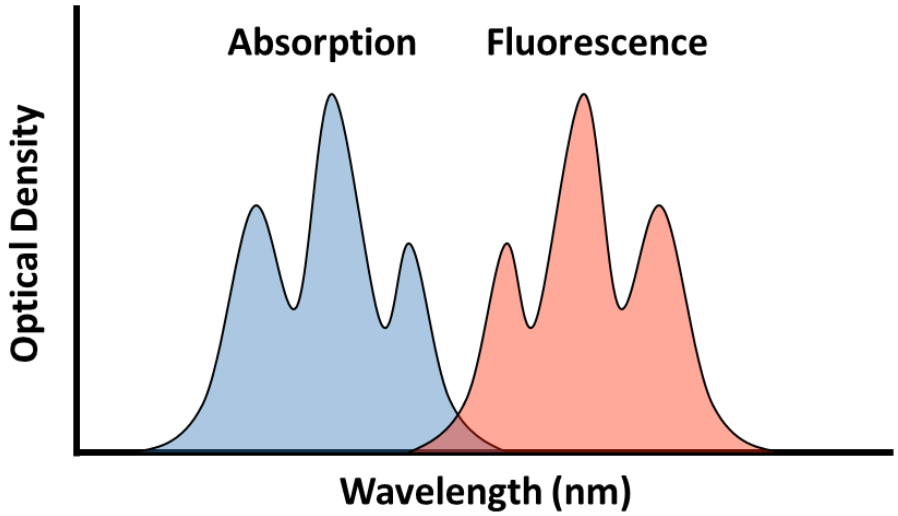

Figure 2.1. Steady-state absorption (blue) and emission (red) spectra of a typical organic molecule with intensities of vibronic transitions dictated by Franck-Condon factors.

Fourier transform infrared spectroscopy (FTIR) is a steady-state characterization technique that provides structural information in terms of IR-active modes of molecular vibration. The operation of FTIR instruments involve a Michaelson interferometer that collects sample absorption at different tunable mirror distances to generate an interferogram, which is then Fourier transformed to provide an absorption spectrum with respect to vibrational frequency. FTIR spectra presented in this dissertation were measured using a Mattson Infinity Series FTIR with an EG&G Judson MCT detector. Measurements were collected in transmission mode and under a purge to eliminate IR signatures of water and CO_2.

2.3 Time-Resolved UV-Vis

The spectroscopic techniques discussed above interrogate the absorption or emission properties of molecules or materials in steady-state (with no explicit time dependence for a single spectrum). However, in some scenarios it may be of interest to utilize time-dependent capture of the ground-state absorption or emission spectrum. For example, if a system is initially formed in a kinetically preferred state and transitions very slowly to a different thermodynamically stable state, one can capture these changes by collecting time-dependent absorption or emission spectra over the course of seconds to minutes, or even up to hours or days. As is discussed in Chapter 5, we used this approach for characterizing the evolution in properties of CT complexes throughout the course of drying a dropcast polymer film. We used the same UV-Vis instrumentation described above, taking advantage of an episodic data capture mode for time-resolved UV-Vis collection: A continuous capture mode was selected with a designated capture time between each episode to collect a series of UV-Vis spectra at distinct time delays. A schematic for the film drying measurement is shown in Figure 2.2. Fiber optics were secured in a designed u-shaped film sample holder, which was secured to a ring stand mount perpendicular to the benchtop and supported by an adjustable base plate. Films were then dropcast as the episodic data capture was initiated.

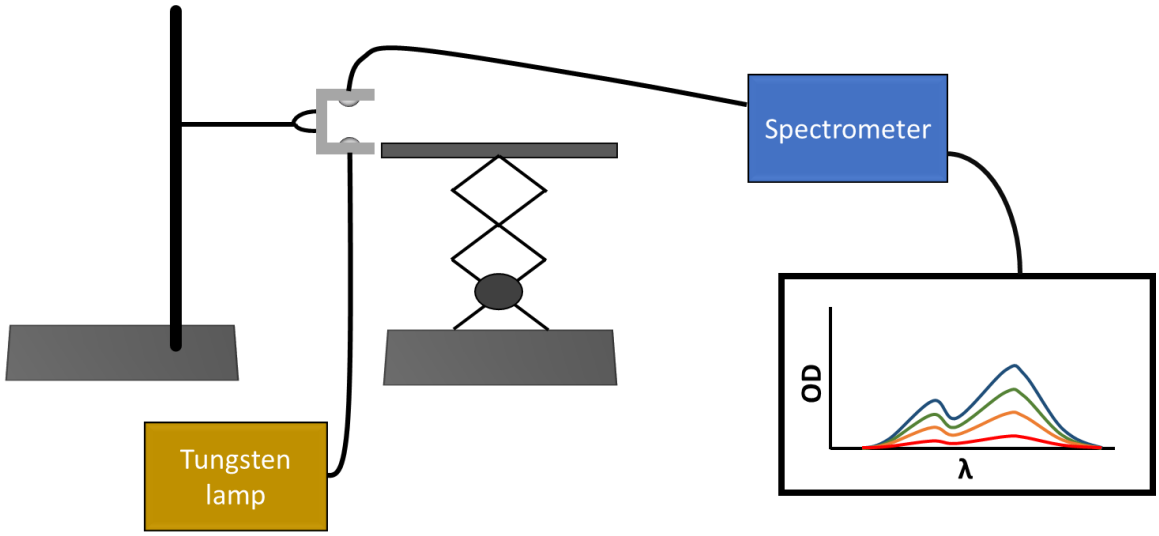

Figure 2.2. Experimental layout of time-resolved UV-Vis absorption for film drying experiments.

2.4 Temperature Dependent UV-Vis

While photophysical and photochemical characterization of materials is generally conducted at room temperature, further physical information may be gained by conducting temperature dependent studies. For example, as discussed in Chapter 3, observing a temperature-dependent change in the equilibrium constant of complex formation provides thermodynamic insight (enthalpies and entropies of formation) to complex stability. In these measurements, precise temperature control must be maintained for quantitative accuracy, and can be achieve by use of a cryostat. Temperature dependent measurements were collected using a Unisoku UnispeKs CoolSpeK UV USP-203 series cryostat (temperature range -80°C to +100°C in 0.1°C steps). The fiber optics coupled to our Stellarnet light sources and spectrograph were incorporated into the setup for UV-Vis spectroscopy. A schematic of the experimental setup is shown in Figure 2.3. Briefly, the dispersed output of light from the fiber optic is centered on the sample chamber windows (this output diverges into three separated spots, the spot that was visually the brightest was adjusted to the center of the window). The light transmitted through the sample chamber was

then collected by a mounted fiber optic coupled to our spectrograph. Background samples were collected as usual at the set temperature of the experiment and allowed to equilibrate 4 to 5 minutes depending on the difference in value from room temperature. Samples were then introduced and allowed to equilibrate for the same time and UV-Vis spectra were then collected.

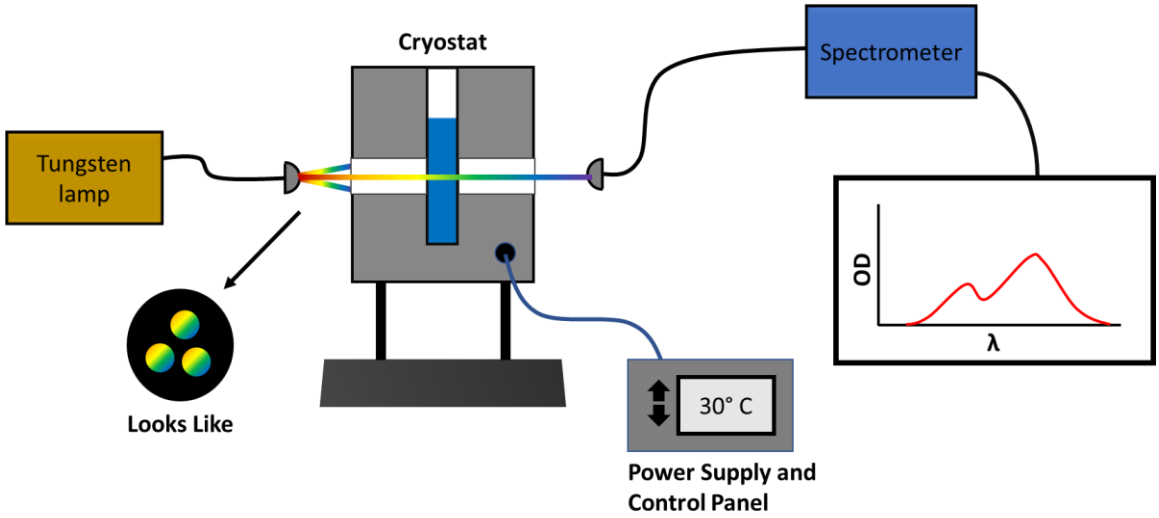

Figure 2.3. Experimental layout for temperature dependent UV-Vis absorption measurements.

2.5 Transient Absorption Spectroscopy (TAS)

The Bragg Lab is currently capable of conducting a variety of time-resolved excited state spectroscopic experiments using techniques including femtosecond stimulated Raman spectroscopy, Pump-Repump-Probe spectroscopy, microsecond transient absorption spectroscopy, and broadband measurements of transient polarization anisotropy. The research discussed in the following chapters focuses on the use of transient absorption spectroscopy (TAS or pump-probe spectroscopy) to probe photodynamics of organosilane materials and CTCs.

TAS can be thought of as UV-Vis spectroscopy of excited states, however, instead of collecting a time integrated spectrum, time-resolved absorption spectra are gathered at specified time delays after photoexcitation and provide a probe of excited-state dynamics. These

experiments require two light pulses: an excitation or "pump" pulse to promote a sample onto an excited-state surface, and a probe pulse to then monitor the change in absorption of the photo-excited sample over time. As mentioned previously, in order to monitor photoinduced phenomena occurring on an ultrafast timescale (femto- to pico- seconds), the time-resolution of both the "pump" and "probe" pulses must be very high (i.e. ultrashort pulses). With the advent of mode-locked laser systems it is now routinely possible to generate laser pulses with a duration of <50 fs to conduct such experiments.

In the Bragg lab, ultrafast laser pulses are generated from a Ti:Sapphire system consisting of two principle components, an ultrafast oscillator and a regenerative amplifier. The oscillator (Mantis, Coherent) generates mode-locked laser pulses centered at 800 nm with 35 fs duration (80 MHz repetition rate). These pulses are used to seed a regenerative amplifier (Legend Elite, Coherent). Pre-amplification begins by passing the seed pulse through a pulse stretcher which temporally broadens (chirps) the pulse by use of diffraction gratings, reducing pulse peak powers to allow for amplification to powers nearing damage thresholds of amplifier optical components. From here a Ti:Sapphire rod is pumped with the output of a 527 nm Nd:YLF laser at a ~1 kHz repetition rate to create a gain medium for amplification of the seed. After 16-17 passes in the laser cavity, amplified pulses are ejected from the amplifier cavity and the spatially chirped pulse is compressed using a grating to recover pulses with time-resolution of 35 fs and pulse energies of 3.5 – 4.0 mJ.

The 800 nm fundamental output is divided using beam splitters and directed down various optical lines for generating our pump and probe pulses. A small portion is sent to either a CaF_2 or Sapphire crystal for generating broadband white light (WL) probe pulses. Sapphire produces a WL continuum that is able to probe further into the NIR and is chosen when wanting to probe

towards 750 nm; CaF_2 produces a WL continuum better for probing towards the near UV. Prior to transmission through the sample, the WL probe passes through a wire-grid polarizer set to magic angle relative to the selected pump pulse polarization to eliminate effects from transient polarization anisotropy (i.e. rotational diffusion) from spectral evolution. Another portion of the fundamental can be diverted to an optical parametric amplifier (Coherent Opera Solo) to generate pump pulses at wavelengths between 290 and 2600 nm by various nonlinear optical processes (discussed below), or to a Barium Borate crystal to generate 400 nm pulses through second harmonic generation (SHG). The pump pulse is then aligned onto a motorized translation stage (Newport) which supports a pair of mounted retroreflector corner cubes (either silver or aluminum reflective mirrors) to precisely control the time delay in which the pump arrives at the sample before the fix probe time delay (time delays up to ~1.6 ns can be gathered at time intervals of ~5 fs).

Each beam is focused and spatially overlapped at the sample (generally in a near colinear geometry); the probe is focused to a spot size of ~100 μm and the pump is separately focused to a spot size that completely encompasses the region of sample being probed (typically ~1-3 mm). After transmission through the sample the probe is collimated and sent through either a long pass or band pass filter before being aligned into a spectrograph and dispersed onto a silicon CCD array camera (Princeton Instruments). Data collection is then performed using a homebuilt LabView acquisition program. For the TAS data discussed in this thesis, four-phase collection measurements were performed for calculation of fluorescence corrected transient absorption spectra. This approach utilizes two optical choppers set to $^1/_2$ and $^1/_4$ the repetition rate of the laser to distinguish four separate phases: $I_{background}$ the background signal measured when both the pump and probe beams are blocked, I_{pump} the scatter and emission signals from the sample when

only the pump is present, I_{probe} intensity when only the probe is transmitted through the sample, and $I_{pump-probe}$ intensity for when the pump and probe both are incident on the sample. Using a variation of Beer's Law, an excited state absorption spectrum can then be determined as the difference spectrum between the ground and excited state according to the following equation:

$$\Delta OD = -log\left(\frac{I_{pump-probe} - I_{pump}}{I_{probe} - I_{background}}\right) \quad (2.2)$$

A detailed description of this experimental setup has been described elsewhere.[1-2] A general schematic of our experimental setup is described in Figure 2.4.

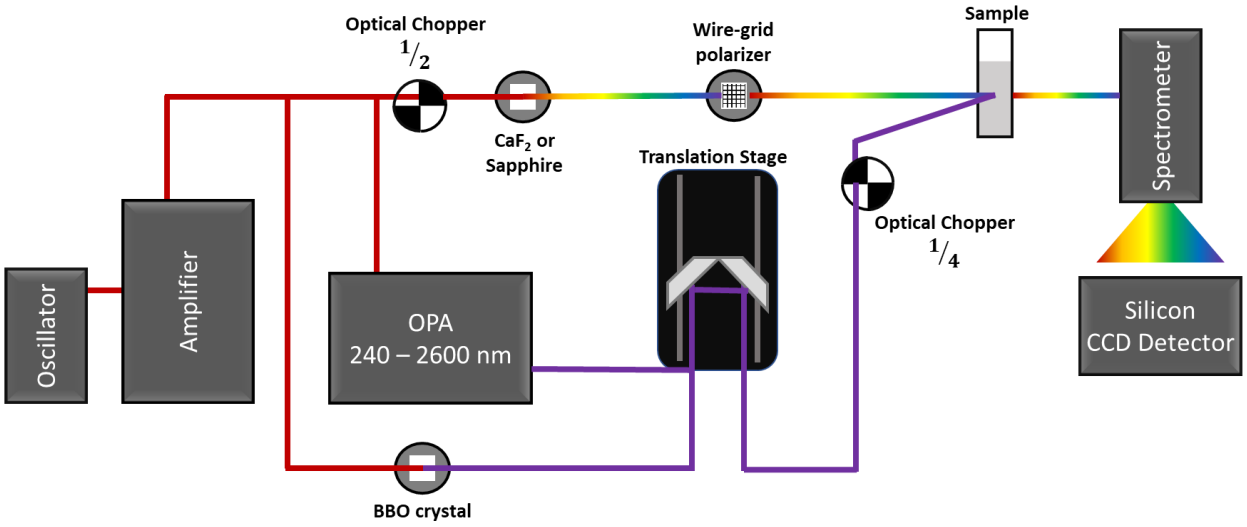

Figure 2.4. Table-top view of transient absorption experiment with various beam paths.

The series of difference spectra collected at a set of time delays provide details of spectral evolution of the excited state after photoexcitation and may contain various positive or negative spectral features. For example, a ground state bleach (GSB) is a negative signal caused by the increase of probe light transmission due to population transfer from the ground state to an excited state upon photoexcitation of the pump; this feature is located in the wavelength range of a steady-state UV-Vis absorption. Another negative feature that may be observed due to an increase in probe transmission is stimulated emission (SE) from an excited state; these spectral features

generally overlap with the wavelength range in which fluorescence is observed. In contrast when there is a pump-induced reduction of probe light transmission, a positive change in optical density occurs and is associated with an excited state absorption (ESA). A representation of these features and an associated energy level diagram is shown in Figure 2.5.

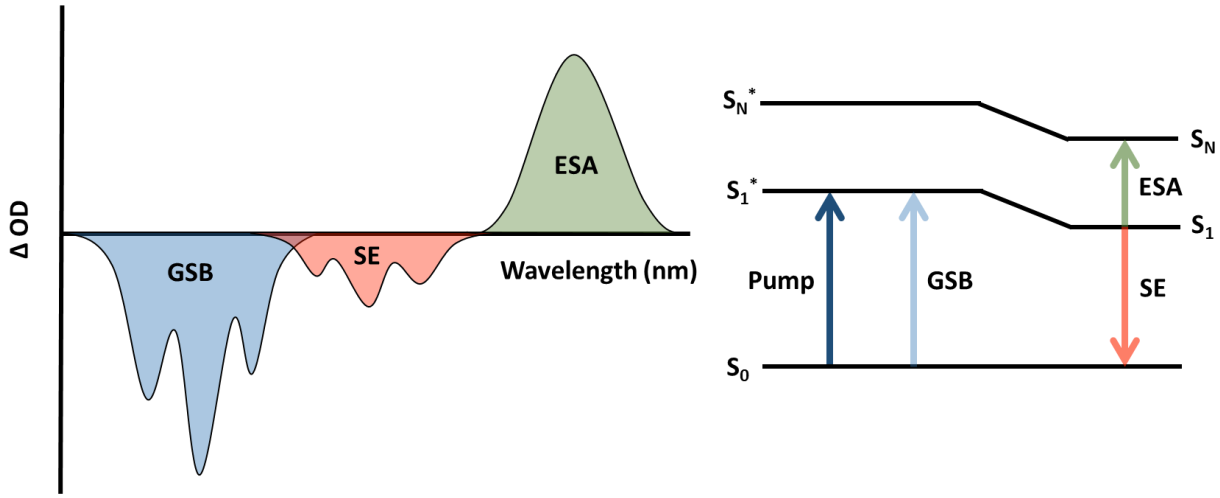

Figure 2.5. Representation of different transient absorption signals (left) for ground state bleach (blue), stimulated emission (red), and excited state absorption (green). The corresponding energy diagram for pump and probe interactions with the sample for each produced signal (right).

2.6 Wavelength Tunability for TAS

To promote a system onto an excited-state surface one must first know its steady-state absorption in order to choose an appropriate wavelength for excitation. For organic molecules this range can vary from UV to visible or to NIR. As described above, for the generation of different energy photons we utilize a femtosecond OPA for generating photons at energies between 290 and 2600 nm using different nonlinear optical mixing processes. The OPA operates by first splitting the 800 nm fundamental into lower energy photons by a process of difference frequency generation to provide photons of different energies that can be used in subsequent nonlinear processes. At sufficient peak powers, when introducing lower energy photons into a nonlinear optical material a higher energy photon can be generated. In the case of SHG, two photons of 800 nm mix and

produce 400 nm, the second harmonic frequency of the fundamental. Third and fourth harmonic generation require additional mixing to generate near-UV and UV photons. Photons of differing energy may also be added through sum-frequency generation. This nonlinear mixing is permitted by the law of conservation of energy, by which the energy of photons emitted by a nonlinear material must be equal to the sum of the input energy. Another consideration for nonlinear mixing is mixing efficiency that arises from "phase matching". This can be view in terms of the law of conservation of momentum. When photon wave vectors are in phase (phase matched) with each other the wave vector of the output photon may have the same magnitude and direction as the resultant of the input mixing photons. Efficiency losses will occur when wave vectors are aligned out of phase. Figure 2.6 presents a diagram for phase matching and nonlinear mixing processes.

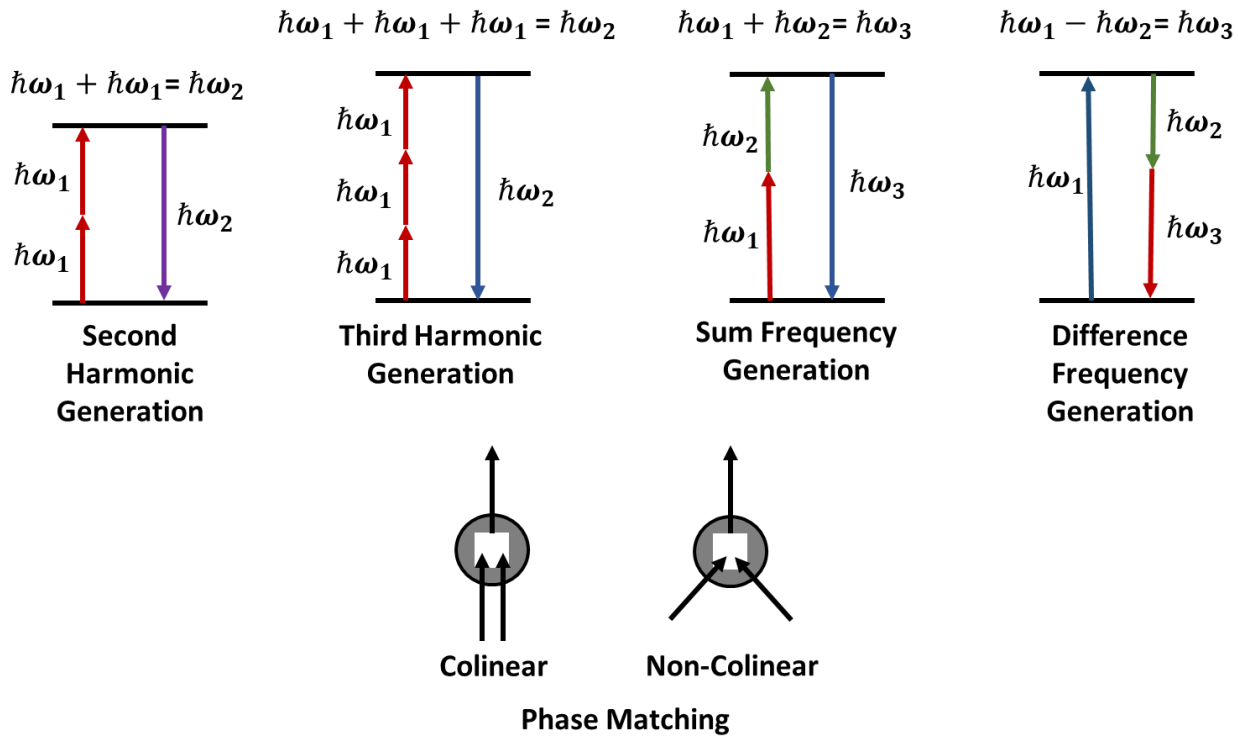

Figure 2.6. Representation of different nonlinear mixing processes (top) demonstrating the law of conservation of energy and phase matching requirements (bottom) by the law of conservation of momentum.

2.7 Data Processing and Fitting Algorithms

Post collection processing of the TAS data is required to further analyze spectral evolution and kinetics. Wavelengths of light across the broadband continuum arrive at the sample at different times due to group velocity dispersion through refractive materials (including the white-light crystals themselves). As a result, redder wavelengths arrive sooner than bluer wavelengths resulting in differences in time zero across the probing window. This can be observed over the course of several hundred femtosecond and is referred to informally as the chirp. To account for this variation, a process of correcting the chirped data is conducted to adjust time zero at each probe wavelength. This is achieved by first finding the time delay at which half the signal intensity (half rise) is observed for each wavelength over the first 1 to 1.5 ps. This wavelength vs time delay data is then fit to a 2^{nd} order polynomial to provide a temporal correction for each probe wavelength. The intensity matrix as a function of these given time delay corrections is then interpolated to a common set of time delays to generate the chirp-corrected data for further kinetic or global analysis.

Post chirp correction, the evolution of spectral transients can be fit to physical models to provide information about the lifetimes of associated transient species. One method is to look at time-dependent intensities for a single or integrated wavelength region of interest and perform a least-squares fitting optimization with respect to a reasonable (exponential) kinetic model. For the experiments described here, sequential state-to-state kinetic models were employed. These kinetic models are convoluted with an instrument response function and include a variable number of exponential decays or rises with a constant background offset to account for species that live beyond the time range that can be probed with our instrument. The instrument response function is a gaussian that contains information about the time-resolution of the experiment (FWHM). The

corresponding FWHM is an effective time-resolution and was typical bound between 0 and 200-250 fs when running the optimization (time-resolution should be better than this upper bound based on previous autocorrelation measurements).

A more rigorous fitting procedure considers the evolution of the entire data matrix through global analysis. Briefly, one starts with principal component analysis (PCA) to investigate weighted principal components, these are eigen solutions (Λ) to the following eigen equation for Y^TY

$$V\,Y^TY = \Lambda\,V \tag{2.3}$$

where Y is the intensity matrix (m by n matrix with rows corresponding to observables (wavelength) and columns to variables (timedelay)). This is possible since the experimental intensity matrix can be described as a linear combination of constant component spectra with relative coefficients based on external parameters (i.e. time). Without further statistical evaluation, alongside prior intuition of the chemical system being studied, the weighted components can qualitatively provide information on how many component species in a model may be required for performing global analysis in order to reproduce experimental data. The data analyzed globally in this thesis involve the use of sequential kinetic models (i.e. A → B, A → B → C, etc.) where the final species are treated as the initial ground state of the systems. When an appropriate model is selected, the following procedure is used for global analysis and is described elsewhere[3]:

1) Define a kinetic matrix "D" for each species in terms of variable parameters and time delay for a given model.
2) Generate a component matrix "E" defined as the following $E = D^TY$.
3) Define initial values for the model's adjustable parameters.

4) Run a nonlinear least squares optimization for the difference between the calculated intensity matrix $D(D^TY)$ and the experimental matrix.

5) Verify model accuracy through goodness of fit (R-squared and fitting of kinetic traces).

The resulting fits then provide excited-state population lifetimes for a given species (species associated difference spectra are generated by using these global minimum values in the fitting parameters to construct the component matrix "E" defined above).

The details above describe a general process for analyzing TAS data and used built in nonlinear least squares fitting algorithms in Matlab. Nonlinear least-squares regression was also involved for processing some steady-state spectroscopic data as discussed in Chapter 3 for determination of CTC equilibrium constants and extinction coefficients. These experiments investigated changes in OD of a CT absorption band as a function of donor concentration (at a constant acceptor concentration), and nonlinear least-squares optimization was performed on absorption data collected at various donor concentrations at a given wavelength to determine K_{CT} and ε from the following[4]:

$$Abs = \frac{\varepsilon}{2}\left[\left(C_A^0 + C_D^0 + \frac{1}{K}\right) - \sqrt{\left(C_A^0 + C_D^0 + \frac{1}{K}\right)^2 - 4C_A^0 C_D^0}\right] \tag{2.4}$$

where C_A^0 and C_D^0 are initial acceptor and donor concentrations. This equation is derived using an equilibrium expression for a donor-acceptor complex with substitution of Beer's Law:

$$K = \frac{C_{AD}}{(C_A^0 - C_{AD})(C_D^0 - C_{AD})} \qquad Abs = C_{AD} l \varepsilon \tag{2.5}$$

2.8 References

1. Molloy, M. S.; Snyder, J. A.; Bragg, A. E., Structural and Solvent Control of Nonadiabatic Photochemical Bond Formation: Photocyclization of O-Terphenyl in Solution. *Journal of Physical Chemistry A* **2014**, *118*, 3913-3925.

2. Yu, W. J.; Magnanelli, T. J.; Zhou, J. W.; Bragg, A. E., Structural Heterogeneity in the Localized Excited States of Poly(3-Hexylthiophene). *Journal of Physical Chemistry B* **2016**, *120*, 5093-5102.

3. Al-Soufi, W.; Novo, M.; Mosquera, M.; Rodriguez-Prieto, F., Principal Component Global Analysis of Series of Fluorescence Spectra. *Reviews in Fluorescence 2009*, Geddes, C. D., Ed. 2011; Vol. 6, pp 23-45.

4. Grebenyuk, S. A.; Perepichka, I. F.; Popov, A. F., Evaluation of the Parameters of 1 : 1 Charge Transfer Complexes from Spectrophotometric Data by Non-Linear Numerical Method. *Spectrochimica Acta Part a-Molecular and Biomolecular Spectroscopy* **2002**, *58*, 2913-2923.

Chapter 3

Solvent Effects on Formation of Donor-Acceptor Charge-Transfer Complexes: N,N'-Diphenyl-N-N'-di-p-tolylbenzene-1,4-diamine (MPDA) and 2,3,5,6-tetrafluoro-7,7,8,8-tetracyanoquinodimethane (F_4TCNQ)

The contents of this chapter and its associated appendix are currently in preparation for journal submission

Brandon J. Barrett, Howard E. Katz, and Arthur E. Bragg

3.1 Abstract

F_4TCNQ (2,3,5,6-tetrafluoro-7,7,8,8-tetracyanoquinodimethane) is a widely used electron acceptor for doping organic semiconductor materials where charge transfer complexes (CTCs) are formed as integer or partial charge separated pairs (ICT vs. PCT). Understanding the effect the local chemical environment has on formation and stabilization of these complexes is therefore important for improving device efficiency. Here we present steady-state and temperature dependent spectroscopic investigations of F_4TCNQ as part of a CTC with the electron donor *N,N'*-Diphenyl-*N*-*N'*-di-p-tolylbenzene-1,4-diamine (MPDA). Equilibrium constants (K_{CT}) for CTC formation were determined via a nonlinear fitting approach for CTCs dissolved in a series of chlorinated solvents. Large formation constants are determined and result from combining strong electron donating and accepting species. An inverse relationship is observed with K_{CT} and solvent dielectric: a lower solvent dielectric is less suited to support charge separation where lower formation constants are observed. Temperature dependent formation constants are determined where enthalpies and entropies of complex formation are evaluated. In high dielectric constant solvents (i.e. 1,2-dichloroethane) complex formation is enthalpically favored. In contrast, with

decreasing dielectric constant, CTCs become unstable enthalpically, with CT formation driven by entropic affects. Chloroform (lowest dielectric constant in the series) is an anomalous case, where favorable formation is observed with a corresponding decrease in entropy. It is suggested inner shell solvent-solute interactions are important for complex formation, where hydrogen bonding is present to stabilize charge separation. We conclude that local dielectric environment plays a critical role for stabilizing charge separation in CTCs and provide insight into how chemical environments may be tuned to support ICT over PCT for film and material applications.

3.2 Introduction

Molecular charge donor and acceptor interactions have recently attracted attention for carrier doping in organic-based optoelectronic materials.[1-3] In many instances donor-acceptor pairs can form ground-state charge-transfer complexes (CTCs), which have distinct electronic and spectroscopic properties: in accordance with Mulliken theory, the highest occupied molecular orbital (HOMO) of the donor and the lowest occupied molecular orbital (LUMO) of the acceptor mix, shifting the dopant energy levels and creating new absorption features that are sensitive to the donor ionization energy and acceptor electron affinity.[4-5] If the LUMO level of the acceptor is sufficiently low compared to the HOMO of the donor, spontaneous integer ground-state charge transfer from donor to acceptor occurs.[1, 6] Integer charge transfer has been used to p-dope conjugated polymers with radical cation polarons, yet even partial charge-transfer arising from the mixing of donor and acceptor energy levels has been demonstrated to improve charge transport in organic materials.

Quinone-based acceptors with large electron affinities have received considerable attention for p-doping organic materials. This group includes 7,7,8,8-tetracyanoquinodimethane (TCNQ), and its fluorinated derivates, such as 2,3,5,6-tetrafluoro-7,7,8,8-tetracyanoquinodimethane (F_4TCNQ). Given the significant increase in electron affinity upon fluorination[1], CTC formation with F_4TCNQ is possible for a broad range of electron donors with varying ionization energies, including polythiophenes (PT), tetrathiafulvavene (TTF), and phenylene diamines. A dominant spectroscopic signature of (integer) CTC formation is the characteristic structured absorption of the F_NTCNQ radical anion which appears in the near infrared (NIR). This has been reported previously for the strong donor-acceptor pairing between *N,N'*-Diphenyl-*N*-*N'*-di-p-tolyl benzene-1,4-diamine (MPDA) and F_4TCNQ, shown in Scheme 3.1, as well as with other donor species.[1, 7-8] These characteristic electronic absorption features, as well as signatures from vibrational absorption spectra (CN stretching mode of F_NTCNQ), are valuable reporters for the degree of charge separation between donors and the F_4TCNQ acceptor.[7, 9-11]

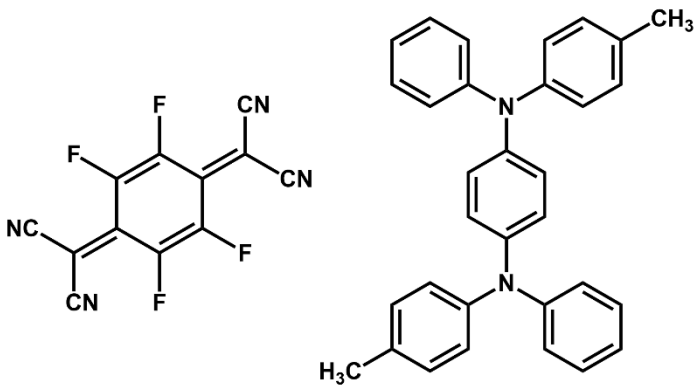

Scheme 3.1. Electron acceptor 2,3,5,6-tetrafluoro-7,7,8,8-tetracyanoquinodimethane (F_4TCNQ, left) and donor *N,N'*-Diphenyl-*N*-*N'*-di-p-tolyl benzene-1,4-diamine (MPDA, right).

F_4TCNQ, in particular, has been used extensively to p-dope organic semiconductor materials, such as poly(3-hexylthiophene-2,5-diyl) (P3HT), to increase charge-carrier densities.[11-

[12] Interestingly, in studies of doped semiconductors both integer and partial charge transfer (ICT vs. PCT) has been observed, where the latter resulted in a decrease in device performance. Studies have shown that an ICT state is formed as the kinetically favored product during film processing but converts to the more thermodynamically favored PCT state.[11] There have been efforts to control the formation of ICT vs PCT present in doped films, as well as controlling the degree of charge transfer, through different approaches to improve device performance.[12-17] For example, acceptor strength has been used to control these in film blends of pentacene and F_4TCNQ or 2,2′-(perfluoronaphthalene-2,6-diylidene)dimalononitrile (F_6TCNNQ): F_4TCNQ has a slightly lower electron affinity and exhibits both ICT and PCT, which is controlled by the mixing ratio; F_6TCNNQ has a higher electron affinity and results only in ICT (but at the cost of a much less stable dopant species).[13] The formation of ICT vs. PCT states may also be overcome by increasing the thermodynamic driving force for charge separation by increasing polaron stabilization; which is observed in ordered vs. disordered regions of polythiophenes.[12] It has also been shown that increasing the doping ratio in PTAA films with F_4TCNQ leads to growth of J-aggregates resulting in ICT, but that excessive doping can lead to a conversion to PCT states in hole transport layers for organic light emitting diodes.[14] Furthermore, the electronic and micro-structure of the polymer influences the density of states for ICT vs PCT.[12]

Although the extent of ICT vs. PCT formation is highly dependent on the relationship between donor IP vs. acceptor EA, the results described above raise questions about the relative stability of CTCs in material environments that are typically characterized by low dielectric constant. This is particularly important for material applications in which the stability of a CT complex is supported by a non- or weakly polar surrounding dielectric material. In prior work we observed an evolution between ICT and PCT states for CTCs based on F_4TCNQ and MPDA doped

in drop-cast films of polystyrene during the course of film processing, which we attribute to reduced stability of a solvent-stabilized integer charge-transfer complex as the film is dried.[7]

With an interest to understand and control the formation of ICT states in films and devices, in this study we have investigated the role of local environment on the stability of integer CTCs. Specifically, we present solvent dependent studies of the strong donor-acceptor pair $F_4TCNQ^{\cdot -}$:$MPDA^{\cdot +}$ to investigate the role the local (solvent) medium has on the stability of complex formation by determining the complex formation constant, K_{CT}. Furthermore, we use temperature-dependent measurements to determine enthalpies and entropies of formation to compare cases of favorable vs unfavorable charge separation and discuss associated interactions for complex stabilization. We make comparisons to calculated free energies for donor/acceptor redox reactions in different solvent media. Collectively our findings highlight the importance the polarity of the local environment has for maintaining fully charge-separated pairs (i.e. ICT) for strong molecular donor-acceptor pairs, as well as provide insight to strategies for creating polymer environments that may favor ICT over PCT.

3.3 Experimental

3.3.1 Sample Preparation.

Dichloroethane (DCE), 1,2-Dichlorobenzene (oDCB), Dichloromethane (DCM), Chlorobenzene (CB), and Chloroform ($CHCl_3$) were purchased from Fischer Scientific and used without further purification. *N,N'*-Diphenyl-*N,N'*-di-p-tolyl benzene-1,4-diamine (MPDA) was purchased from Sigma-Aldrich and used as received. F_4TCNQ was purchased from BOC Sciences (97% purity) and used as received.

Solution samples of integer charge transfer complexes (CTC) were prepared from stock solutions of F_4TCNQ and MPDA for steady-state UV-Vis characterization; solutions were prepared using calibrated micropipettes for additions of each solution and solvent. F_4TCNQ stock solutions were prepared at concentrations near 10^{-5} M; MPDA stock solutions prepared at concentrations between 10^{-4} – 10^{-3} M. CTC solutions were prepared at a constant acceptor concentration but with variable donor concentration by combining 1-2 mL of F_4TCNQ stock with 100 – 850 μL of MPDA stock solution and diluting with solvent to a total solution volume between 4-5 mL.

Room temperature UV-Vis spectra were collected with a diode array spectrometer that is fiber-optically coupled to tungsten and deuterium lamps (Stellarnet). Temperature dependent UV-Vis spectra were collected using a Unisoku UnispeKs CoolSpeK UV USP-203 series cryostat. The fiber optics coupled to our light source(s) and spectrograph were mounted on either side of the sample chamber windows and aligned for collecting transmitted light. A light flow of dry air from a purge generator was introduced into the sample chamber to prevent condensation or window fogging. For temperature-dependent measurements, samples were allowed to equilibrate within the cryostat for 4-5 minutes before collecting spectra (equilibration time was determined based on the temperature difference from room temperature and using the sample heating and cooling rates provided by the manufacturer).

3.3.2 Computations.

Free energies for donor oxidation and acceptor reduction were computed at the DFT-level using the Johns Hopkins Rockfish Cluster and the Orca 4.2.0 software suite. All structure

optimizations applied the M06-L functional with the Ahlrichs basis sets, def2-SVP applied to C and H and def2-TZVPP applied to all other atoms, and the def2/J auxiliary basis set. Solvent environment was modeled using the conductor-like polarizable continuum model (cpcm) with dielectric constants appropriate for each solvent system considered. Vibrational frequency calculations were performed to confirm numerical precision and calculate the enthalpic and entropic contributions to free energy changes.

3.4 Results and Discussion

3.4.1 Solvent-Dependent Formation of $F_4TCNQ^{\cdot -}$:$MPDA^{\cdot +}$ Charge Transfer Complexes (CTCs).

UV-Vis spectra were collected with CTC solutions prepared with a broad range of donor concentrations in order to determine equilibrium constants for complexation. Figure 3.1 plots a series of absorption spectra collected with $F_4TCNQ^{\cdot -}$:$MPDA^{\cdot +}$ CTC solutions in dichloromethane (DCM). All spectra exhibit the characteristic $D_0 \rightarrow D_1$ vibronic absorption features of the F_4TCNQ radical anion. We previously studied this CTC pair and its donor and acceptor species spectroelectrochemically and determined that the MPDA radical cation has a broad, featureless absorption band 600-1100 nm, which overlaps the sharp spectral features of the reduced acceptor.[7] The optical density at 750 nm is plotted in Figure 3.2 as a function of donor concentration for this series. The associated concentrations and optical densities at 750 nm are listed in Table 3.1.

Table 3.1. Initial concentrations of F_4TCNQ and MPDA in DCM with the optical densities measured at 750 nm (c.f. Figures 3.1 and 3.2) for a series of $F_4TCNQ^{\cdot-}$:$MPDA^+$ CTC solutions.

[F_4TCNQ] × 10^{-5} (M)	[MPDA] × 10^{-5} (M)	OD (750 nm)
4.71	3.29	0.524
4.71	6.58	0.663
4.71	9.87	0.884
4.71	13.2	0.925
4.71	16.5	0.990
4.71	19.7	0.986
4.71	23.0	1.014
4.71	26.3	1.030
4.71	29.6	1.057
4.71	32.9	1.078
4.71	36.2	1.066
4.71	39.5	1.098
4.71	42.8	1.083

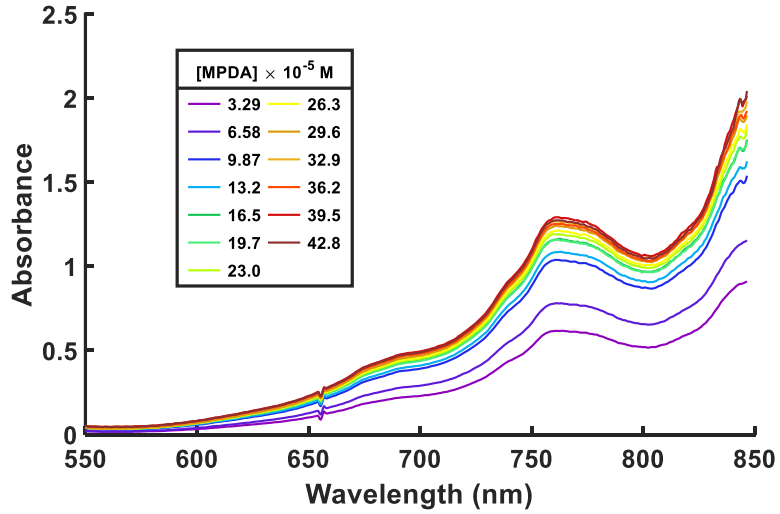

Figure 3.1. Room-temperature UV-Vis absorption spectra collected with solutions of $F_4TCNQ^{\cdot-}$:$MPDA^+$ charge-transfer complexes dissolved in dichloromethane (DCM) at various donor concentrations.

The CTC formation equilibrium is captured by Equation 3.1, in which K_{CT} is the formation constant, C_A^0 and C_D^0 are the initial acceptor and donor concentrations, and C_{AD} is the CTC

concentration at equilibrium. Our measurements of CTC absorption are directly related to C_{AD} by Equation 3.2 (Beer's Law), in which Abs is the concentration-dependent absorbance (OD) and ε is the extinction coefficient of the CTC at a specific wavelength (l is the sample pathlength).

$$K_{CT} = \frac{C_{AD}}{(C_A^0 - C_{AD})(C_D^0 - C_{AD})} \tag{3.1}$$

$$Abs = C_{AD} l \varepsilon \tag{3.2}$$

Equations 3.1 and 3.2 can be used together to derive a (nonlinear) relationship between sample absorbance, formation constant, and initial donor and acceptor concentrations[18]:

$$Abs = \frac{\varepsilon}{2}\left[\left(C_A^0 + C_D^0 + \frac{1}{K_{CT}}\right) - \sqrt{\left(C_A^0 + C_D^0 + \frac{1}{K_{CT}}\right)^2 - 4C_A^0 C_D^0}\right] \tag{3.3}$$

A standard approach for determining formation constants for CTCs is to apply the Benesi-Hildebrand analysis[19] (or related linear-fitting methods[20-23]) to measurements of CTC absorption spectra as a function of donor or acceptor concentration. Benesi-Hildebrand analysis relies on a large excess of donor or acceptor concentration to provide an approximation for the relationship between CTC absorption, donor/acceptor concentration, and ε and K_{CT} of the complex. This has been applied in several studies involving weak donor-acceptor CTCs but has been subject to debate for its drawbacks for accuracy in determination of formation constants.[18, 24-28] An alternative approach is to use nonlinear regression to fit data directly to Equation 3.3. Although this approach does not place strict limits on individual species concentrations or make any approximations, the following inequalities have been proposed to improve reliability in determinations of K_{CT} and ε, assuming $C_D^0 > C_A^0$:

$$0.1C_A^0 < C_{AD} < 0.9C_A^0 \;\; or \;\; 0.1/K < C_D^0 < 0.9/K \tag{3.4}$$

$$0.2 \leq s \leq 0.8 \qquad s = C_{AD}/C_A^0 \tag{3.5}$$

where s is the saturation fraction where it is suggested to analyze at least 75% of the saturation curve.[21, 29] Finally, for improved accuracy in determining K_{CT} and ε by non-linear fitting, it has been reported that 10-15 data points for a fit of Abs vs concentration should be included (which can be over a broad range of donor/acceptor concentrations).[18]

The formation constant for the CT complex in DCM and its extinction coefficient at 750 nm were determined by fitting absorbance data plotted in Figure 3.2 to Equation 3.3 with a nonlinear least-squares regression using Matlab's "fitnlm" command. The resulting fit curve is plotted with experimental data in Figure 3.2. Best-fit values of 4.82×10^4 M^{-1} and 2.42×10^4 M^{-1} cm^{-1} were obtained for K_{CT} and ε, respectively. The large value for the formation constant was expected given the combination of a strong electron-donating and accepting species and the relatively high dielectric constant of the solvent medium that is expected to stabilize charge-separated pairs. We also note that we previously determined the extinction coefficients for $F_4TCNQ^{\cdot -}$ and $MPDA^+$ in Dichloroethane at 750 nm to be 1.9×10^4 and 9.5×10^3 M^{-1} cm^{-1}, respectively, in steady-state while applying a controlled potential electrolysis (i.e. spectroelectrochemical determination).[7] The sum of these values is in reasonable agreement with the fit value for ε (2.48×10^4 vs 2.85×10^4).

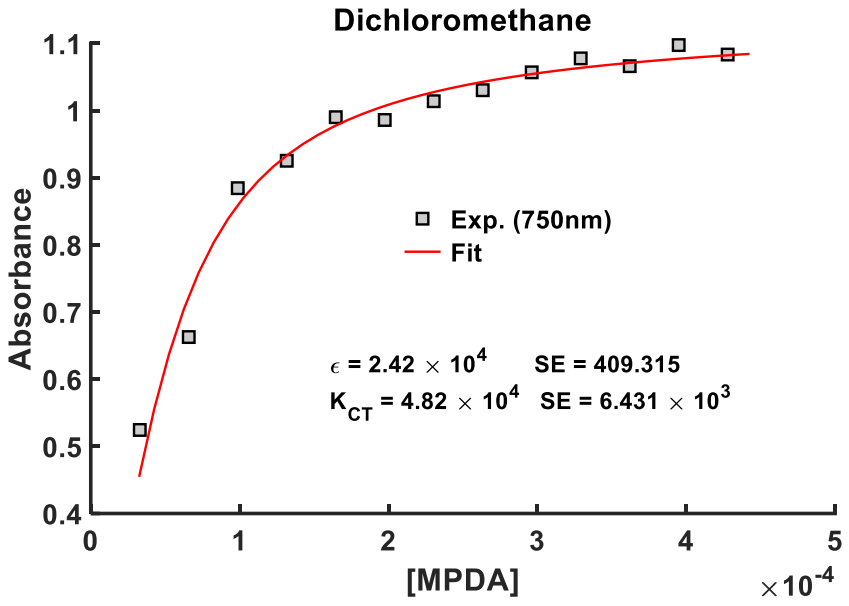

Figure 3.2. Absorbance of $F_4TCNQ^{\cdot-}$:$MPDA^+$ CT complexes in DCM at 750 nm as a function of donor concentration (symbols). The fit to the nonlinear model expressed in Equation 3.3 is overlaid (solid line). Measurements were conducted at room temperature.

To investigate the impact of solvent on complex formation, CTCs were prepared in a collection of solvents with a corresponding range of dielectric constants; complexation constants were determined with the same experimental procedure and analysis presented above. We anticipated a decrease in K_{CT} with decrease in solvent dielectric constant (i.e. solvents of effectively lower polarity are less suited to stabilizing charge-separated pairs), with the goal of determining how low the dielectric constant/solvent polarity can be and still stabilize integer charge transfer between the donor-acceptor pair. Figure 3.3 plots the absorption with donor concentration for CTCs in 1,2-Dichloroethane, 1,2-Dichlorobenzene, Chlorobenzene, and Chloroform; fitting parameters for the series of chlorinated solvents are listed in Table 3.2. Tabulated concentrations and optical densities alongside the individual nonlinear regression fits are provided in Tables and Figures A1.1-A1.4. Within the standard error of the best-determined values for K_{CT}, a decrease in the CTC formation constant is observed when decreasing solvent

dielectric constant for DCE through CB. The formation constant in chloroform deviates from this trend and will be discussed in further detail below in terms of enthalpic and entropic contributions to CTC stabilization.

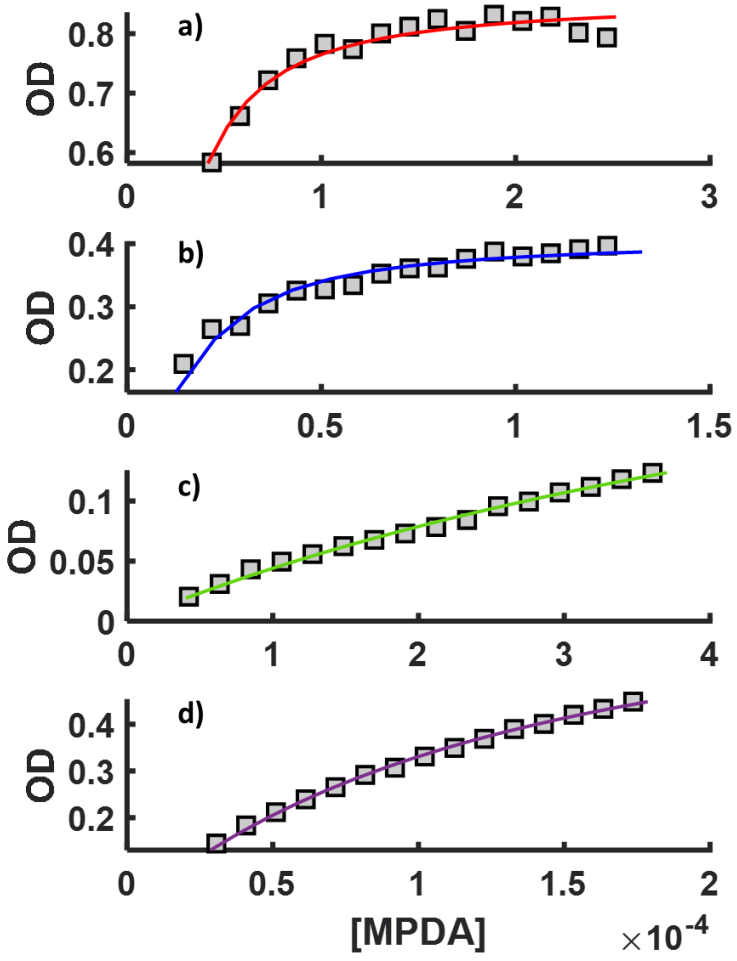

Figure 3.3. Absorption with donor concentration with fits to Equation 3.3 for CTCs in 1,2-Dichloroethane (a), 1,2-Dichlorobenzene (b), Chlorobenzene (c), and Chloroform (d). Fitting parameters are listed in Table 3.2.

Table 3.2. Dielectric constants and best-fit K_{CT} and ε obtained for CTCs in various chlorinated solvents.

Solvent	Dielectric Constant	K_{CT} (M^{-1})	ε (M^{-1} cm^{-1})
1,2-Dichloroethane	10.36	1.15×10^5	2.48×10^4
1,2-Dichlorobenzene	9.93	1.46×10^5	2.06×10^4
Dichloromethane	8.93	4.82×10^4	2.42×10^4
Chlorobenzene	5.62	1.53×10^3	5.93×10^3
Chloroform	4.81	8.66×10^3	2.61×10^4

Computational calculations were performed to compare the combined free-energy change associated with donor oxidation and acceptor reduction to the experimentally determined free energy values determined from K_{CT}. Computational results are presented in Table 3.3. The same qualitative trend is observed: free energy decreases with decrease in solvent dielectric. Furthermore, we have previously reported a change in sign in calculated free energy for charge transfer in toluene, consistent with our observation that no CTCs are formed in toluene solutions.[7] We note that the calculations do not consider the Coulombic interaction between the charged species, nor do they account for entropy changes associated with structure making/breaking associated with solvent-solute interactions.

Table 3.3. Calculated redox potentials for acceptor and donor molecules with the approximated free energy for CTC formation (Δ redox potentials) for comparison to experimentally determined ΔG.

Solvent	$F_4TCNQ/F_4TCNQ^{\cdot -}$ (kcal/mol)	$MPDA^+/MPDA$ (kcal/mol)	Calculated (kcal/mol)	Experimental (kcal/mol)
1,2-Dichloroethane	-117.98	-104.96	-13.02	-6.83
1,2-Dichlorobenzene	-117.88	-106.0	-11.88	-6.97
Dichloromethane	-117.60	-106.48	-11.12	-6.32
Chlorobenzene	-116.32	-108.19	-8.13	-4.30
Chloroform	-115.57	-109.13	-6.44	-5.44
Toluene	-109.94	-113.99	4.05	-

In summary, formation constants and extinction coefficients of $F_4TCNQ^{\cdot-}$:$MPDA^{+}$ CTCs were determined through nonlinear regression. Large K_{CT} values are reported in response to forming favorable CTCs between strong electron donating and accepting molecular pairs. Overall, a trend is observed in K_{CT}, where CTC formation is more favorable in solvents with higher dielectric constants (excluding the special case of chloroform). This trend is also observed qualitatively for calculated reduction energies of charge transfer where solvent is represented as a polarizable continuum. Collectively these results provide insight on the effects local solvent dielectric has for stabilizing charge separation in molecular donor-acceptor pairs.

3.4.2 Temperature Dependence of $F_4TCNQ^{\cdot-}$:$MPDA^{\cdot+}$ CTC Formation

Temperature-dependent UV-Vis measurements were performed for a similar series of CTC solutions to determine enthalpic vs. entropic contributions to the free energy of complexation. Figure 3.4 plots the absorption at 750 nm for a series of CTC solutions in oDCB prepared at various donor concentrations over the range of 22 - 65 °C. An increase in the curvature of the concentration dependence is observed with increasing temperature in this range, which is consistent with an inverse relationship between K_{CT} and temperature. The intensity of the NIR absorption band for the CTCs also behaves similarly (i.e. a decrease in the extinction coefficient as temperature increases) and may be a result of spectral broadening associated with increasing temperature. Fit parameters for each temperature are reported in Table 3.4 and tabulated concentrations and optical densities are reported in Table A1.5.

Table 3.4. Temperature-Dependent values for K_{CT} and ε in 1,2-Dichlorobenzene.

Temperature (K)	K_{CT} (M^{-1})	ε (cm^{-1} M^{-1})
294	1.46×10^5	2.06×10^4
308	9.12×10^4	1.89×10^4
318	7.43×10^4	1.80×10^4
328	5.79×10^4	1.70×10^4
338	4.78×10^4	1.63×10^4

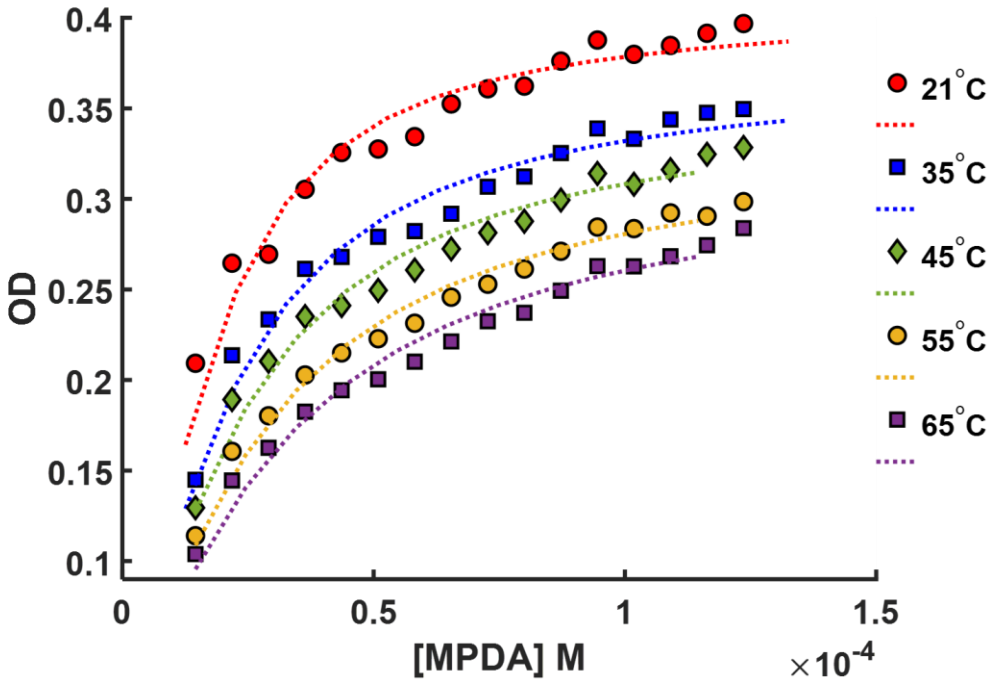

Figure 3.4. Temperature-dependent absorption at 750 nm for $F_4TCNQ^{\cdot -}$:$MPDA^{\cdot +}$ CTCs dissolved in 1,2-Dichlorobenzene prepared at various donor concentrations. Fits to Equation 3.3 are plotted as dashed lines.

These temperature-dependent K_{CT} were used to determine the enthalpy and entropy of formation using Equation 3.6:

$$ln(K_{CT}) = \frac{-\Delta H^{\ddagger}}{RT} + \frac{\Delta S^{\ddagger}}{R} \tag{3.6}$$

Temperature-dependent measurements in CB and $CHCl_3$ were also collected to compare thermodynamic parameters in the case of favorable vs unfavorable CTC formation, as well as providing insight to the unexpected favorability for forming CTCs in $CHCl_3$. The concentration/absorbance data and corresponding plots are presented in Tables A1.6-A1.9 and Figures A1.5-A1.6. Figure 3.5 presents the fits to each solvent's temperature dependent data according to Equation 3.6 and the resulting values for enthalpies and entropies of formation are listed in Table 3.5.

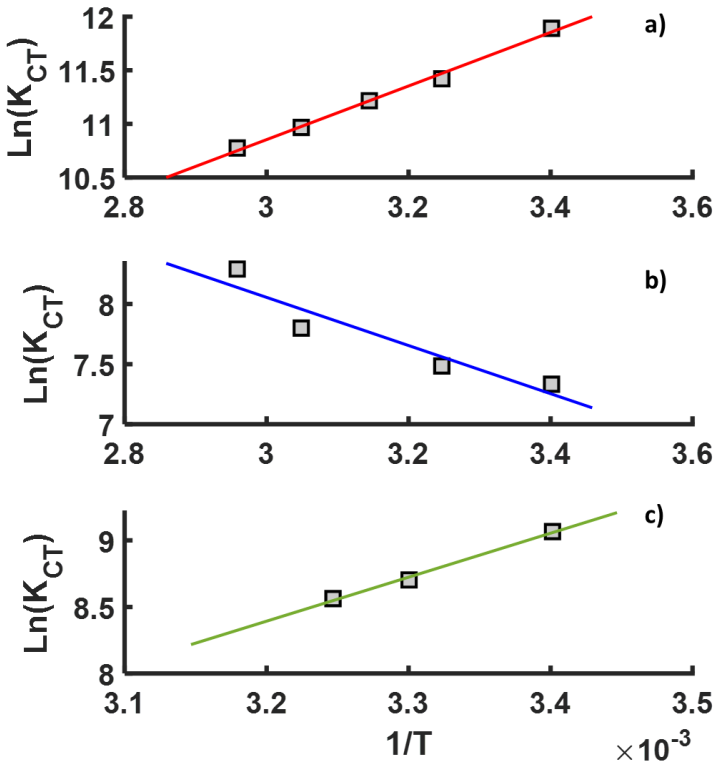

Figure 3.5. Temperature-dependence of K_{CT} for CTCs in 1,2-Dichlorobenzene (a), Chlorobenzene (b), and Chloroform (c). Enthalpies and Entropies are determined from slope and intercept values according to Equation 3.6.

Table 3.5. Entropies and enthalpies obtained from temperature dependent fits presented in Figure 3.5.

Solvent	Dielectric Constant	$\Delta H^{\ddagger}$ (kcal mol^{-1})	$\Delta S^{\ddagger}$ (kcal mol^{-1} K^{-1})
1,2-Dichlorobenzene	9.93	-4.97	0.0067
Chlorobenzene	5.62	3.98	0.028
Chloroform	4.81	-6.52	- 0.0043

For CTC formation in oDCB, where large formation constants are observed, a negative ΔH and small positive ΔS were obtained. This signifies that CTC formation is highly stabilized and exothermic in the higher polarity solvents which can support charge separation. In contrast, in chlorobenzene, where complex formation is less favorable, a smaller positive ΔH is observed with a ΔS that is ~ 4 times larger than in oDCB. As a result of decreasing solvent polarity (which is less suited to support charge separation), CTC formation is endothermic but entropically favored (driven by changes in local solvent structure breaking) to still allow charge transfer to occur.

Chloroform is the interesting case where K_{CT} increases in a solvent environment with a lower dielectric constant (and lower polarity). Here we observe formation of CTCs to be enthalpically favored, with a larger ΔH than in oDCB, but with a negative ΔS. The larger change in enthalpy is suggested to be a result of a stronger binding between donor and acceptor.[26] One scenario may be the introduction of hydrogen bonding for complex stabilization with chloroform, which would result in increased solvent ordering around the charge pair complex compared to the neutral donor-acceptor pair to explain the decrease in entropy.[30] It has been mentioned that if non-bonding interactions are important for complex stabilization an increase in the formation constant should be observed when decreasing solvent polarity due to solvent-solute interactions competing with ion-pair interactions in complex stabilization.[24] This is observed when comparing $CHCl_3$ to

CB, where ion-pair interactions should be favored in the more polar solvent because charge separation is better supported.

3.5 Conclusion

Solvent effects on charge transfer complex formation between a strong phenylene-diamine donor (MPDA) and strong electron acceptor (F_4TCNQ) have been characterized. Application of a numerical nonlinear regression has allowed determination of formation constants (K_{CT}) and extinction coefficients (ε) of the CTC based on changes in absorption of the CTC band across a series of concentration dependent samples in chlorinated solvents. It is observed that decreases in solvent polarity (i.e. decreasing the ability to support charge separated pairs based on solvent-solute interactions) result in a decrease in K_{CT}, with $CHCl_3$ being an anomalous case. Temperature dependent measurements provided information on the thermodynamic contributions of enthalpy and entropy to CTC formation. Negative ΔH and positive ΔS values are reported in high polarity solvents, resulting in favorable charge separation that is supported by local solvent where ion-pair interactions contribute to ground-state complex stability. In contrast, in low polarity solvents, where charge separation should be less supported, CTC's are entropically favored and still undergo spontaneous charge separation. The exception to this trend in dielectric stabilization of CTC's is chloroform, with the largest reported ΔH and the only negative ΔS. These results suggest non-bonding interactions contribute to complex stability where hydrogen bonding is proposed to further stabilize the complex. We previously reported no observation of charge separation for this donor-acceptor pair in toluene, which is a solvent representative of dielectric environments in films and materials. As integer charge transfer among such donor-acceptor complexes is sought after to improve performance across a range of applications in organic optoelectronics, these results

provide insight into how local dielectric environment may be tuned (through chemical functionality) to support charge separation for such applications in organic optoelectronics.

3.6 References

1. Zhang, J.; Xu, W.; Sheng, P.; Zhao, G. Y.; Zhu, D. B., Organic Donor-Acceptor Complexes as Novel Organic Semiconductors. *Accounts of Chemical Research* **2017**, *50*, 1654-1662.

2. Goetz, K. P.; Vermeulen, D.; Payne, M. E.; Kloc, C.; McNeil, L. E.; Jurchescu, O. D., Charge-Transfer Complexes: New Perspectives on an Old Class of Compounds. *Journal of Materials Chemistry C* **2014**, *2*, 3065-3076.

3. Wang, W.; Luo, L. X.; Sheng, P.; Zhang, J.; Zhang, Q. C., Multifunctional Features of Organic Charge-Transfer Complexes: Advances and Perspectives. *Chemistry-a European Journal* **2021**, *27*, 464-490.

4. Mulliken, R. S., Molecular Compounds and Their Spectra. II. *Journal of the American Chemical Society* **1952**, *74*, 811-824.

5. Mulliken, R. S., Molecular Compounds and Their Spectra 3. The Interaction of Electron Donors and Acceptors. *Journal of Physical Chemistry* **1952**, *56*, 801-822.

6. Méndez, H., et al., Doping of Organic Semiconductors: Impact of Dopant Strength and Electronic Coupling. *Angewandte Chemie International Edition* **2013**, *52*, 7751-7755.

7. Barrett, B. J.; Saund, S. S.; Dziatko, R. A.; Clark-Winters, T. L.; Katz, H. E.; Bragg, A. E., Spectroscopic Studies of Charge-Transfer Character and Photoresponses of F_4TCNQ-Based Donor-Acceptor Complexes. *Journal of Physical Chemistry C* **2020**, *124*, 9191-9202.

8. Ma, L.; Hu, P.; Jiang, H.; Kloc, C.; Sun, H.; Soci, C.; Voityuk, A. A.; Michel-Beyerle, M. E.; Gurzadyan, G. G., Single Photon Triggered Dianion Formation in TCNQ and F_4TCNQ Crystals. *Scientific Reports* **2016**, *6*, 28510.

9. Kampar, E.; Neilands, O., Degree of Charge Transfer in Donor–Acceptor Systems of the Π–Π Type. *Russian Chemical Reviews* **1986**, *55*, 334-342.

10. Meneghetti, M.; Pecile, C., Charge-Transfer Organic-Crystals - Molecular Vibrations and Spectroscopic Effects of Electron-Molecular Vibration Coupling of the Strong Electron-Acceptor $TCNQF_4$. *Journal of Chemical Physics* **1986**, *84*, 4149-4162.

11. Watts, K. E.; Neelamraju, B.; Ratcliff, E. L.; Pemberton, J. E., Stability of Charge Transfer States in F_4TCNQ-Doped P3HT. *Chemistry of Materials* **2019**, *31*, 6986-6994.

12. Neelamraju, B.; Watts, K. E.; Pemberton, J. E.; Ratcliff, E. L., Correlation of Coexistent Charge Transfer States in F_4TCNQ-Doped P3HT with Microstructure. *The Journal of Physical Chemistry Letters* **2018**, *9*, 6871-6877.

13. Theurer, C. P.; Richter, M.; Rana, D.; Duva, G.; Lepple, D.; Hinderhofer, A.; Schreiber, F.; Tegeder, P.; Broch, K., Coexistence of Ion Pairs and Charge-Transfer Complexes and Their Impact on Pentacene Singlet Fission. *Journal of Physical Chemistry C* **2021**, *125*, 23952-23959.

14. Cui, M. K.; Rui, H. S.; Wu, X. M.; Sun, Z.; Qu, W. X.; Qin, W. J.; Yin, S. G., Coexistent Integer Charge Transfer and Charge Transfer Complex in F4-TCNQ-Doped PTAA for Efficient Flexible Organic Light-Emitting Diodes. *Journal of Physical Chemistry Letters* **2021**, *12*, 8533-8540.

15. Stanfield, D. A.; Wu, Y.; Tolbert, S. H.; Schwartz, B. J., Controlling the Formation of Charge Transfer Complexes in Chemically Doped Semiconducting Polymers. *Chemistry of Materials* **2021**, *33*, 2343-2356.

16. Salzmann, I.; Heimel, G.; Oehzelt, M.; Winkler, S.; Koch, N., Molecular Electrical Doping of Organic Semiconductors: Fundamental Mechanisms and Emerging Dopant Design Rules. *Accounts of Chemical Research* **2016**, *49*, 370-378.

17. Jiang, H.; Hu, P.; Ye, J.; Zhang, K. K. K.; Long, Y.; Hu, W. P.; Kloc, C., Tuning of the Degree of Charge Transfer and the Electronic Properties in Organic Binary Compounds by Crystal Engineering: A Perspective. *Journal of Materials Chemistry C* **2018**, *6*, 1884-1902.

18. Grebenyuk, S. A.; Perepichka, I. F.; Popov, A. F., Evaluation of the Parameters of 1 : 1 Charge Transfer Complexes from Spectrophotometric Data by Non-Linear Numerical Method. *Spectrochimica Acta Part a-Molecular and Biomolecular Spectroscopy* **2002**, *58*, 2913-2923.

19. Benesi, H. A.; Hildebrand, J. H., A Spectrophotometric Investigation of the Interaction of Iodine with Aromatic Hydrocarbons. *Journal of the American Chemical Society* **1949**, *71*, 2703-2707.

20. Scott, R. L., Some Comments on the Benesi-Hildebrand Equation. *Recueil Des Travaux Chimiques Des Pays-Bas-Journal of the Royal Netherlands Chemical Society* **1956**, *75*, 787-789.

21. Deranleau, D. A., Theory of Measurement of Weak Molecular Complexes .I. General Considerations. *Journal of the American Chemical Society* **1969**, *91*, 4044-+.

22. Foster, R.; Hammick, D. L.; Wardley, A. A., Interaction of Polynitro-Compounds with Aromatic Hydrocarbons and Bases .11. A New Method for Determining the Association Constants for Certain Interactions between Nitro-Compounds and Bases in Solution. *Journal of the Chemical Society* **1953**, 3817-3820.

23. Scatchard, G., The Attractions of Proteins for Small Molecules and Ions. *Annals of the New York Academy of Sciences* **1949**, *51*, 660-672.

24. McKim, W. D.; Ray, J.; Arnold, B. R., Analysis of the Association Constants for Charge-Transfer Complex Formation. *Journal of Molecular Structure* **2013**, *1033*, 131-136.

25. Arnold, B. R.; Euler, A.; Fields, K.; Zaini, R. Y., Association Constants for 1,2,4,5-Tetracyanobenzene and Tetracyanoethylene Charge-Transfer Complexes with Methyl-Substituted Benzenes Revisited. *J. Phys. Org. Chem.* **2000**, *13*, 729-734.

26. Baniyaghoob, S.; Najafpour, M. M.; Boghaei, D. M., Charge-Transfer Complexes of 4-Nitrocatechol with Some Amino Alcohols. *Spectrochimica Acta Part a-Molecular and Biomolecular Spectroscopy* **2010**, *75*, 970-977.

27. Jalilov, A. S.; Lu, J. J.; Kochi, J. K., Charge-Transfer Complex Formations of Tetracyanoquinone (Cyanil) and Aromatic Electron Donors. *J. Phys. Org. Chem.* **2016**, *29*, 35-41.

28. Varukolu, M.; Palnati, M.; Nampally, V.; Gangadhari, S.; Vadluri, M.; Tigulla, P., New Charge Transfer Complex between 4-Dimethylaminopyridine and DDQ: Synthesis, Spectroscopic Characterization, DNA Binding Analysis, and Density Functional Theory (DFT)/Time-Dependent DFT/Natural Transition Orbital Studies. *Acs Omega* **2022**, *7*, 810-822.

29. Person, W. B., A Criterion for Reliability of Formation Constants of Weak Complexes. *Journal of the American Chemical Society* **1965**, *87*, 167-&.

30. Al-Ahmary, K. M.; Alenezi, M. S.; Habeeb, M. M., Spectroscopic Investigation and Computational Analysis of Charge Transfer Hydrogen Bonded Reaction between 3-Aminoquinoline with Chloranilic Acid in 1:1 Stoichiometric Ratio. *Journal of Molecular Structure* **2015**, *1098*, 377-392.

Chapter 4

Spectroscopic Studies of Charge-Transfer Character and Photoresponses of F_4TCNQ-based Donor-Acceptor Complexes

The contents of this chapter and its associated appendix are published in *J. Phys. Chem. C* 2020, 124, 17, 9191–9202.

Brandon J. Barrett, Simran S. Saund, Rachel A. Dziatko, Tylar L. Clark-Winters, Howard E. Katz, and Arthur E. Bragg

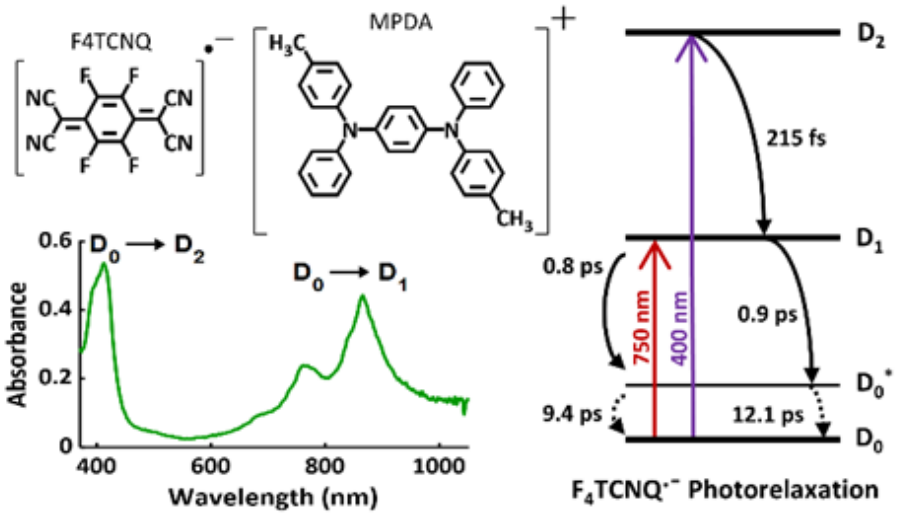

4.1 Abstract

F_4TCNQ (2,3,5,6-tetrafluoro-7,7,8,8-tetracyanoquinodimethane) is used widely as a hole-doping agent in photoresponsive organic semiconducting materials, yet relatively little is known about the photoresponses of the $F_4TCNQ^{\cdot-}$ anion generated via doping. Furthermore, there is still relatively little systematic exploration of how the properties of the local material or chemical environment impacts the driving force for generating these charge-transfer complexes. Here we

present spectroscopic and photophysical studies of F_4TCNQ in charge-transfer complexes (CTCs) with the electron donor *N,N'*-Diphenyl-*N*-*N'*-di-p-tolylbenzene-1,4-diamine (MPDA) both in dichloroethane solution and polystyrene matrices. Integer charge transfer (ICT) between donor and acceptor occurs readily in dichloroethane solvent to form $F_4TCNQ^{\cdot-}$:$MPDA^+$ CTCs, due to a ~150 mV difference in $MPDA^+$/MPDA and $F_4TCNQ/F_4TCNQ^{\cdot-}$ reduction potentials. Ultrafast spectroscopic studies of the CTC as well as electrochemically generated $F_4TCNQ^{\cdot-}$ and $MDPA^+$ reveal that the photoresponses of these CTCs are dominated by that of the dopant anion, including rapid deactivation (800 fs) after excitation to the anion D_1 excited state, followed by slower (~10 ps) vibrational cooling in the anion D_0 state. Excitation to the higher-lying D_2 state results in a rapid relaxation to the D_1 state, in contrast to direct D_2-D_0 relaxation previously observed for $F_4TCNQ^{\cdot-}$ in gas phase. CTCs embedded in polystyrene (PS) matrices are observed to lose their integer charge-transfer character upon evaporation of solvent, as evidenced by changes to electronic and vibrational absorption features associated with $F_4TCNQ^{\cdot-}$. This change is attributed to the loss of solvent stabilization of the ion pair formed through the charge-transfer reaction. Ultrafast spectral measurements reveal that the photoresponses of the partial charge-transfer (PCT) species embedded in PS are still highly similar to those of the ICT species and unlike that of neutral F_4TCNQ, implying the electronic properties of the PCT state are likewise dominated by properties of the reduced acceptor molecule. We conclude that excitation of ICT or PCT states introduces optical losses for photoresponses of doped organic semiconductor materials due to the large anion absorption cross section and its rapid, dissipative deactivation dynamics.

4.2 Introduction

Organic molecular charge dopants have attracted much attention given their potential for enhancing charge-carrier densities in organic field-effect transistors (OFETs),[1-2] organic light emitting diodes (OLEDs),[3-4] and organic semiconductors (OSC) in general.[5-6] The strongly electron-accepting quinone chromophore 7,7,8,8-tetracyanoquinodimethane (TCNQ) is considered a benchmark molecular charge dopant and has been studied extensively.[7-10] Organic donor-acceptor charge-transfer (CT) salts, such as the salt formed between tetrathiafulvalene (TTF) and TCNQ, were first discovered in the 1960s[11] and were found to exhibit the largest known electrical conductivities in organic materials.[12-13] Fluorinated derivatives of TCNQ including 2,3,5,6-tetrafluoro-7,7,8,8-tetracyanoquinodimethane (F_4TCNQ), which is shown in Scheme 4.1, have since been demonstrated to have even higher electron affinities than TCNQ itself,[14] enabling CT complex or salt formation with a broader range of donor compounds (such as the donor *N,N'*-Diphenyl-*N*-*N'*-di-p-tolylbenzene-1,4-diamine or "methylphenyl phenyl phenylenediamine," MPDA, shown in Scheme 1). Here, we describe efforts to better understand the relative stability and photoresponses of $F_4TCNQ^{\cdot-}$ based charge-transfer complexes.

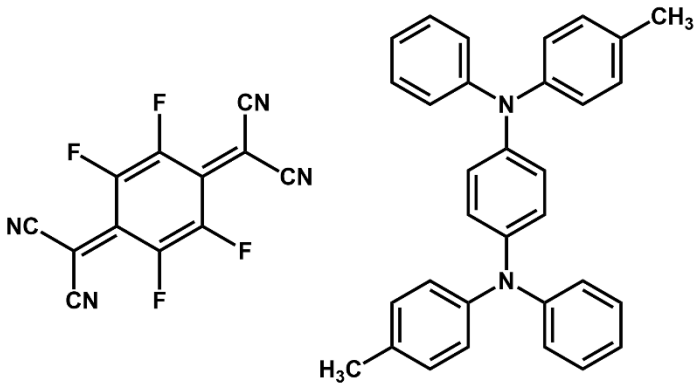

Scheme 4.1. Electron acceptor 2,3,5,6-tetrafluoro-7,7,8,8-tetracyanoquinodimethane (F_4TCNQ, left) and donor *N,N'*-Diphenyl-*N*-*N'*-di-p-tolyl benzene-1,4-diamine (MPDA, right).

Research on molecular doping of organic materials has aimed to tune electronic properties of the dopant,[14-17] control crystal structure for optimizing dopant interactions and the degree of charge transfer,[17-19] improve doping and material processing methods,[20-23] and examine behaviors of doped materials for applications requiring insulating,[12, 24] semiconducting,[16, 25-26] conductive[27-28] and superconductive materials.[29-30] Recently F_4TCNQ has been investigated widely as a p-type dopant for conjugated polymer films, such as poly(3-hexylthiophene-2,5-diyl) (P3HT), and organic semiconducting devices based on these materials,[31-34] with much attention given to the doping efficiency and the properties of the doped organic semiconductors. Electron transfer from OSC to dopant generates free charge carriers (holes) with a corresponding increase in material conductivity. It has been reported that charge separation in F_4TCNQ-doped P3HT films initially produces an integer charge transfer (ICT) state; the ICT state exhibits the characteristic but overlapping electronic absorption features of $F_4TCNQ^{\cdot-}$ and P3HT polarons[32] in the near-infrared (NIR). p-type doping of conjugated polymers by ICT generates both "free" valence and "trapped" inter-bandgap polarons;[32, 34] in a recent study Schwartz's group showed evidence for delocalization of polarons in F_4TCNQ-doped P3HT films present in both forms. Tolbert, Schwartz and coworkers have further shown that hole mobilities in P3HT doped with F_4TCNQ or electron deficient dodecaborane compounds are improved due to doping-induced changes in polymer stacking.[35-37] However, it has also been shown that the ICT state of these doped materials subsequently converts to a thermodynamically preferred partial charge transfer (PCT) state over the course of weeks, as verified by time-dependent changes in CN stretching frequencies and N 1s electron binding energies determined by Fourier transform infrared spectroscopy (FTIR) and X-ray photoelectron spectroscopy (XPS), respectively.[33] Studies with F_4TCNQ-doped regioregular (rr) P3HT and regiorandom (rra) P3HT have further revealed that the microstructure and electronic

structure of the polymer influences the donor density of states available for ICT vs. PCT formation.[38]

At the same time, there also has been interest in the properties of the dopant anions $F_4TCNQ^{\cdot -}$ and F_4TCNQ^{2-}.[39-44] The electronic structure of $F_4TCNQ^{\cdot -}$ has received considerable attention because it supports multiple bound electronic states (a rare feature for an anion). Calculations by Simons et al.[45] revealed that the ground anionic state (D_0, 1^2B_{2g}) possesses a planar D_{2h} symmetry, similar to that of the neutral but with changes in bond alternation induced by the electron in the pi-antibonding singly occupied molecular orbital (SOMO). The lowest-lying bound excited state (D_1, 1^2B_{3u}) involves a core-electron excitation ($\pi^2 1\pi^{*1} \rightarrow \pi^1 1\pi^{*2}$), with a minimum-energy structure characterized by twisting of the cyano groups out of the plane of the central ring. The second bound excited state (D_2, 2^2B_{3u}) involves a valence-electron excitation ($\pi^2 1\pi^{*1} \rightarrow \pi^2 2\pi^{*1}$), and is characterized by a non-planar structure in which the fluorine substituents lie above and cyano groups bend below the plane of the central ring. The $D_0 \rightarrow D_1$ and $D_0 \rightarrow D_2$ transitions both possess large oscillator strengths and are responsible for the characteristic absorption features of $F_4TCNQ^{\cdot -}$ observed in the near-IR and near-UV, respectively[42] (*vide infra*). A third bound excited state was calculated (D_3 1^2A_g); spectroscopic transition from D_0 to this state has a vanishingly small oscillator strength.[41]

The existence of multiple bound, electronically excited states with significantly different minimum-energy geometries presents the possibility for nonadiabatic, nonradiative deactivation following photoexcitation of $F_4TCNQ^{\cdot -}$. Verlet's group previously examined the photoresponses of $F4TCNQ^{\cdot -}$ in the gas phase with time-resolved photodetachment spectroscopy.[41] In their experiments they selectively excited each of the two lowest-lying anion excited electronic states and determined that the D_1 and D_2 states rapidly relax with lifetimes of 190 fs and 60 fs,

respectively. Furthermore, their results indicated that the nonradiative relaxation of D_2 occurs directly to the ground state rather than cascading via D_1. Similar studies by their group with $TCNQ^{\cdot-}$ and negatively charged para-benzoquinone revealed excited-state lifetimes of 650 fs and < 40 fs.[46-47] The rapid deactivation timescales observed in all cases suggest that nonradiative relaxation through conical intersections (CIs) may be common to quinone-based anions in gas phase.

The photophysical properties of the dopant species in condensed phase environments have been explored only lightly, and relatively little is known about the photoresponses of $F_4TCNQ^{\cdot-}$ in charge-transfer complexes and doped materials. To our knowledge, the only investigations of this sort were reported by Ma et al., who used transient absorption spectroscopy to study photoresponses of $TCNQ^{\cdot-}$ in acetonitrile (generated by charge disproportionation or charge transfer to the solvent) excited to the lowest-lying D_1 excited electronic state.[48] These authors reported decay of D_1 via internal conversion with a ~2 ps lifetime (much slower than is observed in the gas phase), with a small quantum yield for relaxation to a state presumed to be charge-transfer in character (proposed to be of possible dianion character) that exhibits a lifetime of ~20 ps. The $TCNQ^{\cdot-}$ concentration studied in that work was quite low, such that it was only possible to examine relaxation from the D_1 state due to spectral overlap of higher-lying transitions with those of neutral TCNQ. [In other work, these authors demonstrated that photogenerated anion is an intermediate to forming F_4TCNQ^{2-} in crystalline F_4TCNQ,[43] but to our knowledge no one has studied the photophysical dynamics of $F_4TCNQ^{\cdot-}$ explicitly.] While this work demonstrates qualitative consistency with behaviors in gas phase, relevant issues that remain largely unexplored include whether state-specific deactivation dynamics observed in the gas-phase also occur in the condensed phase, whether photoinduced charge recombination is possible in CT pairs, how the

deactivation dynamics of this dopant anion are impacted by the local chemical environment (e.g. solvent/matrix polarity as well as presence of the counterion), and if/how the photoresponses of dopant anion represents an absorption loss for light-driven applications with doped OSC materials.

Herein we present condensed phase studies (solution and film) of the photoresponses of charge-transfer complexes of $F_4TCNQ^{\cdot -}$. We report responses for the anion as part of (i) an integer charge transfer state in solution and (ii) a partial charge transfer state in a polystyrene matrix. We use transient absorption spectroscopy to directly probe relaxation dynamics of selectively excited D_1 and D_2 anion states and draw comparisons to previous gas- and solution-phase studies. Furthermore, we use the sensitivity of the charge-transfer interaction to local chemical environment to interrogate how the photophysical properties of CT complexes compare in ICT vs. PCT states. Due to absorption overlap with the polaron absorption, $F_4TCNQ^{\cdot -}$ photoresponses are difficult to address from studies of e.g. doped P3HT films. Thus, not only are these results relevant for understanding fundamental photophysical properties of $F_4TCNQ^{\cdot -}$ and how they are modified by chemical environment, they also provide insight to photoresponses of F_4TCNQ-based charge-transfer complexes in molecular doped OSCs, as the complexes studied here can be viewed as models for relevant doping interactions.

4.3 Experimental

4.3.1 Sample Preparation

Dichloroethane (DCE) was purchased from Fischer Scientific (99.9% purity) and used without further purification. *N,N'*-Diphenyl-*N,N'*-di-p-tolyl benzene-1,4-diamine (MPDA) and 1,4-Bis(diphenylamino)benzene (97% purity) (PDA = MPDA without the methyl substituents) were purchased from Sigma-Aldrich and used as received. F_4TCNQ was purchased from BOC

Sciences (97% purity) and used as received. Polystyrene (PS, avg. MW 35,000) was purchased from Sigma-Aldrich and purified via reprecipitation by mixing a solution of PS in dichloroethane dropwise to a methanol bath (1:10 by volume).

Solution-phase samples for transient absorption were prepared with a concentration of 0.15 mM F_4TCNQ, with excess MDPA or PDA donor (~0.2 or 0.5 mM for studies with 750 or 400 nm photoexcitation, respectively), to form $F_4TCNQ^{\cdot -}$ as part of a charge transfer complex (CTC) in solution. UV-Vis spectra were collected with a diode array spectrometer that is fiber-optically coupled to tungsten and deuterium lamps (Stellarnet). Solution samples used in laser experiments were circulated through a 1 mm path length quartz flowcell, resulting in an optical density (OD) of approximately 0.35 and 0.8 at 750 and 400 nm, respectively. UV-Vis spectra of solutions were taken before and after irradiation at each excitation wavelength to track any photochemical changes. Notably, F_4TCNQ also absorbs near 400 nm, and we therefore used excess donor concentrations (0.5 mM) in order to increase the fraction of $F_4TCNQ^{\cdot -}$ and consequently minimize contributions to our transient measurement from direct excitation of F_4TCNQ at this wavelength. Transient absorption measurements were also conducted with neutral F_4TCNQ, prepared at similar concentrations (~0.14 mM) in dichloroethane, as a control to differentiate/identify any contributions to our measured signals from neutral dynamics at this excitation wavelength.

Thin films of CTC-doped PS were prepared by drop-casting solutions of CTC and PS codissolved in dichloroethane solution. Purified PS was dissolved in dichloroethane at a concentration of 100 mg/ml. F_4TCNQ and MPDA concentrations were determined such that doped PS films would be 15% CTC by weight after solvent evaporation. Films were cast on indium tin oxide (ITO) coated glass substrates and dried in a petri dish under room conditions. Film samples had optical densities of approximately 0.2 at 750 nm and were rastered relative to

the laser beams for transient spectroscopic measurements using a small automated translation stage to eliminate the possibility for laser damage. FTIR spectra of thin films were measured using a Mattson Infinity Series FTIR with an EG&G Judson MCT detector. Solutions were drop-cast and dried onto the same region of a NaCl salt plate five consecutive times. Spectra were measured in transmission mode under a dry-air purge for 250 accumulations at a 4 nm resolution.

Solutions for collection of spectroelectrochemistry measurements were prepared as follows. Individual F_4TCNQ and MPDA solutions were prepared in dichloroethane at 0.13 mM and 0.092 mM, respectively, for controlled potential electrolysis (CPE). Separate CTC solutions were prepared at (1) 0.12 mM F_4TCNQ with excess MPDA and (2) 0.091 mM MPDA with excess F_4TCNQ for CPE neutralization measurements. Finally, individual solutions of F_4TCNQ and MPDA were prepared at 0.15 mM and 0.085 mM, respectively, for collecting transient absorption measurements of isolated $F_4TCNQ^{\cdot -}$ and $MPDA^{+}$. All of these sample solutions contained supporting electrolyte and were used in a honeycomb electrochemical cell, the details of which are discussed below.

4.3.2 Spectroelectrochemistry

Spectroelectrochemical measurements were conducted using a PINE Research Au honeycomb working electrode, with an integrated Au counter electrode and $Ag/AgNO_3$ (10 mM) reference electrode; potentials were controlled with a BASI Epsilon potentiostat, and corrected for the $Fc^{+/0}$ redox couple. Spectra were collected on an Agilent Cary 60 UV-Vis spectrophotometer with a Xe flash lamp. All solutions contained 100 mM tetrabutylammonium hexafluorophosphate ($TBAPF_6$) as the supporting electrolyte. The same spectroelectrochemical cell and conditions were

utilized for ultrafast measurements of electrochemically generated donor cations and acceptor anions for comparisons with photoresponses of the charge-transfer complexes.

Cyclic voltammograms for the donor and acceptor compounds were obtained independently with an Ivium-n-Stat potentiostat, in the presence of 100 mM $TBAPF_6$ supporting electrolyte, under an N_2 atmosphere, with a 3 mm diameter CH Instruments glassy carbon working electrode, Pt wire counter electrode, and Ag pseudo-reference electrode. The working electrode was polished with 1 μm alumina slurry deposited on a micro-polishing pad. All potentials were corrected for internal ferrocene at the end of the experiment, and solution resistance was partially compensated for using in-situ methods.

4.3.3 Computations

Computations of redox free energies were performed on the Maryland Advanced Research Computing Cluster, using the Orca 4.2.0 software suite.[49-50] All optimizations applied the M06-L functional with the Ahlrichs basis sets,[51-52] def2-SVP applied to C and H and def2-TZVPP applied to all other atoms, and the def2/J auxiliary basis set[53]. Solvent was modeled using the conductor-like polarizable continuum model (cpcm) with standard parameters applied for toluene, and a dielectric strength of 10.36 to model structures in dichloroethane. Vibrational frequency calculations were performed to confirm numerical precision and calculate the enthalpic and entropic contributions to free energy.

4.3.4 Transient Absorption Spectroscopy (TAS)

The setup for our transient absorption measurements have been described in detail elsewhere,[54-55] and here we describe specific experimental details for the work presented. Ultrafast

excitation and probe pulses were generated using the amplified output of a Ti:Sapphire laser (Coherent Legend Elite, 3.8 mJ/pulse, 1kHz repetition rate, ~35 fs pulse duration). The 400 nm pulses used for photoexcitation were generated by doubling the 800 nm fundamental with a barium borate (BBO) crystal. NIR pulses at 750 nm were obtained through second harmonic generation of the NIR signal obtained from an optical parametric amplifier (OPA, Coherent OperaSolo). Broadband probe pulses were obtained via white light generation in a 2 mm calcium fluoride (CaF_2) crystal (390-750 nm, 850-1100 nm). Probe pulses were passed through a wire-grid polarizer (Thorlabs) set at magic angle (54.7°) with respect to the pump pulse polarization and placed immediate before the sample in order to eliminate time dependent polarization effects. The spot size of the probe pulse at the sample was roughly 100 μm, whereas pump pulses were focused to a spot size of about 1 mm. The pump pulse energy was 4 μJ or less for measurements with solutions and 1 μJ or less for thin films; no dependence on pump fluence was observed in this regime.

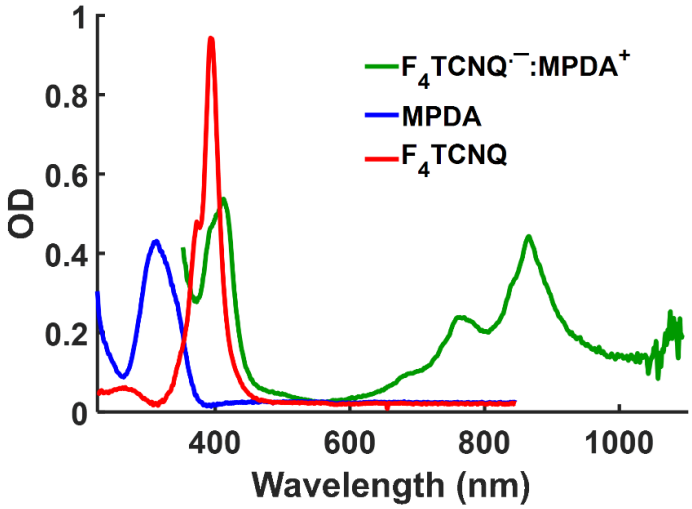

Figure 4.1. UV-Vis spectra of MPDA (blue), F_4TCNQ (red), and the $F_4TCNQ^{\cdot-}$:$MPDA^+$ charge transfer complex (green). [Separate spectroelectrochemical measurements for $F_4TCNQ^{\cdot-}$ and $MPDA^+$ are presented in Appendix 2.]

4.4 Results and Discussion

4.4.1 Steady-state spectroscopy and electrochemistry of donor, acceptor, and charge-transfer complexes in solution

Figure 4.1 presents steady-state absorption spectra for MPDA (donor, blue), F_4TCNQ (acceptor, red), and $F_4TCNQ^{\cdot-}$:$MPDA^+$ CTCs (green) dissolved in dichloroethane. Neutral F_4TCNQ exhibits a strong absorption peak at 393 nm, whereas the lowest-energy absorption feature of the donor species peaks at 312 nm. The absorption spectrum of the CTC exhibits the characteristic vibronic progression between 700 and 900 nm that is associated nominally with the vertical $D_0\left(1^2B_{2g}\right) \rightarrow D_1\ (1^2B_{3u})$ transition for $F_4TCNQ^{\cdot-}$ as well as a feature at 412 nm that corresponds with the anion's vertical $D_0\left(1^2B_{2g}\right) \rightarrow D_2\ (2^2B_{3u})$ transition. We note that under similar sample preparation that $F_4TCNQ^{\cdot-}$:PDA^+ CTCs exhibit identical features, with sample variations in the optical density of both bands that we ascribe to differences in the solubilities of the two donors, and therefore their abilities to form CTCs with F_4TCNQ in solution.

Table 4.1. $E_{1/2}$ potentials determined by cyclic voltammetry for redox reactions of F_4TCNQ and MPDA in dichloroethane (relative to Fc^+/Fc).

Redox couple	$E_{1/2}$ (V)
$F_4TCNQ^{2-}/F_4TCNQ^{\cdot-}$	-0.475
$MPDA^+/MPDA$	0.030
$F_4TCNQ^{\cdot-}/F_4TCNQ$	0.155
$MPDA^+/MPDA^{2+}$	0.575

Cyclic voltammetry (CV) was utilized to determine the reduction potentials for $MPDA^+$ and F_4TCNQ and therefore the favorability (i.e. thermodynamic driving force) for donor-to-

acceptor charge transfer in dichloroethane solution. A composite voltammogram obtained with separate solutions of F_4TCNQ and MPDA is presented in Figure A2.1. We find that the $MPDA^+$/MPDA and $F_4TCNQ/F_4TCNQ^{\cdot-}$ reduction potentials are extremely close (approaching a difference of ~150 mV) and consistent with a spontaneous charge separation in dichloroethane solution. As noted further below, charge-transfer complexes could not be formed spontaneously in toluene (a much less polar solvent), which reflects the need for polar solvent-solute interactions to stabilize the charge pair in solution relative to a positive change in free energy upon charge transfer; we consider this further below in the context of CTC-doped PS films. A summary of reduction and oxidation potentials associated with the cyclic voltammogram presented in Figure A2.1 is reported in Table 4.1.

Spectro-electrochemistry was utilized to assess contributions from the donor cation and acceptor anion to the steady-state absorption spectra of charge-transfer complexes. Measurements were conducted using controlled potential electrolysis (CPE), with the potential held constant at relevant values for generating specific electrochemical species (as determined from CV). Spectro-electrochemical results from the reduction of F_4TCNQ at a potential relevant for generation of only $F_4TCNQ^{\cdot-}$ are presented in Figure A2.2(a); these show the growth of the distinct vibronic progression in the near-IR region that is associated with the lowest-energy absorption transition of $F_4TCNQ^{\cdot-}$ (signatures of the acceptor dianion appear at reduction potentials much higher than used for CPE). Spectro-electrochemical data obtained under conditions for single oxidation of the donor also reveals broad, featureless absorption features in the near IR and near UV (Figure A2.2(b)), indicating that the steady-state absorption of the CT complex plotted in Figure 4.1 must have overlapping contributions from both species.

In order to determine extinction coefficients for both species at excitation wavelengths used in transient absorption measurements, spectroelectrochemical studies of the charge-transfer complex were conducted in which we selectively neutralized either the donor cation or the acceptor anion by applying a controlled potential electrolysis as indicated in Figure A2.3. These solutions for selective neutralization of donor cation or acceptor anion contained excess F_4TCNQ or MPDA, respectively. This condition ensured that (1) the limiting reagent was present in its ionic form as part of a CTC, and (2) that electrolysis conditions would not change the concentration of the ionic charge-transfer partner. Under this condition the absorption features remaining after neutralization of either the donor cation or acceptor anion by CPE at an appropriate potential corresponds to the absorption of the counterpart at the concentration of the limiting reagent. We consequently determined that the extinction coefficients at 750 nm to be 9.5×10^3 $M^{-1}cm^{-1}$ for $MPDA^+$ and 1.9×10^4 $M^{-1}cm^{-1}$ for F_4TCNQ^-. A similar determination at 400 nm is not possible due to the overlap with the lowest-energy absorption feature of neutral F_4TCNQ. In order to determine the relative extinction coefficients of the two charged species at 400 nm we considered the relative optical densities at 750 nm and 400 nm from the spectroelectrochemistry of each individual species. We similarly find that the relative extinction coefficients at 400 nm are roughly 2:1 F_4TCNQ^-:$MPDA^+$.

Finally, we make note of photochemistry that can be observed with the 400-nm excitation of CTC solutions that is mitigated by use of a flow cell. UV-Vis spectra were collected before and after irradiation of a solution of CTC at 400 nm (under conditions of transient measurements) using both a flow cell and a 2 mm cuvette. When using a cuvette, a new absorption feature grows in around 480 nm (with a loss of neutral absorption below 400 nm) after prolonged 400-nm photoexcitation. We ascribe this new feature to a product of photoreactions between excited

neutral F_4TCNQ with the organic solvent or possibly with the donor species. Similar photoreactivity for F_4TCNQ^* was reported from Moulé and coworkers and utilized for optical de-doping of F_4TCNQ-doped P3HT films: as a result of irradiating at 405 nm, a soluble photoproduct is formed between neutral F_4TCNQ and tetrahydrofuran (THF).[31] While similar photoreactivity may occur to some degree with the 400-nm excitation of our samples, we note that use of a flow cell in transient measurements with both CTCs and neutral F_4TCNQ eliminated any spectral signatures of the buildup of such a photoproduct.

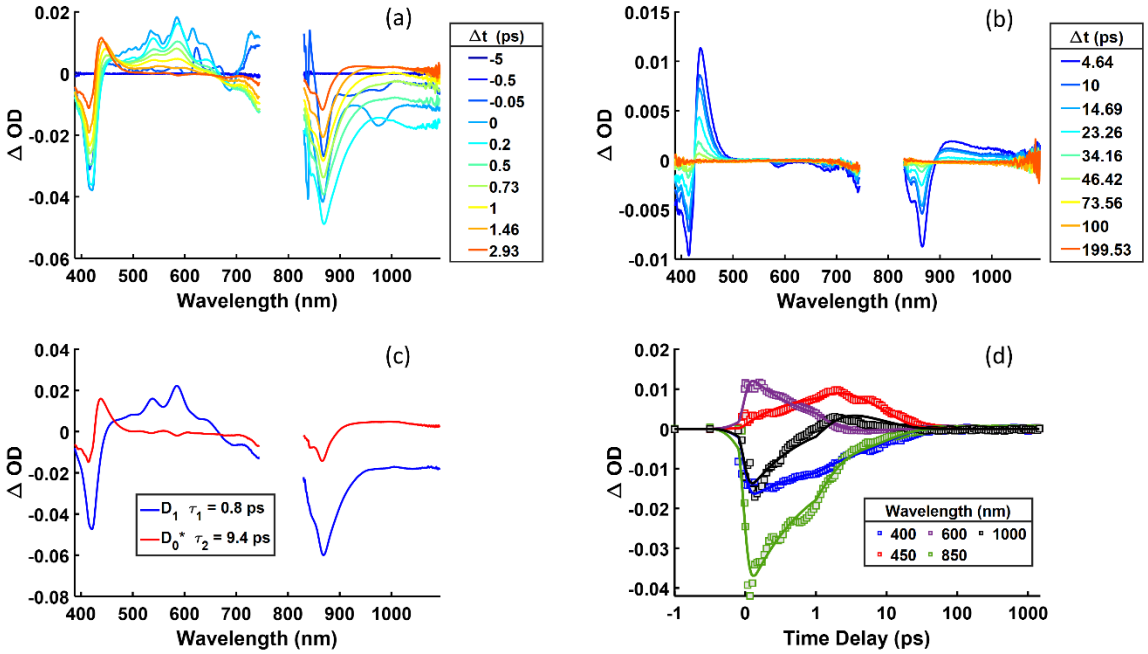

Figure 4.2. Transient absorption spectroscopy of $F_4TCNQ^{\cdot-}$:$MPDA^+$ dissolved in dichloroethane with 750-nm excitation (nominally, $F_4TCNQ^{\cdot-}$ $D_0 \rightarrow D_1$). Transient absorption shown (a) before and (b) after 3 ps. (c) Species associated spectra and (d) selected fits to kinetic traces obtained from global analysis.

4.4.2 Excitation energy-dependent photoresponses of ICT CTCs in solution

Figure 4.2(a-b) presents results from transient absorption measurements conducted with 750-nm excitation of $F_4TCNQ^{\cdot-}$:$MPDA^+$ CTCs dissolved in dichloroethane. Transient spectra are

characterized by negative bands at 416 nm and 868 nm that correspond with bleaching of the steady-state absorption features of the complex (ground state bleach, GSB). We also observe regions of photoinduced absorption (PIA, positive signals) at 500-650 nm for delays shorter than 3 ps (Figure 4.2(a)) and centered around 435 nm and 950 nm for delays longer than 3 ps (Figure 4.2(b)). The photoinduced absorption and bleach features fully decay and recover, respectively, under 750 nm excitation. All of these features are qualitatively similar to those observed previously for excitation of $TCNQ^{\cdot-}$ in acetonitrile.[48]

The absorption between 500-650 nm appears within our temporal response and has well-defined vibronic structure. We assign this feature to an excited-state absorption (ESA) of the photoprepared anion D_1 state to a higher-lying electronic level of the dopant anion. Verlet's group previously reported time dependent density functional theory (TD-DFT) calculations for vertical energy gaps to excited states starting from the optimized D_{2h} $\left(1^2B_{2g}\right)$ $F_4TCNQ^{\cdot-}$ ground state.[41] Their results are consistent with previous calculations by Simons for three bound excited states; these authors also identified another bound configuration that lies between 2^2B_{3u} and ^2A_g with ^2A_u symmetry (this state was found to be unbound in Simon's calculations). The vertical gap between the 1^2B_{3u} D_1 state and the ^2A_g state is consistent with the absorption maximum for the visible feature observed in our transient measurements at time delays < 3 ps; furthermore, the ^2A_g state has the correct symmetry for a dipole-allowed vertical transition from D_1. Notably, the ESA features we observed following 750 nm excitation of $F_4TCNQ^{\cdot-}$ in CTCs are much sharper than those observed in the study by Ma et al. with $TCNQ^{\cdot-}$. We postulate that this difference could be manifestations of charge-transfer dynamics in the terminal ^2A_g state that are correlated with differences in the binding energy for this state (^2A_g is more weakly bound for $TCNQ^{\cdot-}$).

In contrast, the "differential" transient spectral feature observed at later time delays (>3 ps) are highly evocative of a transient population of D_0 in a vibrational hot state. A vibrationally hot ground-state anion would exhibit hot-band absorption at lower energy (longer wavelength) relative to both bleach features in the near-IR and near-UV. Assignment of these spectral features to a vibrationally hot ground state is consistent with signatures of vibrationally hot D_0 observed in Verlet's time-resolved photodetachment measurements with $TCNQ^{\cdot -}$.

In order to quantify the timescales associated with these spectral dynamics, transient spectra were fit globally to a simple kinetic model convoluted with our instrument response. As two spectral patterns/species can be distinguished directly from the data, the following kinetic scheme was applied to data collected with 750 nm photoexcitation:

$$D_1 \xrightarrow{\tau_{IC}} D_0^* \xrightarrow{\tau_{vib}} D_0 \qquad (4.1)$$

where D_1 is $F_4TCNQ^{\cdot -}$ in its first bound excited state, which undergoes ultrafast relaxation (internal conversion, IC) to a hot vibrational ground state D_0^* ; the vibrationally hot ground state subsequently cools through vibrational energy transfer to the solvent. Figure 4.2(c) plots species-associated difference spectra (with respect to D_0) for D_1 and D_0^*; fits to transient data at selected probe wavelengths are plotted in 4.2(d). Based on this model, D_1 relaxes through ultrafast electronic relaxation with a lifetime of 0.8 ps, and the vibrationally hot ground state populated by internal conversion cools with a lifetime of 9.4 ps. As noted above, similar transient species have been observed in pump-probe measurements of $TCNQ^{\cdot -}$ under 750 nm excitation.[48] Based on these similarities with our data, we argue the same photodeactivation processes (ultrafast IC followed by vibrational cooling in D_0) most likely also occur for $TCNQ^{\cdot -}$ without need to invoke existence of an intermediate charge-transfer state.

Although the spectral dynamics observed following 750-nm excitation of the CT complex are consistent with prior reports of ultrafast dynamics in $TCNQ^{\cdot -}$, we recognize that transient spectral features shown in Figure 4.2 should likely include contributions from both the photoexcited acceptor anion and donor cation due to the overlap of their steady-state absorption features noted above. We therefore undertook a series of transient absorption measurements of electrochemically generated $F_4TCNQ^{\cdot -}$ and $MPDA^+$ to measure explicitly the ultrafast spectral dynamics associated with solutions containing each half of the CT complex. Figure A2.4 presents transient data obtained for $F_4TCNQ^{\cdot -}$ prepared by CPE at -0.310 V. Figure A2.5 presents species associated spectra (SAS) and fits at selected probe wavelengths obtained by global spectral analysis of transient absorption data (subject to the model in Equation 4.1). The spectral dynamics observed are remarkably similar to those collected with the solution of CTCs, exhibiting a highly structured transient absorption in the visible that decays on an 800 fs lifetime as well as spectral features consistent with a vibrationally hot ground state following electronic deactivation. Transient absorption data obtained with electrochemically generated $MPDA^+$ (prepared by CPE at 0.190 V) are presented in Figure A2.6, with results of global spectral analysis presented in Figure A2.7. In contrast to the acceptor anion, photoexcited donor cation has very weak absorption features at best in the visible at time delays < 3 ps (with earliest spectra and SAS 1 dominated by coherent artifacts), but exhibits bleach signatures in the near UV and IR that match the positions of the steady-state absorption spectrum of the cation. Thus, the similarity in shape and timescales observed in the spectral evolution of PIA from both the CTC and electrochemically generated anion (and dissimilarity with the cation) support our assignments above. Notably, transient spectral evolution for both the anion and the cation exhibit signatures of vibrational cooling in the ground state following rapid excited-state deactivation (Figure A2.4(b) and Figure A2.6(b)). We

therefore can infer that the vibrational relaxation timescale determined for CTC complex reflects contributions from both species, albeit dominated by anion contributions due to its larger absorption cross section at the excitation wavelength.

To examine the state-dependence of anion relaxation dynamics, transient absorption measurements were also conducted with 400 nm excitation of $F_4TCNQ^{\cdot -}$:$MPDA^+$ CTCs; transient spectra are presented in Figures 4.3(a-b). Bleach, ESA, and vibrationally hot ground-state absorption (GSA) features similar to those seen in Figures 4.2(a-b) are observed in the visible and NIR regions. Two noticeable differences with data collected with 750-nm excitation include: 1) the ESA at 500-650 nm lacks sharp vibronic structure with 400 nm excitation, and 2) a residual bleach below 400 nm and a weak absorption at 950 nm persists on the longest timescales of our measurements (~1-2 ns).

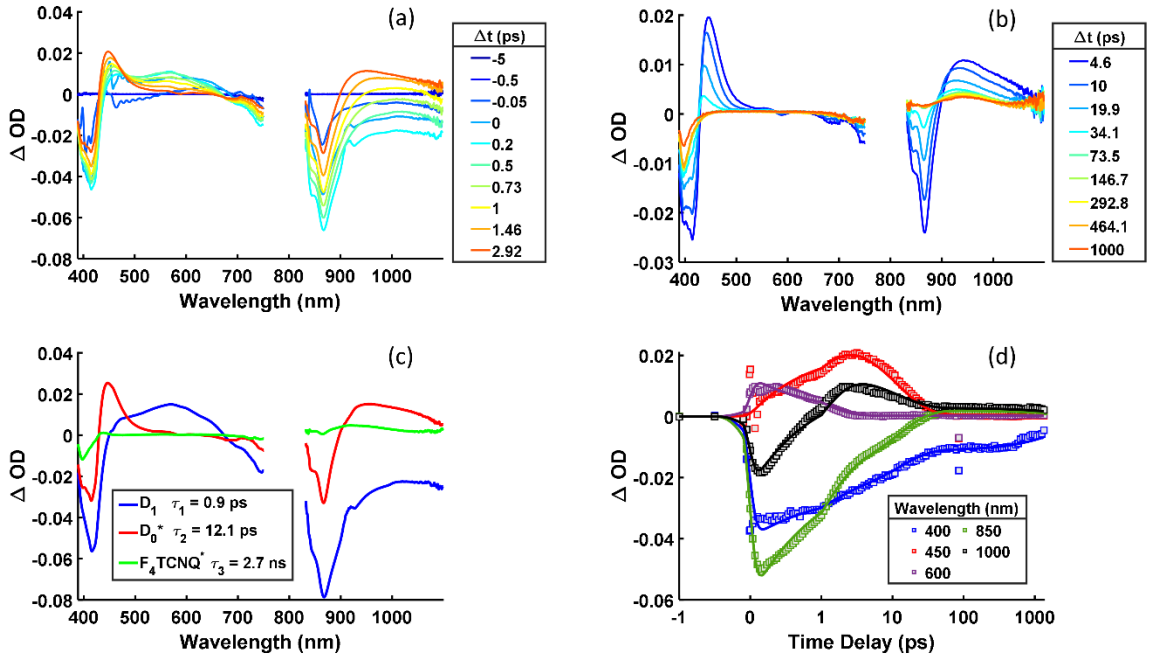

Figure 4.3. Transient absorption spectroscopy of $F_4TCNQ^{\cdot -}$:$MPDA^+$ dissolved in dichloroethane with 400-nm (nominally, $F_4TCNQ^{\cdot -}$ $D_0 \rightarrow D_2$) excitation. Transient absorption shown (a) before and (b) after 3 ps. (c) Species associated spectra and (d) selected fits to kinetic traces obtained from global analysis.

The long-lived bleach and absorption features are attributable to excitation of some neutral F_4TCNQ present in solution. When compared to transient spectra collected with 750-nm excitation of the anion (Figure 4.2), there is a noticeable shift of the GSB at 400 nm towards the absorption peak for neutral F_4TCNQ, whereas little to no shift is observed in the anion bleach around 865 nm; this difference supports that the bleach signal observed in this region with the higher excitation energy arises from simultaneously exciting the overlapping transitions of the neutral and anion. To further assess the scale of this contribution, we conducted TAS measurements with F_4TCNQ at 400 nm (transient data presented in Figure A2.8; results of global analysis presented in Figure A2.9). Both a sharp bleach feature at 400 nm and the broad absorption at 950 nm remain 1 ns after 400 nm excitation of F_4TCNQ, and both features line up with the small features observed at similar time delays after 400 nm excitation of the CTC solution. Although this indicates that 400 nm excitation is not 100% selective for excitation of the CTC, we note that 1) TAS signals measured for the CTC solution are overwhelmingly dominated by CTC (i.e. $F_4TCNQ^{\cdot -}$) transient features, 2) the excited-state features of F_4TCNQ evolve very slowly (100s of ps), and not on timescales observed in the relaxation of $F_4TCNQ^{\cdot -}$ when excited selectively at 750 nm, and 3) no significant features appear in the visible (500-700 nm) in the TA spectra for neutral F_4TCNQ. In total, this means that spectral dynamics following 400 nm excitation of $F_4TCNQ^{\cdot -}$ dominate the transient data presented in Figures 4.3(a-b).

The transient spectra in Figure 4.3(a-b) also were fit globally, but with an inclusion of an extra component to account for the long-lived transient that is populated through direct excitation of some neutral F_4TCNQ. Component spectra and fits to transients at selected wavelengths are shown in Figure 4.3(c-d). Notably, the first two component spectra are highly similar to those obtained with 750 nm excitation, with the exception that the transient absorption in the visible

(450-650 nm) lacks the sharp vibronic structure at this higher excitation energy. When compared to the sharp ESA vibronic progression seen in Figure 4.2(c), the appearance of this broadened feature indicates that a vibrationally hot D_1 state is rapidly populated following selective excitation to D_2 (on timescales comparable or approaching experimental time resolution). Global fits recover lifetimes of 0.9 ps and 12.1 ps for D_1-to-D_0 internal conversion and D_0 vibrational cooling associated with F4TCNQ$^{\cdot-}$. The internal conversion lifetime is comparable to that observed with 750-nm excitation; we attribute the somewhat longer-lived vibrationally hot ground state to the greater excess vibrational energy in D_0 obtained with photoexcitation to D_2.

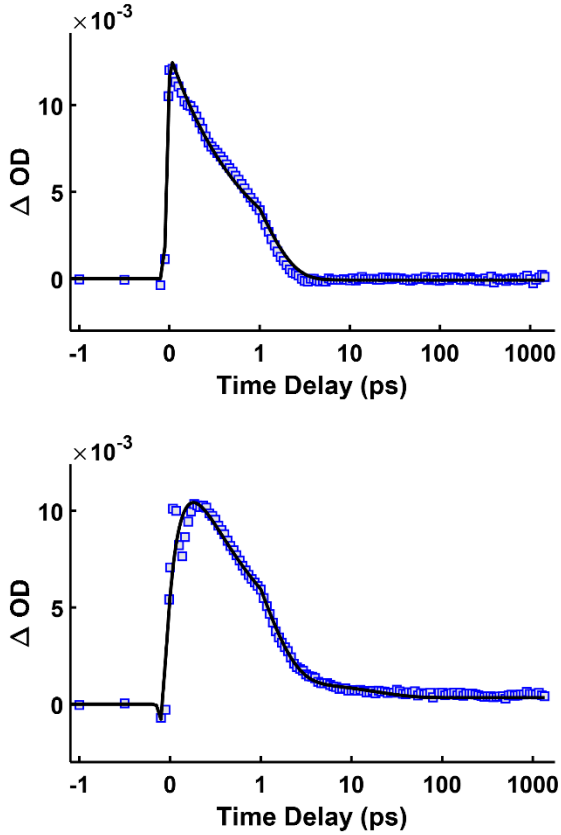

Figure 4.4. Exponential fits to decay of excited-state absorption features measured for $F_4TCNQ^{\cdot-}$:$MPDA^+$ dissolved in dichloroethane with 750-nm (top) and 400-nm (bottom) excitation. The kinetic traces are averaged over the 500 nm-600 nm to cover the region of the ESA. An ultrafast signal rise is required to fit data collected with 400-nm excitation.

We note that we attempted to fit this data globally with a kinetic model incorporating a rapid internal conversion between D_2 to D_1, but that this produced nonsensical component spectra for D_2 due to coherent spectral artifacts that appear around time zero. However, the plausibility for a rapid D_2 to D_1 internal conversion is supported by a comparison of time-dependent traces through transient spectra averaged over the ESA band (500-650 nm) under 400 nm and 750 nm excitation, as presented in Figure 4.4. Here it can be seen that a rapid signal induction (~215 fs) is observed after photoexciting the D_2 state (note, that some of this rise follows the appearance of the coherent artifact/spike appearing at time zero); the decay of this signal was fit with a bi-exponential fitting function with lifetimes of 0.9 ps and 18.5 ps; the longer timescale is a minor component (~5%) that accounts for spectral intensity of vibrational hot D_0 generated in this wavelength range. In contrast, the visible PIA appears within the instrument limit at 750 nm and can be fit with a single-exponential decay with a lifetime of 0.9 ps (a longer timescale is not necessary, likely because regeneration of the D_0 state at this lower excitation energy results in a "cooler" vibrationally hot state that absorbs to the blue of this wavelength range). In all, this ultrafast signal induction in the visible following 400-nm excitation combined with the loss of vibronic structure observed following direct D_1 excitation at 750 nm and the comparable ESA decay observed at both wavelengths support that D_2 to D_1 IC occurs on an ultrafast timescale for $F_4TCNQ^{\cdot -}$ in a CTC in DCE solution.

Transient absorption measurements were also conducted for $F_4TCNQ^{\cdot -}$:DPA^+ CTCs in which the donor lacks solubilizing methyl groups. Similar deactivation of the D_1 and D_2 state are observed; Figure A2.10-A2.11 presents transient absorption spectra of $F_4TCNQ^{\cdot -}$:DPA^+ at 750 nm excitation (we have not reported spectra for 400 nm excitation due a greater amount of neutral F_4TCNQ present, likely a result of differences in solubility between the electron donors). A 0.8

ps lifetime for internal conversion was observed, followed by vibrational cooling on a 6.3 ps timescale. The similarities in internal conversion timescales reveals that changing the donor does not influence anion dynamics appreciably in ICT CTCs. Differences in vibrational cooling lifetimes could be associated with differences in charge-pair interactions impacting accepting modes of the local solution environment responsible for vibrational energy dissipation: i.e., the lack of solubilizing methyl groups on this donor could possibly result in tighter ion-pair interactions for the resultant CTC, facilitating more the rapid vibrational energy transfer observed for the photoexcited anion.

In total, the excitation-dependent mechanisms for relaxation are independent of the donor molecule but differs considerably from relaxation dynamics observed for $F_4TCNQ^{\cdot -}$ in the gas phase: In the gas-phase, very rapid internal conversion proceeds directly to the ground state from both optically accessible excited states; for solution-phase CTCs the excited-state lifetimes are dilated, particularly in D_1, and relaxation of the D_2 state occurs via a cascade through lower levels. These differences therefore indicate that the relaxation dynamics of $F_4TCNQ^{\cdot -}$ are affected either by solvent-induced modification of electronic state couplings or by a caging effect of the solvent that inhibits the nonradiative deactivation pathway. Such solvent-induced effects are well-known to be possible for relaxation phenomena involving conical intersections.[56] In contrast, the presence of the counter-ion does not appear to have a significant impact on electronic deactivation: A comparison of CVs collected with CTCs vs. isolated donor and acceptor in DCE solution (Figure A2.12) suggests that the donor cation and acceptor anion likely have unscreened interactions consistent with a bound (possibly tightly bound) ion pair. Nonetheless, identical relaxation behavior is observed for the anion generated in CTCs and by electrochemical generation of pure donor solutions.

We note that the excited-state deactivation of $F_4TCNQ^{\cdot-}$ in condensed phase is similar to that of other radical anions that have been chemically, electrochemically, or photochemically prepared,[57] including aromatic imide and diimides[58] as well as fullerenes (C_{60} and C_{70}).[59-60] In all cases excited-state relaxation is characterized by rapid internal conversion to a vibrationally hot ground electronic state. The rapid deactivation of excited anions, compared to their neutral parent molecules, is correlated with smaller energy gaps between D_0 and D_1 states.[58, 61]

Table 4.2: Computed free energies for electron transfer in dichloroethane and toluene.

Redox Couple$_{(solvent)}$	ΔG (kcal/mol)
MPDA+/MPDA$_{(dce)}$	-104.96
MPDA+/MPDA$_{(tol)}$	-113.99
$F_4TCNQ/ F_4TCNQ^{\cdot-}{}_{(dce)}$	-117.98
$F_4TCNQ/ F_4TCNQ^{\cdot-}{}_{(tol)}$	-109.94

4.4.3 Properties and dynamics of charge-transfer complexes in low-dielectric films·

Based on our observations above, we postulated that lowering the dielectric strength of the surrounding chemical environment might alter the photoinduced dynamics of CTCs, resulting in behaviors more similar to what has been observed for $F_4TCNQ^{\cdot-}$ in the gas phase. Alternatively, a low dielectric environment might generate donor-acceptor complexes with only partial charge-transfer character. To explore this we first attempted to generate CTCs in toluene solutions, but found no new absorption features in UV-Vis spectra attributable to a donor-acceptor charge-transfer complex. This observation is consistent with DFT computations that reveal that the relative magnitude of the free energies changes for the $MPDA^+$/MPDA and $F_4TCNQ/F_4TCNQ^{\cdot-}$ reductions (and therefore ΔG for donor to acceptor charge transfer) reverses between DCE and toluene solvents, and therefore a spontaneous donor-to-acceptor charge-transfer reaction is not favorable in toluene. Computed free-energy changes for each redox reaction in DCE and toluene

are reported in Table 4.2. This reversal in spontaneity with solvent environment indicates that solvation energy (and particularly that of $F_4TCNQ^{\cdot-}$) is a critical contributor to supporting an ICT state with MPDA in solution.

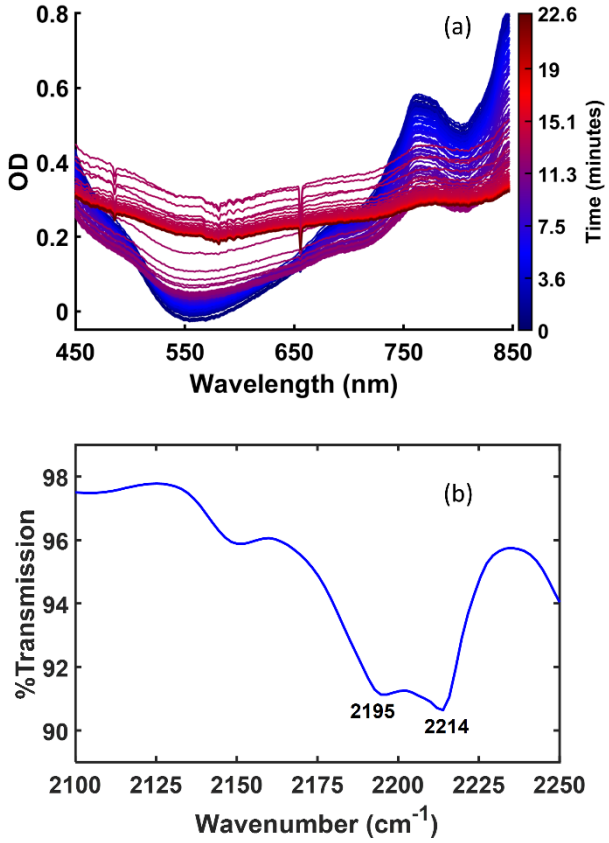

Figure 4.5. Steady-state spectroscopic characterization of dropcast films of $F_4TCNQ^{\cdot-}$:$MPDA^+$ doped PS. (a) UV-Vis spectra measured in time over the course of film drying; (b) F_4TCNQ CN stretching region of FTIR spectrum for film drop-cast onto NaCl salt plate.

To characterize interactions and properties of a PCT complex made with these compounds, we therefore prepared CTC-doped PS, whereby complexes that were initially ICT in character were trapped within a low-dielectric film as it dried after drop-casting from a DCE solution containing both CTCs and PS. Figure 4.5 shows a time-dependent progression of a UV-Vis spectra collected for a CTC-doped PS film as it dried; spectra were collected in 5 second intervals over the first 20 minutes of drying and on longer intervals for hours after drop-casting. Notably, the

sharp vibronic features associated with the anion absorption in the near IR become much less noticeable as the film dries, ultimately resulting in a broad, largely featureless absorption in this region after 1-2 hours of drying. Additionally, a two-fold decrease in optical density is observed in this region.

Based on these spectral changes and similarities with broad, featureless absorption of F_4TCNQ doped films of rra-P3HT,[38] we expect that CTCs exist predominantly as partial charge transfer complexes. Theoretical investigations of CTCs between F_4TCNQ and thiophene based oligomers of varying ionization potentials (IP) show linearity in degree of CT vs IP-|EA| for optimized geometries of donor and acceptor in the CTC.[62] The reversal in computed free-energy for charge transfer would therefore substantiate the favorability for PCT states in our CTC doped PS film.

To further explore that nature of charge-pair interaction in PS matrices, we collected FTIR spectra of CTC-doped PS films. FTIR has been shown to be useful for characterizing degree of charge transfer in F_4TCNQ-based CT salts.[14, 18, 39, 63] In particular, it has been established that the ν(C≡N) stretching modes are sensitive to local electron density: as electron density in the acceptor's lowest unoccupied molecular orbital (LUMO) increases the b_{1u} mode shifts towards lower frequencies. This frequency shift has been proposed to be correlated to the degree of charge transfer according to the following relationship:

$$\delta = \frac{2\Delta\nu}{\nu_0}\left(1 - \frac{\nu_1^2}{\nu_0^2}\right)^{-1} \qquad (4.2)$$

where ν_0 and ν_1 are the frequencies for neutral F_4TCNQ and $F_4TCNQ^{\cdot-}$ in an ICT with values of 2227 cm^{-1} and 2194 cm^{-1}, respectively.[39, 63] A detailed FTIR characterization of F_4TCNQ and F_4TCNQ^{-} has been reported by Meneghetti et al.,[39] as well as assignments of features for F_4TCNQ

doped P3HT (as previously discussed containing ICT and PCT states) for features within this same window.[38] Figure 4.5(b) shows the C≡N stretching region of an FTIR spectra of a CTC-doped PS film, with peaks at 2195 cm^{-1} and 2214 cm^{-1}; the former agrees with CN stretches of ICT pairs, whereas the latter reflects that PCT states are present. This data suggests the presence of both ICT and PCT states within our CTC-doped PS films; based on Equation 4.2, a PCT state with $\delta = 0.6$ charge separation is formed with solvent evaporation from the PS matrix.

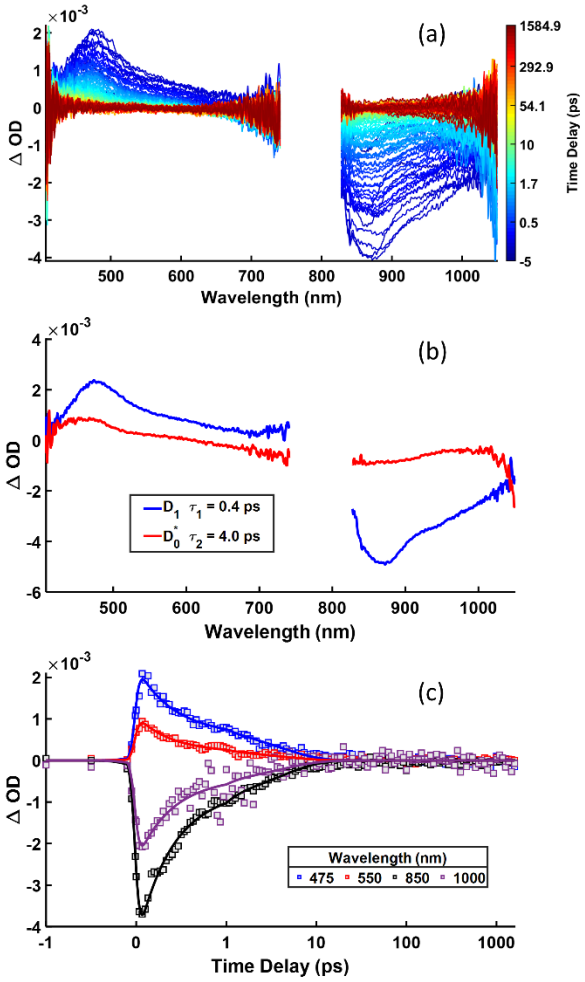

Figure 4.6. Transient absorption spectroscopy of $F_4TCNQ^{\cdot-}$:$MPDA^+$ doped PS excited at 750 nm. (a) Transient absorption spectra, (b) species associated spectra, and (c) selected fits to kinetic traces from global analysis.

PCT character could also be expected to alter the photophysics of the dopant, and it is therefore of interest to examine these with time-resolved spectroscopy. Transient absorption spectra collected with 750 nm excitation of PS films are presented in Figure 4.6(a). These spectra are again characterized by GSB and photoinduced absorption features similar to what are observed in measurements with CTC solutions. However, transient features are broadened with loss of vibronic structure throughout the visible and NIR, which may be expected in films containing PCT states (much as is seen in steady-state absorption features, Figure 4.5(a)). Given the qualitative similarities between Figure 4.6(a) and Figures 4.2(a,b) and 4.3(a,b), we posit that very similar photorelaxation processes occur in these films and have applied the kinetic scheme in Equation 4.1 to globally fit the spectral dynamics. Component spectra and selected fits to kinetic traces from global analysis are shown in Figure 4.6(b) and (c). From these fits, lifetimes of 0.4 ps and 4.0 ps were determined for internal conversion and vibrational cooling respectively.

By incorporating CTCs into a low dielectric polymer matrix the nature of the charge-pair interaction changes. We therefore cannot make direct connections to the photophysical properties of $F_4TCNQ^{\cdot -}$ in gas phase or examine the sensitivity of the photoresponses of the isolated acceptor anion to changes in local environment, as these are intimately connected with the charge-transfer character of these species. Nonetheless, transient spectra share similar spectral properties to solution phase, with dynamics in films appearing still to be controlled largely by the electronic properties of the anion. These results are relevant to doped organic semiconductor materials (i.e. P3HT and other materials) as we expect similar photoresponse of the dopant, whether part of an ICT or PCT complex. Notably, the relatively strong visible to near-IR absorption of F_4TCNQ-based CTCs (ICT and PCT) coupled with their rapid deactivation implies that these represent photon losses for light-driven applications with doped materials.

4.5 Conclusions

In summary we have characterized the electrochemistry, spectroscopy, and photoresponses of F_4TCNQ-based charge-transfer complexes in solution and low-dielectric film matrices. Solution phase samples exhibit integer charge transfer (full charge separation) and excitation-dependent photoresponses have been characterized to involve ultrafast internal conversion (~ 0.8 ps) followed by vibrational cooling which has lifetimes dependent on the wavelength of excitation (~ 9.4 ps and 12.1 ps). These relaxation timescales are slow relative to relaxation of $F_4TCNQ^{\cdot-}$ in gas phase, suggesting a solvent-induced modification of the shape of or dynamics on the potential energy landscape of the D_1 surface that permits rapid passage through a conical intersection in the gas phase. Furthermore, valence excitation to the D_2 state is observed to proceed through internal conversion to D_1 before fully returning to the ground state, unlike what is observed in gas-phase. When incorporating these complexes in a low dielectric polymer matrix the nature of the charge pair interaction changes. With the presence of PCT states (δ=60%), transient signals suggest that CTC photoresponses are still strongly dictated by properties of the anion and involve very rapid deactivation through a similar mechanism. Collectively these results are of fundamental interest to further understanding the photoresponses of quinone anions in condensed-phase media and, more specifically, the photoresponses of F_4TCNQ-doped organic semiconducting materials.

Supporting Information

Cyclic voltammetry, spectroelectrochemistry and additional transient absorption data and analysis for CTCs, neutral F_4TCNQ, and electrochemically generated $MPDA^+$ and $F_4TCNQ^{\cdot-}$. This material is provided in Appendix 2.

Acknowledgements

This work was supported by the U.S. Department of Energy, Office of Science, Basic Energy Sciences, under Award # DE-FG02-07ER46465.

4.6 References

1. Lüssem, B.; Keum, C.-M.; Kasemann, D.; Naab, B.; Bao, Z.; Leo, K., Doped Organic Transistors. *Chem. Rev.* **2016,** *116*, 13714-13751.

2. Lüssem, B.; Tietze, M. L.; Kleemann, H.; Hossbach, C.; Bartha, J. W.; Zakhidov, A.; Leo, K., Doped Organic Transistors Operating in the Inversion and Depletion Regime. *Nat. Commun.* **2013,** *4*, 6.

3. Walzer, K.; Maennig, B.; Pfeiffer, M.; Leo, K., Highly Efficient Organic Devices Based on Electrically Doped Transport Layers. *Chem. Rev.* **2007,** *107*, 1233-1271.

4. Zhou, X.; Blochwitz, J.; Pfeiffer, M.; Nollau, A.; Fritz, T.; Leo, K., Enhanced Hole Injection into Amorphous Hole-Transport Layers of Organic Light-Emitting Diodes Using Controlled P-Type Doping. *Adv. Funct. Mater.* **2001,** *11*, 310-314.

5. Jacobs, I. E.; Moule, A. J., Controlling Molecular Doping in Organic Semiconductors. *Adv. Mater.* **2017,** *29*, 1703063.

6. Kiefer, D.; Kroon, R.; Hofmann, A. I.; Sun, H.; Liu, X.; Giovannitti, A.; Stegerer, D.; Cano, A.; Hynynen, J.; Yu, L., et al., Double Doping of Conjugated Polymers with Monomer Molecular Dopants. *Nat. Mater.* **2019,** *18*, 149-155.

7. Skurski, P.; Gutowski, M., Excited Electronic States of the Anion of 7,7,8,8-Tetracyanoquinodimethane (TCNQ). *Theochem-J. Mol. Struct.* **2000,** *531*, 339-348.

8. Marchal, N.; Van Gompel, W.; Gélvez-Rueda, M. C.; Vandewal, K.; Van Hecke, K.; Boyen, H.-G.; Conings, B.; Herckens, R.; Maheshwari, S.; Lutsen, L., et al., Lead-Halide Perovskites Meet Donor–Acceptor Charge-Transfer Complexes. *Chem. Mater.* **2019,** *31*, 6880-6888.

9. Salzillo, T.; Campos, A.; Mas-Torrent, M., Solution-Processed Thin Films of a Charge Transfer Complex for Ambipolar Field-Effect Transistors. *J. Mater. Chem. C* **2019,** *7*, 10257-10263.

10. Talin, A. A.; Centrone, A.; Ford, A. C.; Foster, M. E.; Stavila, V.; Haney, P.; Kinney, R. A.; Szalai, V.; El Gabaly, F.; Yoon, H. P., et al., Tunable Electrical Conductivity in Metal-Organic Framework Thin-Film Devices. *Science* **2014,** *343*, 66-69.

11. Ferraris, J.; Cowan, D. O.; Walatka, V.; Perlstein, J. H., Electron Transfer in a New Highly Conducting Donor-Acceptor Complex. *J. Am. Chem. Soc.* **1973,** *95*, 948-949.

12. Melby, L. R.; Harder, R. J.; Hertler, W. R.; Mahler, W.; Benson, R. E.; Mochel, W. E., Substituted Quinodimethans. II. Anion-Radical Derivatives and Complexes of 7,7,8,8-Tetracyanoquinodimethan. *J. Am. Chem. Soc.* **1962,** *84*, 3374-3387.

13. Torrance, J. B., Difference between Metallic and Insulating Salts of Tetracyanoquinodimethane (TCNQ) - How to Design an Organic Metal. *Acc. Chem. Res.* **1979,** *12*, 79-86.

14. Mendez, H.; Heimel, G.; Winkler, S.; Frisch, J.; Opitz, A.; Sauer, K.; Wegner, B.; Oehzelt, M.; Rothel, C.; Duhm, S., et al., Charge-Transfer Crystallites as Molecular Electrical Dopants. *Nat. Commun.* **2015,** *6*, 8560.

15. Liang, Y. Y.; Qin, Y. K.; Chen, J.; Xing, W. L.; Zou, Y.; Sun, Y. M.; Xu, W.; Zhu, D. B., Band Engineering and Majority Carrier Switching in Isostructural Donor-Acceptor Complexes DPTTA-F_XTCNQ Crystals (X=1, 2, 4). *Adv. Sci.*, 9.

16. Qin, Y.; Cheng, C.; Geng, H.; Wang, C.; Hu, W.; Xu, W.; Shuai, Z.; Zhu, D., Efficient Ambipolar Transport Properties in Alternate Stacking Donor–Acceptor Complexes: From Experiment to Theory. *Phys. Chem. Chem. Phys.* **2016,** *18*, 14094-14103.

17. Jiang, H.; Hu, P.; Ye, J.; Zhang, K. K. K.; Long, Y.; Hu, W. P.; Kloc, C., Tuning of the Degree of Charge Transfer and the Electronic Properties in Organic Binary Compounds by Crystal Engineering: A Perspective. *J. Mater. Chem. C* **2018,** *6*, 1884-1902.

18. Jacobs, I. E.; Cendra, C.; Harrelson, T. F.; Bedolla Valdez, Z. I.; Faller, R.; Salleo, A.; Moulé, A. J., Polymorphism Controls the Degree of Charge Transfer in a Molecularly Doped Semiconducting Polymer. *Mater. Horiz.* **2018,** *5*, 655-660.

19. Valencia, A. M.; Cocchi, C., Electronic and Optical Properties of Oligothiophene-F_4TCNQ Charge-Transfer Complexes: The Role of the Donor Conjugation Length. *J. Phys. Chem. C* **2019,** *123*, 9617-9623.

20. Salzmann, I.; Heimel, G.; Oehzelt, M.; Winkler, S.; Koch, N., Molecular Electrical Doping of Organic Semiconductors: Fundamental Mechanisms and Emerging Dopant Design Rules. *Acc. Chem. Res.* **2016,** *49*, 370-8.

21. Tietze, M. L.; Benduhn, J.; Pahner, P.; Nell, B.; Schwarze, M.; Kleemann, H.; Krammer, M.; Zojer, K.; Vandewal, K.; Leo, K., Elementary Steps in Electrical Doping of Organic Semiconductors. *Nat. Commun.* **2018,** *9*, 1182.

22. Scholes, D. T.; Hawks, S. A.; Yee, P. Y.; Wu, H.; Lindemuth, J. R.; Tolbert, S. H.; Schwartz, B. J., Overcoming Film Quality Issues for Conjugated Polymers Doped with F_4TCNQ by Solution Sequential Processing: Hall Effect, Structural, and Optical Measurements. *J. Phys. Chem. Lett.* **2015,** *6*, 4786-4793.

23. Li, J.; Zhang, G.; Holm, D. M.; Jacobs, I. E.; Yin, B.; Stroeve, P.; Mascal, M.; Moulé, A. J., Introducing Solubility Control for Improved Organic P-Type Dopants. *Chem. Mater.* **2015,** *27*, 5765-5774.

24. Hasegawa, T.; Kagoshima, S.; Mochida, T.; Sugiura, S.; Iwasa, Y., Electronic States and Anti-Ferromagnetic Order in Mixed-Stack Charge-Transfer Compound (BEDT-TTF)(F_2TCNQ). *Solid State Commun.* **1997,** *103*, 489-493.

25. Vermeulen, D.; Zhu, L. Y.; Goetz, K. P.; Hu, P.; Jiang, H.; Day, C. S.; Jurchescu, O. D.; Coropceanu, V.; Kloc, C.; McNeil, L. E., Charge Transport Properties of Perylene–TCNQ Crystals: The Effect of Stoichiometry. *J. Phys. Chem. C* **2014,** *118*, 24688-24696.

26. Tsutsumi, J. y.; Matsuoka, S.; Inoue, S.; Minemawari, H.; Yamada, T.; Hasegawa, T., N-Type Field-Effect Transistors Based on Layered Crystalline Donor–Acceptor Semiconductors with Dialkylated Benzothienobenzothiophenes as Electron Donors. *J. Mater. Chem. C* **2015,** *3*, 1976-1981.

27. Bryce, M. R.; Murphy, L. C., Organic Metals. *Nature* **1984,** *309*, 119-126.

28. Murata, T.; Morita, Y.; Yakiyama, Y.; Fukui, K.; Yamochi, H.; Saito, G.; Nakasuji, K., Hydrogen-Bond Interaction in Organic Conductors: Redox Activation, Molecular Recognition, Structural Regulation, and Proton Transfer in Donor−Acceptor Charge-Transfer Complexes of TTF-Imidazole. *J. Am. Chem. Soc.* **2007,** *129*, 10837-10846.

29. Williams, J. M.; Beno, M. A.; Wang, H. H.; Leung, P. C. W.; Emge, T. J.; Geiser, U.; Carlson, K. D., Organic Superconductors: Structural Aspects and Design of New Materials. *Acc. Chem. Res.* **1985,** *18*, 261-267.

30. Hebard, A. F.; Rosseinsky, M. J.; Haddon, R. C.; Murphy, D. W.; Glarum, S. H.; Palstra, T. T. M.; Ramirez, A. P.; Kortan, A. R., Superconductivity at 18 K in Potassium-Doped C60. *Nature* **1991,** *350*, 600-601.

31. Fuzell, J.; Jacobs, I. E.; Ackling, S.; Harrelson, T. F.; Huang, D. M.; Larsen, D.; Moule, A. J., Optical Dedoping Mechanism for P3HT:F_4TCNQ Mixtures. *J. Phys. Chem. Lett.* **2016,** *7*, 4297-4303.

32. Voss, M. G.; Scholes, D. T.; Challa, J. R.; Schwartz, B. J., Ultrafast Transient Absorption Spectroscopy of Doped P3HT Films: Distinguishing Free and Trapped Polarons. *Faraday Discuss.* **2019,** *216*, 339-362.

33. Watts, K. E.; Neelamraju, B.; Ratcliff, E. L.; Pemberton, J. E., Stability of Charge Transfer States in F_4TCNQ-Doped P3HT. *Chem. Mater.* **2019,** *31*, 6986-6994.

34. Ghosh, R.; Chew, A. R.; Onorato, J.; Pakhnyuk, V.; Luscombe, C. K.; Salleo, A.; Spano, F. C., Spectral Signatures and Spatial Coherence of Bound and Unbound Polarons in P3HT Films: Theory Versus Experiment. *J. Phys. Chem. C* **2018,** *122*, 18048-18060.

35. Yee, P. Y.; Scholes, D. T.; Schwartz, B. J.; Tolbert, S. H., Dopant-Induced Ordering of Amorphous Regions in Regiorandom P3HT. *J. Phys. Chem. Lett.* **2019,** *10*, 4929-4934.

36. Scholes, D. T.; Yee, P. Y.; McKeown, G. R.; Li, S.; Kang, H.; Lindemuth, J. R.; Xia, X.; King, S. C.; Seferos, D. S.; Tolbert, S. H., et al., Designing Conjugated Polymers for Molecular Doping: The Roles of Crystallinity, Swelling, and Conductivity in Sequentially-Doped Selenophene-Based Copolymers. *Chem. Mater.* **2019,** *31*, 73-82.

37. Aubry, T. J.; Axtell, J. C.; Basile, V. M.; Winchell, K. J.; Lindemuth, J. R.; Porter, T. M.; Liu, J.-Y.; Alexandrova, A. N.; Kubiak, C. P.; Tolbert, S. H., et al., Dodecaborane-Based Dopants Designed to Shield Anion Electrostatics Lead to Increased Carrier Mobility in Doped Conjugated Polymer. *Adv. Mater.* **2020,** *31*, 1805647.

38. Neelamraju, B.; Watts, K. E.; Pemberton, J. E.; Ratcliff, E. L., Correlation of Coexistent Charge Transfer States in F_4TCNQ-Doped P3HT with Microstructure. *J. Phys. Chem. Lett.* **2018,** *9*, 6871-6877.

39. Meneghetti, M.; Pecile, C., Charge–Transfer Organic Crystals: Molecular Vibrations and Spectroscopic Effects of Electron–Molecular Vibration Coupling of the Strong Electron Acceptor $TCNQF_4$. *J. Chem. Phys.* **1986,** *84*, 4149-4162.

40. Sutton, A. L.; Abrahams, B. F.; D'Alessandro, D. M.; Elliott, R. W.; Hudson, T. A.; Robson, R.; Usov, P. M., Structural and Optical Investigations of Charge Transfer Complexes Involving the F_4TCNQ Dianion. *CrystEngComm* **2014,** *16*, 5234-5243.

41. Horke, D. A.; Roberts, G. M.; Verlet, J. R., Excited States in Electron-Transfer Reaction Products: Ultrafast Relaxation Dynamics of an Isolated Acceptor Radical Anion. *J. Phys. Chem. A* **2011,** *115*, 8369-74.

42. Panja, S.; Kadhane, U.; Andersen, J. U.; Holm, A. I. S.; Hvelplund, P.; Kirketerp, M. B. S.; Nielsen, S. B.; Stochkel, K.; Compton, R. N.; Forster, J. S., et al., Dianions of 7,7,8,8-Tetracyano-P-Quinodimethane and Perfluorinated Tetracyanoquinodimethane: Information on Excited States from Lifetime Measurements in an Electrostatic Storage Ring and Optical Absorption Spectroscopy. *J. Chem. Phys.* **2007,** *127*, 6.

43. Ma, L.; Hu, P.; Jiang, H.; Kloc, C.; Sun, H.; Soci, C.; Voityuk, A. A.; Michel-Beyerle, M. E.; Gurzadyan, G. G., Single Photon Triggered Dianion Formation in TCNQ and F_4TCNQ Crystals. *Sci. Rep.* **2016,** *6*, 28510.

44. Yamashita, Y.; Tsurumi, J.; Ohno, M.; Fujimoto, R.; Kumagai, S.; Kurosawa, T.; Okamoto, T.; Takeya, J.; Watanabe, S., Efficient Molecular Doping of Polymeric Semiconductors Driven by Anion Exchange. *Nature* **2019,** *572*, 634-638.

45. Sobczyk, M.; Skurski, P.; Simons, J., Bound-Excited Electronic States of the Anion of 2,3,5,6-Tetrafluoro-7,7,8,8-Tetracyanoquinodimethane. *J. Phys. Chem. A* **2003,** *107*, 7084-7091.

46. Roberts, G. M.; Lecointre, J.; Horke, D. A.; Verlet, J. R., Spectroscopy and Dynamics of the 7,7,8,8-Tetracyanoquinodimethane Radical Anion. *Phys. Chem. Chem. Phys.* **2010,** *12*, 6226-32.

47. Horke, D. A.; Li, Q.; Blancafort, L.; Verlet, J. R., Ultrafast above-Threshold Dynamics of the Radical Anion of a Prototypical Quinone Electron-Acceptor. *Nat. Chem.* **2013,** *5*, 711-7.

48. Ma, L.; Hu, P.; Kloc, C.; Sun, H.; Michel-Beyerle, M. E.; Gurzadyan, G. G., Ultrafast Spectroscopic Characterization of 7,7,8,8-Tetracyanoquinodimethane (TCNQ) and Its Radical Anion (TCNQ−). *Chem. Phys. Lett.* **2014,** *609*, 11-14.

49. Ekström, U.; Visscher, L.; Bast, R.; Thorvaldsen, A. J.; Ruud, K., Arbitrary-Order Density Functional Response Theory from Automatic Differentiation. *J. Chem. Theory Comput.* **2010,** *6*, 1971-1980.

50. Neese, F., Software Update: The Orca Program System, Version 4.0. *WIREs Comput. Mol. Sci.* **2018,** *8*, e1327.

51. Weigend, F.; Ahlrichs, R., Balanced Basis Sets of Split Valence, Triple Zeta Valence and Quadruple Zeta Valence Quality for H to Rn: Design and Assessment of Accuracy. *Phys. Chem. Chem. Phys.* **2005,** *7*, 3297-3305.

52. Schäfer, A.; Horn, H.; Ahlrichs, R., Fully Optimized Contracted Gaussian Basis Sets for Atoms Li to Kr. *J. Chem. Phys.* **1992,** *97*, 2571-2577.

53. Weigend, F., Accurate Coulomb-Fitting Basis Sets for H to Rn. *Phys. Chem. Chem. Phys.* **2006,** *8*, 1057-1065.

54. Molloy, M. S.; Snyder, J. A.; Bragg, A. E., Structural and Solvent Control of Nonadiabatic Photochemical Bond Formation: Photocyclization of O-Terphenyl in Solution. *J. Phys. Chem. A* **2014,** *118*, 3913-3925.

55. Yu, W. J.; Magnanelli, T. J.; Zhou, J. W.; Bragg, A. E., Structural Heterogeneity in the Localized Excited States of Poly(3-Hexylthiophene). *J. Phys. Chem. B* **2016,** *120*, 5093-5102.

56. Kahan, A.; Wand, A.; Ruhman, S.; Zilberg, S.; Haas, Y., Solvent Tuning of a Conical Intersection: Direct Experimental Verification of a Theoretical Prediction. *J. Phys. Chem. A* **2011,** *115*, 10854-10861.

57. Fujitsuka, M.; Majima, T., Reaction Dynamics of Excited Radical Ions Revealed by Femtosecond Laser Flash Photolysis. *Photochem. Rev.* **2017,** *35*, 25-37.

58. Gosztola, D.; Niemczyk, M. P.; Svec, W.; Lukas, A. S.; Wasielewski, M. R., Excited Doublet States of Electrochemically Generated Aromatic Imide and Diimide Radical Anions. *J. Phys. Chem. A* **2000,** *104*, 6545-6551.

59. Fujitsuka, M.; Ohsaka, T.; Majima, T., Dual Electron Transfer Pathways from the Excited C60 Radical Anion: Enhanced Reactivites Due to the Photoexcitation of Reaction Intermediates. *Phys. Chem. Chem. Phys.* **2015,** *17*, 31030-31038.

60. Lu, C. L.; Fujitsuka, M.; Sugimoto, A.; Majima, T., Excited-State Properties of Radical Anions of C70 and Its Derivatives: Significant Differences from the Case of C60. *J. Phys. Chem. C* **2018,** *122*, 13385-13390.

61. Breslin, D. T.; Fox, M. A., Excited-State Behavior of Thermally Stable Radical Ions. *J. Phys. Chem.* **1994,** *98*, 408-411.

62. Zhu, L.; Kim, E.-G.; Yi, Y.; Brédas, J.-L., Charge Transfer in Molecular Complexes with 2,3,5,6-Tetrafluoro-7,7,8,8-Tetracyanoquinodimethane (F4-TCNQ): A Density Functional Theory Study. *Chem. Mater.* **2011,** *23*, 5149-5159.

63. Kampar, E.; Neilands, O., Degree of Charge Transfer in Donor–Acceptor Systems of the П–П Type. *Russ. Chem. Rev.* **1986,** *55*, 334-342.

Chapter 5

Intramolecular Photoinduced Charge Transfer and Recombination Dynamics in Vinyl-Arene Terminated Organosilanes

The contents of this chapter and its associated appendix are published in *J. Phys. Chem. B* 2021, 125, 30, 8460–8471

Brandon J. Barrett, Daniel Jimenez, Rebekka S. Klausen, and Arthur E. Bragg

5.1 Abstract

We report on charge-transfer dynamics of newly designed acceptor-donor-acceptor organosilanes, with a specific focus on how donor-acceptor combination and local chemical environment can be used to control the lifetime for intramolecular charge-separation between silane electron donors and organic acceptors. In this work linear oligosilanes were capped with arene-vinyl end groups of variable electron-accepting strength: weak (diester vinyl), intermediate (ester,cyano vinyl) and strong (dicyano vinyl). Ultrafast transient absorption spectroscopy was used to characterize their structure-dependent charge-transfer and recombination behaviors. All

structures exhibit similar photoinduced ultrafast spectral dynamics that we ascribe to relaxation of the nascent charge-separated excited state followed by a return to the ground state via charge recombination. We find that relaxation of the nascent "hot" charge-separated excited state scales with the strength of dipole-dipole interactions between solvent molecules and the polar arene-vinyl acceptor. Furthermore, electron-accepting strength governs whether electronic coupling dictates charge recombination rate: weak acceptors produce charge-separated states that exhibit relatively large electronic coupling for back-electron transfer (approaching the adiabatic limit) that result in fast recombination, whereas the strong and moderate-strength acceptors support more stable charge-separated states with weaker coupling and longer lifetimes. We find that recombination rates increase substantially for structures with weak and moderate-strength acceptors in cyclohexane (i.e. negligible solvent reorganization energy), which we attribute to an increased electronic coupling in a nonpolar solvent environment where charge pairs are weakly screened. In contrast, for structures with strong electron acceptors, the very low reorganization energy of cyclohexane places back-electron transfer even further into the Marcus inverted regime, with a resultant increase in charge-separation lifetime. Together these results provide critical insights on how to tune photoinduced charge-transfer behavior in organic-inorganic hybrids that have potential material applications in molecular- and opto-electronics.

5.2 Introduction

Molecular electronics based on π-conjugated organic small molecules and polymers continue to hold technological promise, with potential uses in organic field-effect transistors (OFETs)[1], organic light-emitting diodes (OLEDs)[2], organic photovoltaics (OPVs)[3], and nonlinear optical materials.[4] Interest in organic-based materials is predicated on their preparative and

economic benefits, including their relative stock abundance compared to inorganic counterparts, potential for a broad structural palette, material flexibility, and ease of material processing.[5] Research efforts in this area span fundamental synthetic design to materials processing to fundamental material and device/application characterization. Hybrid (organic-inorganic) materials present further potential for increasing the structural palette for molecular electronics in order to combine desirable physical properties of inorganic components with the beneficial properties of organics. Herein we describe our efforts to better understand structure-function relationships controlling charge-pair generation in hybrid organosilane materials with potential applications for molecular-based optoelectronics.

Oligosilanes are Si-containing compounds that possess at least one Si-Si bond, strongly absorb ultraviolet (UV) light, and exhibit σ-conjugation that is sensitive to the length and/or molecular conformation of the silane chain.[6] Broadly speaking, *organo*silanes combine organic sidechains and oligosilanes, where π-conjugated side chains in particular facilitate electronic interactions between organic and inorganic moieties.[7] As a result of this hybrid conjugation, organosilanes exhibit high conductivity on the molecular[8-10] and bulk scales.[11] Furthermore, these interactions have significant impacts on the spectroscopy, photophysics, and photochemistry of organosilanes.[12-13] Gilman et al. showed that the optical properties of a series of permethylated oligosilanes are significantly varied when the silane chain is terminated with π-conjugated organic groups.[7] Other studies have shown that permethylated oligosilanes can be induced with light to donate electrons to the electron acceptor tetracyanoethylene (TCNE),[14] suggesting that sigma-pi conjugated hybrid materials might be expected to exhibit photoinduced intramolecular charge-transfer. These discoveries prompted the design of new organosilane materials with silane-bridged

donor-acceptor units as a common architecture[15-21] and the interrogation of their photoinduced charge-transfer and nonlinear optical behaviors.

We recently reported a new class of cyano(ester)vinyl capped oligosilanes shown in Scheme 5.1a, their charge transport properties, and their photoinduced charge-transfer behaviors. Films of these hybrid materials exhibit much higher conductivities than films made only with their σ- or π-conjugated components.[22] Steady-state absorption and emission spectroscopy further revealed a spectroscopic feature attributable to a σ-π* charge-transfer transition that is observed for structures with covalently bound silane and ester-cyano-vinyl groups, but does not appear in spectra associated with σ- or π- conjugated components on their own.[23] Using femtosecond stimulated Raman spectroscopy (FSRS), we confirmed that photoexcitation of this optical transition results in intramolecular charge transfer from the electron-rich silane core (donor) to the electron-poor cyano(ester)vinyl (acceptor) unit, as the Raman spectrum of the excited organosilane agrees well with that of a reduced acceptor unit.[24] Furthermore, this work revealed that the degree of charge separation scales with silane chain length.

In subsequent work we characterized the photophysics and charge-transfer dynamics in a series of acceptor-donor-acceptor (ADA) and donor-acceptor (DA) organosilane structures in solutions of moderately polar solvents using transient absorption and fluorescence spectroscopy (**Si*n*s-E,C** and **Si*n*a-E,C** nomenclature is used to describe symmetric and asymmetric ester-cyano-vinyl structures, respectively, where ***n*** refers the number of silicon atoms in the chain).[23] We determined that both ADA and DA structures exhibit direct, optically-induced intramolecular charge transfer to generate charge-polarized excited states; in the case of ADA structures, asymmetric charge separation results from symmetry breaking associated with silane-chain conformation. Spectra of the charge-separated excited state were observed to evolve on two

timescales that we attributed to fast relaxation within the excited state (τ_1) followed by a slower deactivation to the ground state via charge recombination (τ_2). We found that the timescales for these processes are sensitive to silane chain length and solvent environment: Faster recombination rates were measured for longer silane chains and a gap-law behavior was observed when τ_2 was correlated against peak emission energy across a series of **Si*n*a-E,C** and **Si*n*s-E,C** structures. In contrast, τ_1 showed no dependence on chain length or symmetry (ADA vs. DA), but was observed to change dramatically with variation in solvent polarity (acetonitrile < dichloroethane < chloroform) indicating that τ_1 is principally associated with a solvent reorganization timescale that follows photoinduced charge separation. Notably, faster recombination rates (i.e. shorter τ_2) were also observed in more polar solvent environments (i.e. acetonitrile). Together, the dependence of τ_2 on S_1-S_0 energetic gap and solvent polarity pointed to charge recombination (back-electron transfer) occurring within the Marcus inverted region, which is common for photoinduced charge recombination processes.[25]

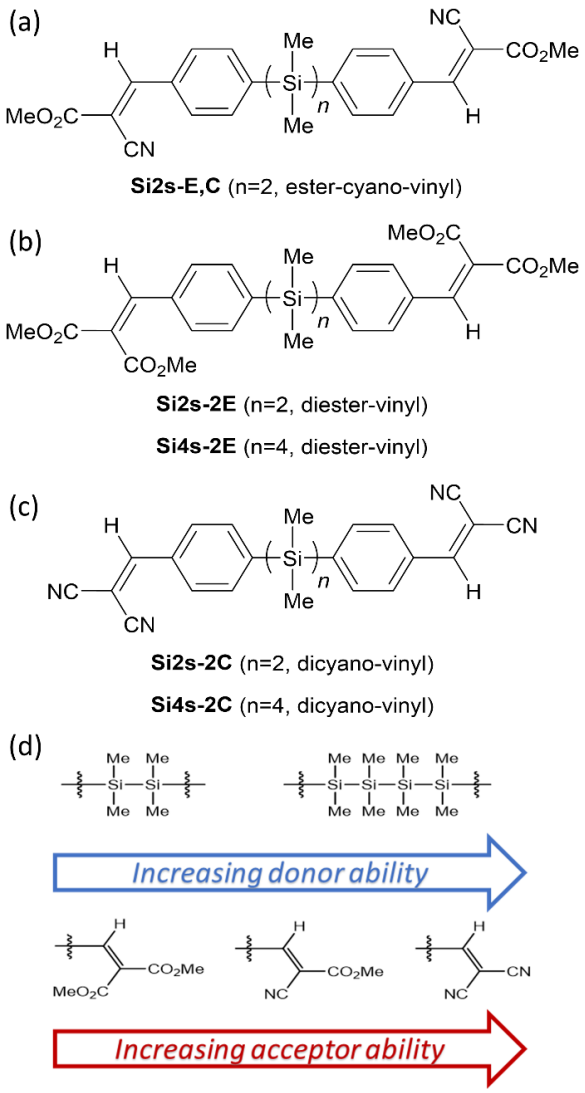

Scheme 5.1. Structures of symmetric (acceptor-donor-acceptor, ADA) organosilanes, **Si*n*s**, with various acceptor pendants. (a) ester, cyano-vinyl **Si*n*s-E,C**, (b) diester-vinyl **Si*n*s-2E**, (c) dicyano-vinyl **Si*n*s-2C**. (d) relative silicon chain electron donating and arene-vinyl electron accepting strengths.

An obvious question about these structures is how to control the lifetimes of their photoinduced charge-separated states, as this may be useful for manipulating nonlinear optical properties and uses in optoelectronic applications. To do so one must consider a few key parameters in the semi-classical rate expression for electron transfer derived by Marcus:

$$k_{ET} = \frac{1}{h\sqrt{4\pi k_B T \lambda}} |V|^2 exp\left(\frac{-(\Delta G^0 + \lambda)^2}{4\lambda k_B T}\right) \quad (5.1)$$

In Equation 5.1, ΔG^0 represents the free energy (driving force) between charge-separated (D^+/A^-) and charge-neutral (D/A) states, *V* corresponds to the electronic coupling strength between these two states, and λ is the reorganization energy (solvent and intramolecular) in response to electron transfer.[26] In the inverted regime, the driving force is larger than the reorganization energy ($-\Delta G^0 > \lambda$); consequently, increasing the driving force for electron transfer presents a handle for slowing down the back electron-transfer rate. In practice, for a donor-acceptor structure of interest, ΔG^0 is often controlled through additions or variations of electron withdrawing or donating substituents on acceptor, bridge, or donor units.[27-28] Alternatively, for a fixed ΔG^0, the local solvent polarity (i.e. reorganization energy) can also be selected to tune the rate of electron transfer (as we have previously observed for **Si6s-E,C**).[28-29] Notably, in special cases where ΔG^0 and λ are roughly the same order of magnitude, electron transfer can be tuned from the normal to the inverted regimes with variation in solvent reorganization energy.[30]

Another possibility for decreasing the recombination rate is to decrease the electronic coupling, *V*. It is known that electronic coupling strength can be tuned by varying bridge length or structure in donor-bridge-acceptor systems, or through use of a chemical tether for controlling molecular conformation to tune orbital overlaps.[31] In systems in which the donor and acceptor groups are directly linked, as in organosilanes, the donor and acceptor strengths and contributions from solvent stabilization of charge-polarized excited states are expected to impact electronic coupling and therefore recombination rates. These relationships must be consideration in order to design and fine-tune charge-transfer properties in molecular systems for material application.[32]

Here we present results of transient spectroscopic investigations of charge-transfer and recombination dynamics for the larger set of organosilanes presented in Scheme 5.1. With the aim

of controlling and possibly extending charge-separation lifetimes in this class of molecule, we address two previously unexplored questions: how are photoinduced charge-transfer and recombination behaviors impacted by (1) organic acceptor strength and (2) solvent polarity or reorganization energy? We present results with diester-vinyl (**Si*n*s-2E**) and dicyano-vinyl (**Si*n*s-2C**) (see Scheme 5.1b-c) terminated silanes and compare with our previous results obtained with **Si*n*s-E,C**, thereby spanning weak, intermediate, and strong electron accepting regimes. Furthermore, we investigate their charge-transfer and recombination behaviors in nonpolar environments (cyclohexane) that would be predicted to have lower reorganization energies and correspondingly slower recombination rates for electron transfer in the Marcus inverted regime.

5.3. Experimental

5.3.a. Materials and Methods.

All chemicals and solvents were purchased from Sigma-Aldrich, Acros Organics, or Tokyo Chemical Industry Co. and used without additional purification steps unless stated otherwise. The compounds 1,2-bis-(4-formylphenyl)tetramethyldisilane and 1,4-bis-(4-formylphenyl)octamethyltetrasilane were synthesized according to literature procedures.[22-24] All reactions were performed in oven-dried glassware. The flasks were fitted with rubber septa and reactions were conducted under a positive pressure of argon. Anhydrous anaerobic solvents were obtained from JC Meyer solvent purification system (Model: Phoenix 5 solvent freestanding double columns 24 x 24). All column chromatography was performed on a Teledyne ISCO Combiflash Rf using Redisep RF silica columns. ^{1}H NMR, ^{13}C NMR, and ^{29}Si NMR spectra were recorded on a Bruker Avance III 400 MHz Spectrometer. Spectra are reported in parts per million downfield from tetramethylsilane and are referenced to residual protium in the NMR solvent for

^{1}H NMR ($CHCl_3$: δ 7.26; C_6H_6: δ 7.16), carbon resonances of the solvent for ^{13}C NMR ($CDCl_3$: δ 77.0; C_6D_6: δ 128.5) and silicon resonance of tetramethylsilane (TMS) for ^{29}Si NMR (TMS: δ 0.0). Data are represented as follows: chemical shift, multiplicity (br = broad, s = singlet, d = doublet, t = triplet, q = quartet, m = multiplet), coupling constants in Hertz, and integration. High-resolution mass spectra were obtained at the Johns Hopkins University Mass Spectrometry Facility using a VG Instruments VG70S/E magnetic sector mass spectrometer with EI (70 eV).

5.3.b. Synthesis.

5.3.b.1. Si2s-2E. A 100 mL three-neck round bottom flask equipped with reflux condenser and stir bar was charged with 1,2-bis-(4-formylphenyl)tetramethyldisilane (250 mg, 0.760 mmol) and sealed with a rubber septum. The silane was dissolved in benzene (10.0 mL). The flask was charged with dimethyl malonate (183 µL, 2.10 equiv.) and piperidine (20.0 µL, 0.300 equiv.). The flask was heated at reflux for 22 hours. The flask was cooled to room temperature and volatiles were removed by rotary evaporation. **Si2s-2E** was isolated (215 mg, 51% yield) after column chromatography (20% ethyl acetate in hexanes). ^{1}H NMR (400 MHz, $CDCl_3$) δ 7.74 (s, 2H), 7.35 (m, 8H), 3.86 (d, 12H), 0.32 ppm (s, 12H). ^{29}Si NMR (400 MHz, $CDCl_3$) δ -21.10. HRMS (ASAP+): $C_{28}H_{34}O_8Si_2$ (M+H): 555.1870, found 555.1873.

5.3.b.2. Si4s-2E. A 100 mL three-neck round bottom flask equipped with reflux condenser and stir bar was charged with 1,4-bis-(4-formylphenyl)octamethyltetrasilane (150 mg, 0.339 mmol) and sealed with a rubber septum. The silane was dissolved in benzene (6.00 mL). The flask was charged with dimethyl malonate (94.0 mg, 2.10 equiv.) and piperidine (10.0 µL, 0.300 equiv.). The flask was heated at reflux for 20 hours. The flask was cooled to room temperature and volatiles

were removed by rotary evaporation. **Si4s-2E** was isolated (62 mg, 27% yield) after column chromatography (20% ethyl acetate in hexanes). ^{1}H NMR (400 MHz, $CDCl_3$): δ 7.75 ppm (s, 2H), 7.43 (d, 4H), 7.40 (d, 4H), 3.84 (s, 6H), 3.80 (s, 6H), 0.33 (s, 12H), 0.01 (s, 12H). ^{29}Si NMR (400 MHz, $CDCl_3$) δ -17.40, -44.10. HRMS (ASAP+): $C_{32}H_{46}O_8Si_4$ (M+H): 671.2348, found 671.2344.

5.3.b.3. Si2s-2C. A 100 mL three-neck round bottom flask equipped with reflux condenser and stir bar was charged with 1,2-bis-(4-formylphenyl)tetramethyldisilane (164 mg, 0.501 mmol) and sealed with a rubber septum. The silane was dissolved in benzene (6.60 mL). The flask was charged with malonitrile (69.5 mg, 2.1 equiv.) and piperidine (15.0 µL, 0.30 equiv.). The flask was heated at reflux for 24 hours. The flask was cooled to room temperature and volatiles were removed by rotary evaporation. **Si2s-2C** was isolated (97 mg, 45% yield) after column chromatography (15% ethyl acetate in hexanes). ^{1}H NMR (400 MHz, $CDCl_3$) δ 7.79 (d, 4H), 7.75 ppm (s, 2H), 7.48 ppm (d, 4H), 0.38 ppm (s, 12H). ^{29}Si NMR (400 MHz, $CDCl_3$) δ -19.94. HRMS (ASAP+): $C_{24}H_{22}N_4Si_2$ (M+H): 423.1461, found 423.1472.

5.3.b.4. Si4s-2C. A 100 mL three-neck round bottom flask equipped with reflux condenser and stir bar was charged with 1,4-bis-(4-formylphenyl)octamethyltetrasilane (150 mg, 0.339 mmol) and sealed with a rubber septum. The silane was dissolved in benzene (6.00 mL). The flask was charged with malonitrile (47.1 mg, 2.1 equiv.) and piperidine (10.0 µL, 0.30 equiv.). The flask was heated at reflux for 2.5 hours. The flask was cooled to room temperature and volatiles were removed by rotary evaporation. **Si4s-2C** was isolated (53.1 mg, 29% yield) after column chromatography (20% ethyl acetate in hexanes) and recrystallization in dichloromethane-hexanes. ^{1}H NMR (400 MHz, $CDCl_3$): δ 7.84 (d, 4H), 7.74 (s, 2H), 7.56 (d, 4H), 0.38 (s, 12H), 0.02 (s, 12H). ^{29}Si NMR (400 MHz, $CDCl_3$): δ -16.82, -43.97. HRMS (ASAP+): $C_{28}H_{34}N_4Si_4$ (M+H): 539.1938, found 539.1940.

5.3.c. Sample Preparation.

Cyclohexane (CH) and dichloromethane (DCM) were purchased from Fischer Scientific (99.9% and ≥ 99.8% assays respectively) and used as received. Organosilane solutions were prepared at concentrations of ~10^{-4} mol/L and sonicated until dissolved in solvent. UV-Vis spectra were collected with a diode array spectrometer that is fiber-optically coupled to tungsten and deuterium lamps (Stellarnet). Solution samples used in laser experiments were stirred in a 2 mm path length quartz cuvette, resulting in optical densities (OD) around 0.7 and 0.9 at the wavelength of excitation for diester/ester-cyano and dicyano oligosilanes, respectively. No photochemical changes were observed in UV-Vis spectra collected before and after irradiation over the course of transient absorption measurements.

5.3.d. Transient Absorption Spectroscopy.

The setup for our transient absorption measurements have been described in detail elsewhere,[33-34] and here we describe specific experimental details for the work presented. Ultrafast excitation and probe pulses were generated using the amplified output of a Ti:Sapphire laser (Coherent Legend Elite, 3.8 mJ/pulse, 1 kHz repetition rate, ~35 fs pulse duration). Excitation pulses at 360 nm were obtained through fourth harmonic generation of the NIR signal obtained from an optical parametric amplifier (OPA, Coherent OperaSolo). Broadband probe pulses were obtained via white light generation in a 2 mm sapphire crystal (425-750 nm). Probe pulses were passed through a wire-grid polarizer (Thorlabs) set at magic angle (54.7°) with respect to the pump pulse polarization and placed immediate before the sample in order to eliminate time-dependent polarization effects. The spot size of the probe pulse at the sample was roughly 100 μm, whereas

pump pulses were focused to a spot size of about 1 mm, with pump pulse energies at 2 μJ or less. The effective time resolution for measurements reported here was 200 fs (i.e. FWHM of pump-probe cross-correlation).

5.4. Results and Discussion

5.4.a. Donor and acceptor dependence of steady-state absorption features.

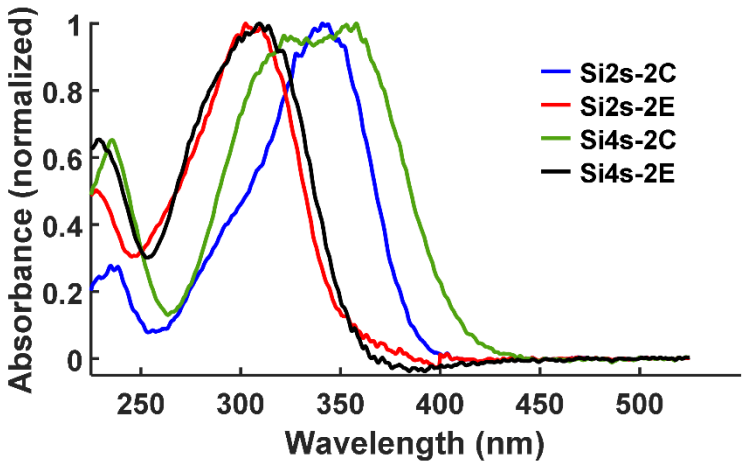

Figure 5.1. UV-Vis spectra of **Si2s-2C** (blue), **Si2s-2E** (red), **Si4s-2C** (green), and **Si4s-2E** (black) dissolved in DCM.

Figure 5.1 presents steady-state UV-Vis absorption spectra of **Si2s-2C** (blue), **Si2s-2E** (red), **Si4s-2C** (green), and **Si4s-2E** (black) in DCM. Spectra taken with these organosilanes exhibit similar features as observed previously for symmetric (ADA) and asymmetric (AD) ester,cyano-vinyl organosilanes (i.e. **Si*n*s-E,C** and **Si*n*a-E,C**). We have previously shown that the broad feature in the near-UV between 255 nm and 400 nm arises from overlapping π-π* and σ-π* transitions, where the latter is the optically induced intramolecular charge transfer transition that results from combining the silane donor and arene acceptor.[23] Figure 5.1 illustrates that the red-

edge of the absorption spectra, where the σ-π* transition lies, red-shifts with increased acceptor strength (i.e **2E** < **2C**). Spectra previously collected with **Si*n*s-E,C** also fits this qualitative trend: the wavelengths at half-rise intensities on the red edge of the σ-π* transition are approximately 334 nm, 360 nm, and 368 nm for **Si2s-2E**, **Si2s-E,C**, and **Si2s-2C**, respectively, and 337 nm, 375 nm, and 385 nm for **Si4s-2E**, **Si4s-E,C**, and **Si4s-2C**.[23] In contrast, the feature around 230 nm corresponds to a σ-σ* transition of the silane core. This feature's position is similar for both n = 2 and 4, which is consistent with our previous steady-state measurements with **Si*n*s-E,C** that only showed red-shifts in the σ-σ* transition for longer donor chain lengths (n>4) due to increased σ-conjugation. Given the overlap of various absorption transitions at shorter wavelengths, TAS studies described below used an excitation wavelength of 360 nm in order to selectively excite the σ-π* transition.

5.4.b. Donor and acceptor dependence of intramolecular charge-transfer dynamics probed by transient absorption spectroscopy

Figures 5.2(a-b) and 5.3(a-b) present transient absorption spectra obtained with **Si2s-2E** and **Si2s-2C**, respectively, dissolved in DCM with excitation at 360 nm. Figures 5.2(a) and 5.3(a) illustrate the appearance of transient spectral features and their initial evolution on short timescales (<3 ps) following photoexcitation, whereas Figures 5.2(b) and 5.3(b) highlight the decay of photoexcited species on longer timescales (up to ~1 ns). Figures 5.2(b) and 5.3(b) reveal that transient spectra of the photoexcited organosilanes are characterized by broad positive features peaking between 450 nm and 500 nm and negative features peaking around 625 nm and 650 nm, respectively. The positions of these features are highly similar to what we observed in transient absorption spectra collected with the **Si*n*s-E,C** compounds and which we assigned to excited-state

absorption (ESA) and stimulated emission (SE) transitions, respectively. These assignments were supported by the instantaneous appearance of the broad absorption (on the time scale of the pump-probe cross-correlation) and the fact that the negative feature falls within the wavelength range in which steady-state fluorescence has been observed[23-24] (see also Figures A3.3-A3.6).

Figures 5.2(a) and 5.3(a) reveal that the transient spectral shapes evolve in the first few picoseconds that follow photoexcitation, with the ESA band red-shifting/broadening and the SE band both red-shifting and gaining intensity. This spectral evolution is followed by complete disappearance of these features (i.e. returning to baseline) over tens to hundreds of picoseconds. As described above, we have previously attributed these distinct phases of spectral relaxation to solvent reorganization in response to the formation of a charge-separated state within a few picoseconds of initial excitation, followed by charge recombination back to the ground state on timescales of 10s-100s of ps; we confirmed the former using solvent-dependent TA measurements. Notably, comparison of Figure 5.2(a) and 5.3(a) reveals that the stimulated emission band appears instantaneously for **Si2s-2C** but exhibits a lag or induction for **Si2s-2E**; this indicates that solvent reorganization is likely to have a much more significant role in stabilizing (or possibly generating[35-36]) the charge-separated excited state for the structure with the weaker accepting group.

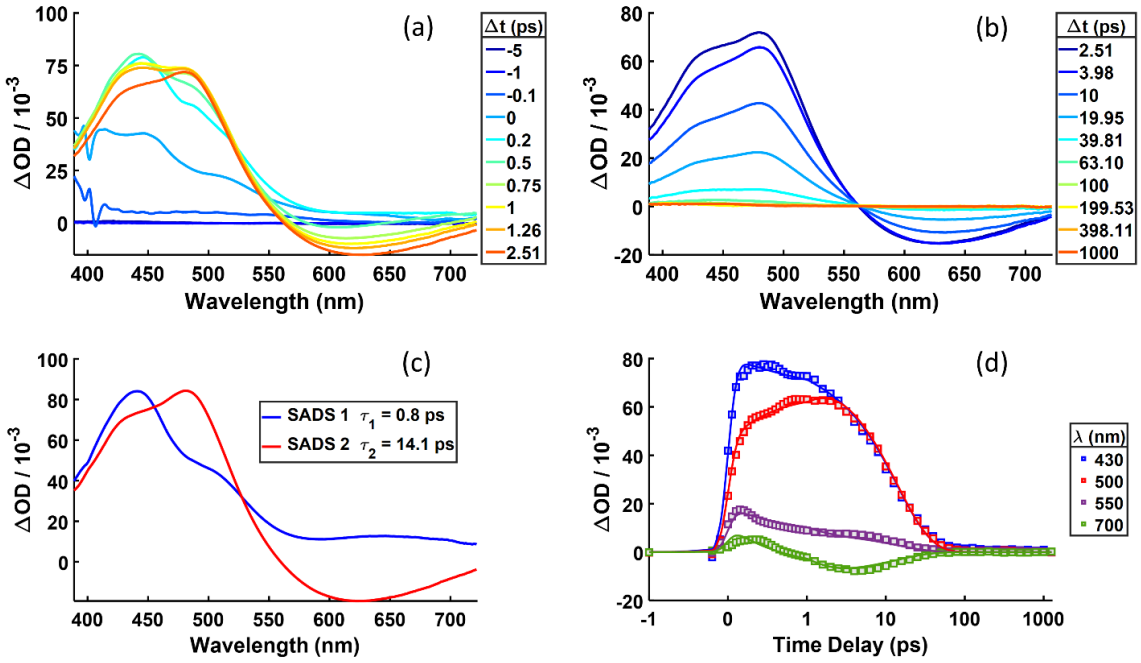

Figure 5.2. Transient absorption spectra of **Si2s-2E** dissolved in DCM excited at 360 nm (a) before and (b) after 3 ps. (c) species associated difference spectra and (d) temporal traces at selected wavelengths plotted with fits, obtained from global analysis with the kinetic model presented in Equation 5.2.

In order to quantify the timescales associated with these photoinduced processes we have applied the following two-state kinetic model for global fitting of transient spectral data:

$$S_1^* \xrightarrow{\tau_1} S_1 \xrightarrow{\tau_2} S_0 \qquad (5.2)$$

Here S_1^* corresponds with the "hot," photoprepared (charge-separated) excited state which relaxes through solvent/structural reorganization to a minimum-energy configuration S_1; the ground state S_0 is subsequently recovered by charge recombination on a longer timescale, τ_2. Figures 5.2(c) and 5.3(c) plot the species associated difference spectra (SADS, i.e. the transient spectral intensities associated with each kinetic state relative to the steady-state S_0 absorption spectrum) for S_1^* and S_1; fits to transient data at selected probe wavelengths are plotted in Figures 5.2(d) and 5.3(d). Based on the fits, S_1^* for **Si2s-2E** (**Si2s-2C**) relaxes to S_1 with a 0.8 ps (2.8 ps) lifetime,

which subsequently decays back to the ground state via charge recombination with a 14.1 ps (237.1 ps) lifetime. The excited-state relaxation (τ_1) and charge recombination lifetimes (τ_2) are listed alongside prior results obtained with **Si2s-E,C** in Table 5.1.

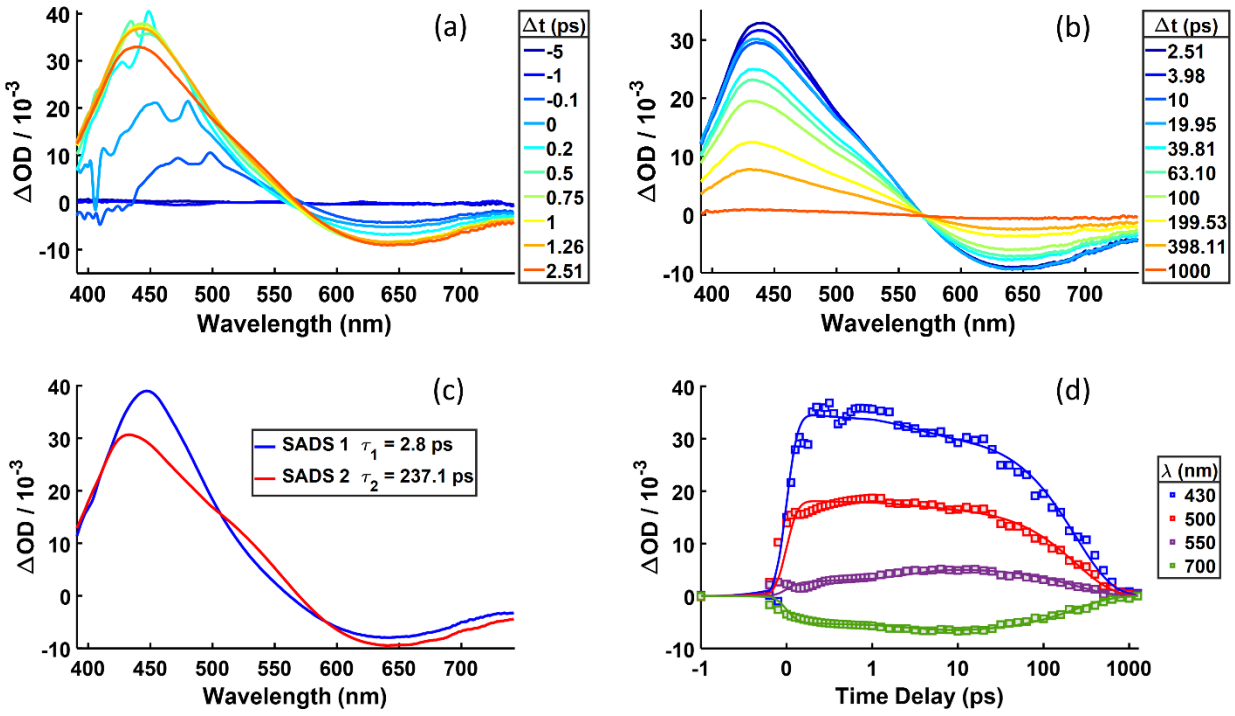

Figure 5.3. Transient absorption of **Si2s-2C** dissolved in DCM excited at 360 nm (a) before and (b) after 3 ps. (c) species associated difference spectra and (d) temporal traces at selected wavelengths plotted with fits, obtained from global analysis with the kinetic model presented in Equation 5.2.

Table 5.1. Excited-state relaxation (τ_1) and charge recombination (τ_2) lifetimes for **Si2s** and **Si4s** organosilanes dissolved in DCM under 360 nm excitation. Timescales were obtained from global fitting transient spectral data to the kinetic model summarized in Equation 5.2. [a] Values taken from ref 20.

Compound	τ_1 (ps)	τ_2 (ps)
Si2s-2E	0.8 ± 0.1	14.1± 0.6
Si2s-E,C [a]	1.1 ± 0.1	680 ± 30
Si2s-2C	2.8 ± 1.2	237 ± 19
Si4s-2E	0.8 ± 0.1	53 ± 3
Si4s-E,C [a]	1.6 ± 0.4	130 ± 30
Si4s-2C	8.7 ± 1.5	180 ± 10

Transient absorption measurements with **Si4s-2E** and **Si4s-2C** dissolved in DCM were also conducted to interrogate chain length (and therefore donor strength) dependence on charge recombination kinetics. This data alongside results of global fitting subject to Equation 5.2 are presented in Figures A3.1 and A3.2, respectively. Best-fit timescales are presented in Table 5.1 with prior results obtained with **Si4s-E,C**.

For both sets of compounds the excited-state relaxation lifetime (τ_1) increases with acceptor strength (e.g. **Si2s-2E** < **Si2s-E,C** < **Si2s-2C**). We attribute this variation with the impact of dipole-dipole interactions between solvent and polar cyano groups that exist prior to excitation and that are expected to impact the scale and therefore rate of solvent reorganization that follows photoinduced charge separation. With the exception of **Si2s-2C** and **Si4s-2C**, little variation in the solvent reorganization lifetime is observed for changes to donor chain length. We previously observed similar behavior for **Si*n*s-E,C** ***n***=2,4,6,8 organosilanes, which all exhibited solvent reorganization lifetimes of ~1ps.

In contrast, the charge recombination timescales (τ_2) have somewhat different dependencies with variation in acceptor for the **Si2s** and **Si4s** compounds: Amongst the **Si2s** compounds, the recombination timescale increases between **Si2s-2E** and **Si2s-E,C** and then decreases for **Si2s-2C**. In contrast, the charge recombination timescale increases monotonically with increasing acceptor strength across the series **Si4s-2E**, **Si4s-E,C**, and **Si4s-2C**. These variations result from the interplay of two factors: the structure-dependence of electronic coupling strength between the ground and charge-separated excited states, and variation in the free energy gap or driving force between charge-separated and ground states that result from the relative energetic stability of the charge-separated state as supported by the nature of the polar accepting groups.

The relative acceptor strength of the acceptor groups are summarized in Scheme 5.1d. This order is supported by calculated and measured electron affinities (EA) for similar ethylene electron accepting units. DFT calculations predict the EA of methyl-2-cyanoacrylate (similar to the **E,C** acceptor group) to be the same as ethyl-2-cyanoacrylate (1.08 eV),[37] which agrees well with experimental values reported at 0.9 ± 0.2 eV.[38] Replacing the ester with a second cyano group further increases the EA, where 1,1-dicyanoethylene (i.e. **2C** acceptor group) has a calculated EA of 1.36 eV;[37] similarly, trans 1,2-dicyanoethylene has a measured EA of 1.24 eV.[39] To our knowledge an EA for diethyl 2-methylenemalonate (i.e. **2E** acceptor group) has not been reported, but we expect that eliminating all electron withdrawing cyano groups should decrease the EA relative to methyl-2-cyanoacrylate (i.e. the **E,C** acceptor).

For a common silane donor, acceptor variation in EA should directly determine the structure-dependent driving force for back electron transfer (i.e. the driving force for charge recombination decreases when replacing a weak with a strong electron acceptor). Similarly, the

electron accepting strength should be expected to impact the electronic coupling strength (that is, stronger acceptors result in weaker electronic coupling for back electron transfer). We note that if the electronic coupling were the same for all of the structures studied here, we might expect the slowest recombination rates for the **2E** structures as they would have the largest driving force. Therefore, the very fast recombination rates observed for **Si*n*s-2E** compounds most likely arises from larger electronic coupling, *V*, relative to structures with **E,C** and **2C** acceptors.

We used our data to explore these expectations quantitatively. Back-electron transfer (BET) commonly occurs within the Marcus inverted regime following photoinduced charge separation, such that the BET rate (k_{BET}) is calculated as the Franck-Condon weighted sum of electron-transfer rates from the lowest-lying vibrational level of the charge-separated excited state to various vibrational levels (n) of the electronic ground state:[40-41]

$$k_{BET} = \frac{2\pi|V|^2}{\hbar\sqrt{4\lambda k_B T}} \sum_{n=0}^{\infty} e^{-S^2} \frac{S^n}{n!} \exp\left[-\frac{(\Delta G_0 + \lambda + n\hbar\omega)^2}{4\lambda k_B T}\right] \quad (5.3)$$

The BET rate therefore depends sensitively on the driving force for BET (ΔG_0), the electronic coupling between the initial charge-separated and final charge-recombined electronic states (V), the reorganization energies ($\lambda = \lambda_I + \lambda_S$, where I = intramolecular, S = solvent), as well as the frequency ($\hbar\omega$) and displacement (captured by the Huang-Rhys Factor $S = \lambda_I/\hbar\omega$) along the Franck-Condon active vibrational mode(s); additional terms in Equation 5.3 include Planck's and Boltzmann's constants, and temperature (T = 293 K). We applied this formalism to assess which parameter (V or ΔG_0) dominates the acceptor-dependent BET rates for organosilanes. Values for driving force and reorganization energies can be estimated from steady-state spectral data (*vide infra*). Our primary goal was to find values of V that agree with the experimentally measured charge-recombination lifetimes (τ_2) via Equation 5.3 using a minimization routine. These calculations necessarily required computational simplifications, such as assuming Franck-Condon

weighting with respect to a single vibrational mode, but are sufficient for identifying whether differences in electronic coupling vs. driving force dominantly impact the BET rate as the acceptor strength is varied.

Given that the charge-separated state is emissive, estimates for the total reorganization energy, λ, and the sum $\Delta G_0 + \lambda$ can be determined using the energies of peak emission ($\hbar\omega_{em}$) and absorption ($\hbar\omega_{abs}$) measured for each organosilane in DCM:[40, 42-43] $\Delta G_0 + \lambda$ is directly related to the peak emission gap (i.e. $-\hbar\omega_{em} = -\Delta G_0 + \lambda$). The total reorganization energy was calculated as $\lambda = 0.5(\hbar\omega_{abs} - \hbar\omega_{em})$; in practice we used the peak energy from the fluorescence excitation spectrum for $\hbar\omega_{abs}$ due to the overlap between the $\sigma \rightarrow \pi^*$ absorption transition, which populates the emissive charge-separated state, and the acceptor $\pi \rightarrow \pi^*$ absorption transition, which results in significantly weaker emission. We used the same method to determine the intramolecular reorganization energy, λ_I, using emission and fluorescence excitation spectra collected for organosilanes in cyclohexane (CH);[42] the static and optical dielectric constants of CH are identical, such that solvent reorganization energy is assumed to be negligible.

Table 5.2 summarizes our values for $-\hbar\omega_{em}$ and $\hbar\omega_{abs}$ in DCM and CH as well as our estimates of $\Delta G_0 + \lambda$, λ, and λ_I; spectral data for **Si2s-2E**, **Si2s-2C**, **Si4s-2E**, and **Si4s-2C** used for these determinations are presented in Appendix 3 (displayed in Figures A3.3-A3.6). Peak emission energies for **Si2s-E,C** and **Si4s-E,C** were taken from our previous work, in which we did not obtain fluorescence excitation spectra. The $\sigma \rightarrow \pi^*$ and $\pi \rightarrow \pi^*$ absorption transitions for these compounds overlap significantly; we therefore estimated $\hbar\omega_{abs}$ for the former using **Si*n*s-2C** as a reference and shifting by the relative red-edge absorption onset in **Si*n*s-E,C** vs. **Si*n*s-2C** compounds (a difference of ~0.1 eV in both cases).

Table 5.2. Summary of estimated values for parameters controlling back-electron-transfer rates in vinyl end-capped **Si*n*s** compounds. All values are in electron Volts (eV) unless stated otherwise. See text for details on methods of estimation.

	$\hbar\omega_{abs}$[a]	$-\hbar\omega_{em}$	λ[d]	ΔG_0[e]	V_1 (cm^{-1})[f]	V_2 (cm^{-1})[g]	$\bar{\nu}$ (cm^{-1})[h]
DCM							
Si2s-2C	3.573	-2.267	0.653	-2.948	310	134	2200
Si2s-E,C	3.648[b]	-2.29[c]	0.679	-2.972	199	84	2200
Si2s-2E	3.724	-2.412	0.656	-3.094	2193	1829	1700
Si4s-2C	3.416	-2.091	0.662	-2.773	192	96	2200
Si4s-E,C	3.519[b]	-2.13[c]	0.695	-2.812	256	124	2200
Si4s-2E	3.735	-2.246	0.744	-2.928	607	520	1700
CH							
Si2s-2C	3.605	-2.655	0.475	-3.140	2159	599	2200
Si2s-2E	3.899	-3.047	0.426	-3.531	-	-	1700
Si4s-2C	3.543	-2.578	0.482	-3.062	628	188	2200
Si4s-2E	3.746	-2.638	0.554	-3.123	3535 (2732)[i]	2794 (2159)[i]	1700

[a] Vertical absorption peak identified from fluorescence excitation spectrum unless noted otherwise.
[b] **Si*n*s-E,C** peak estimated relative to **Si*n*s-2C** using shift in red-edge absorption onset.
[c] From Reference 23.
[d] Total reorganization energy in DCM and CH; total reorganization in CH used as intramolecular reorganization energy. Average values used for calculations with Equation 5.3: $<\lambda>$ = 0.682 eV and $<\lambda_I>$ = 0.484 eV)
[e] Calculated as $\Delta G_0 = -\hbar\omega_{em} - <\lambda>$.
[f] Determined via Equation 5.3 using a common vibrational frequency (1615 cm^{-1}).
[g] Determined via Equation 5.3 using different vibrational frequencies for each acceptor.
[h] Vibrational frequencies used for V_2 calculations (approximate highest frequency for an unsaturated bond, C=O or CN).
[i] Determined using slowest possible recombination lifetime (75 ps) for **Si4s-2E** given large parameter error

We find that the total and intramolecular reorganization energies determined for the entire set of compounds are highly similar, with average values of $<\lambda>$ = 0.682 eV and $<\lambda_I>$ = 0.484 eV, respectively. From these values one calculates a solvent reorganization energy, λ_S, of ~0.2 eV in DCM, which is consistent with λ_S estimated independently from a Lippert-Mataga analysis of solvent-dependent emission Stokes' shifts for the **Si*n*s-E,C** end-capped compounds (see additional discussion in Appendix 3).[23, 42, 44-45] Given quantitative similarities across all structures, we used the average values for λ and λ_I in our calculations of V; we also estimated ΔG_0 for BET in each

compound using this common value for λ (Table 5.2). Importantly, the similarity in the reorganization energies for all structures reflects that the *emitting* state in each of these compounds is characteristically similar (i.e. regardless of acceptor identity they can all be classified as a charge-separated state).

We treated the Franck-Condon weighting with two approaches: First we assumed weighting for all compounds using a mode at a common frequency of 1615 cm^{-1}. A feature at this frequency dominates the pre-Resonant ground-state Raman spectrum we reported previously for **Si*n*s-E,C** structures;[23-24] we therefore assume that this mode is coupled to the $\sigma \rightarrow \pi^*$ optical charge transfer and expect that it also couples to back electron transfer. Calculation of the ground-state Raman spectrum of the organic acceptor shows that this feature corresponds with a symmetric phenylene-vinyl stretching mode. Our previous FSRS results also show that reduction of the acceptor only results in a modest (<100 cm^{-1}) shift in the frequency of this mode, which should not significantly impact predictions from our analysis of relative values of V. In a second approach we used a different effective vibrational frequency for each organic acceptor type. Specifically, we chose approximate frequencies corresponding with the strongest unsaturated bond in the acceptor moiety (e.g. C=O or CN); these vibrational frequencies are summarized in Table 5.2. This second approach was used to assess whether differences in the vibrational frequency (rather than driving force or electronic coupling) could underlie variations in BET rate between compounds.

Table 5.2 lists the value of V that reproduces the measured BET lifetimes via Equation 5.3. Notably, similar structure-dependent variations in V are observed with both FC-weighting schemes (compare V_1 and V_2): Relatively small electronic coupling terms (<200-300 cm^{-1}) were obtained for the **2C** and **E,C** end-capped structures – falling within the weak-coupling or nonadiabatic

electron-transfer limit. In contrast, V approaches or enters the strong-coupling or adiabatic electron-transfer limit for the **2E** end-capped oligosilanes (up to ~2000 cm^{-1} for **Si2s-2E**). This comparison highlights that the significantly higher BET rates (faster recombination lifetimes) measured for the **2E** structures must result from a dramatic change in state coupling to counteract the decrease in rate expected from the relative increase in ΔG_0 (Table 5.2)

Differences in values for V obtained for the **E,C** and **2C** acceptors are much smaller (within a factor of 2), indicating that presence of a single cyano electron-withdrawing group on the acceptor may be sufficient to reduce the electronic coupling to within the weak-coupling limit in DCM. Notably, all electronic coupling terms are on average lower for the **Si4s** vs. **Si2s** structures, which is consistent with increased hole delocalization along the sigma-conjugated silane chain and that the positive core is harder to shield from the reduced acceptor on the shorter silane chain. Finally, the longer charge-separation lifetime (slower recombination rate) for **Si2s** vs. **Si4s E,C** and **2C** is primarily controlled by the larger driving force for BET for the former.

5.4.c. Tuning photoinduced charge-separation lifetimes in Si*n*s organosilanes with local chemical environment.

Having established that charge-recombination lifetimes are considerably shorter for organosilane structures with weaker diester-vinyl electron acceptors due to increased electronic coupling, we sought to determine whether stronger acceptors would allow for increasing excited-state lifetimes in low polarity material environments. The prescription for this involves reducing the solvent reorganization energy, which according to Marcus theory should result in longer charge-separation lifetimes in the inverted regime when the driving force remains constant (i.e. no

change in donor or acceptor groups). Variation in reorganization energy can be achieved nominally by varying the solvent dielectric constant or polarity.

Accordingly, we collected transient absorption data with **Si2s-E,C**, **Si4s-2E**, **Si2s-2C**, and **Si4s-2C** in cyclohexane (CH). Figure 5.4 presents transient spectra along with results from global analysis for **Si2s-E,C**. Figure 5.5 presents transient absorption (plotted with contours) along with results from global analysis for **Si4s-2E** and **Si4s-2C**. Transient absorption data and results from global analysis for **Si2s-2C** are presented in Figures A3.7; the transient spectra at selected time delays for **Si4s-2E** and **Si4s-2C** are also presented in Figures A3.8 and A3.9.

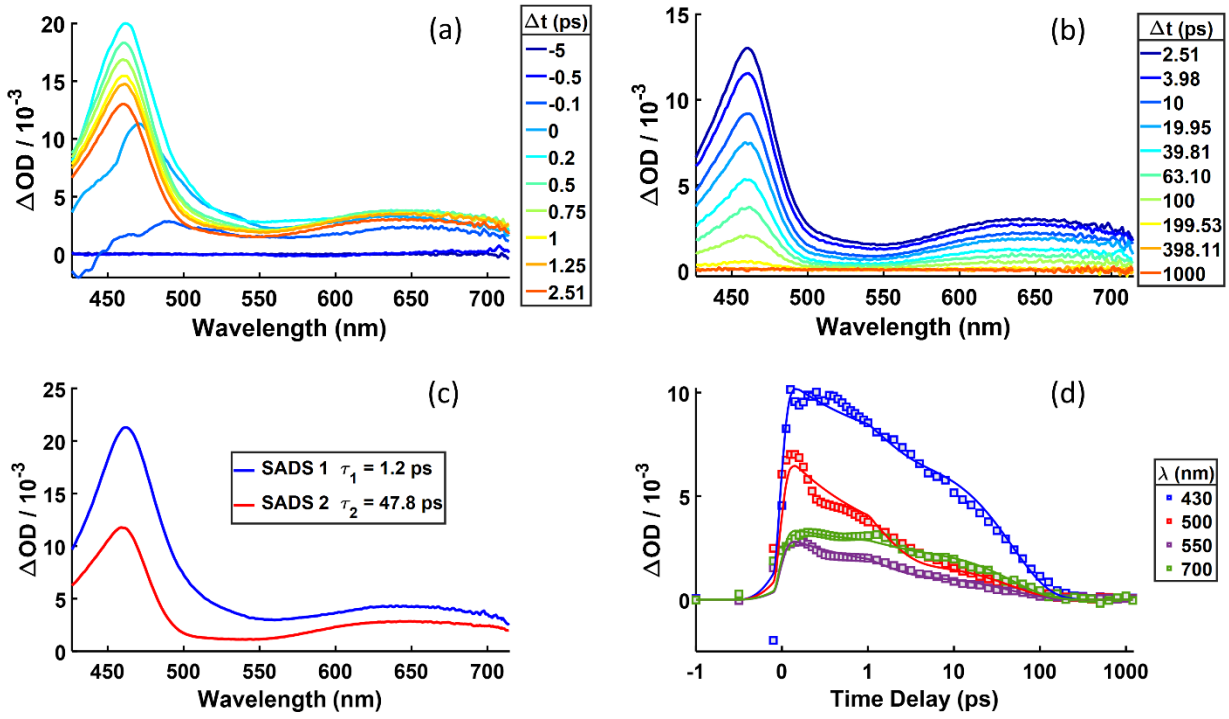

Figure 5.4. Transient absorption of **Si2s-E,C** dissolved in CH excited at 360 nm (a) before and (b) after 3 ps. (c) species associated difference spectra and (d) temporal traces at selected wavelengths plotted with fits, obtained from global analysis with the kinetic model presented in Equation 5.2.

Generally speaking, the transient spectra of these compounds in CH exhibit an ESA band centered around 475 nm, as well as absorption above 600 nm; however, clear SE bands do not appear. In our previous work, a bathochromic shift in fluorescence with decreasing solvent dielectric strength was observed for **Si*n*s-E,C**, which exhibited a peak emission between 475 nm and 500 nm in toluene. Hence, the fact that we see no clear SE band in CH likely arises from a strong overlap between the ESA and SE bands at shorter wavelengths (this is verified by comparing ESA features to the emission spectra presented in Appendix 3, figures A3.3-A3.6). The dip in the transient spectral intensity 500-550 nm is suggestive of ESA + SE overlap in these systems.

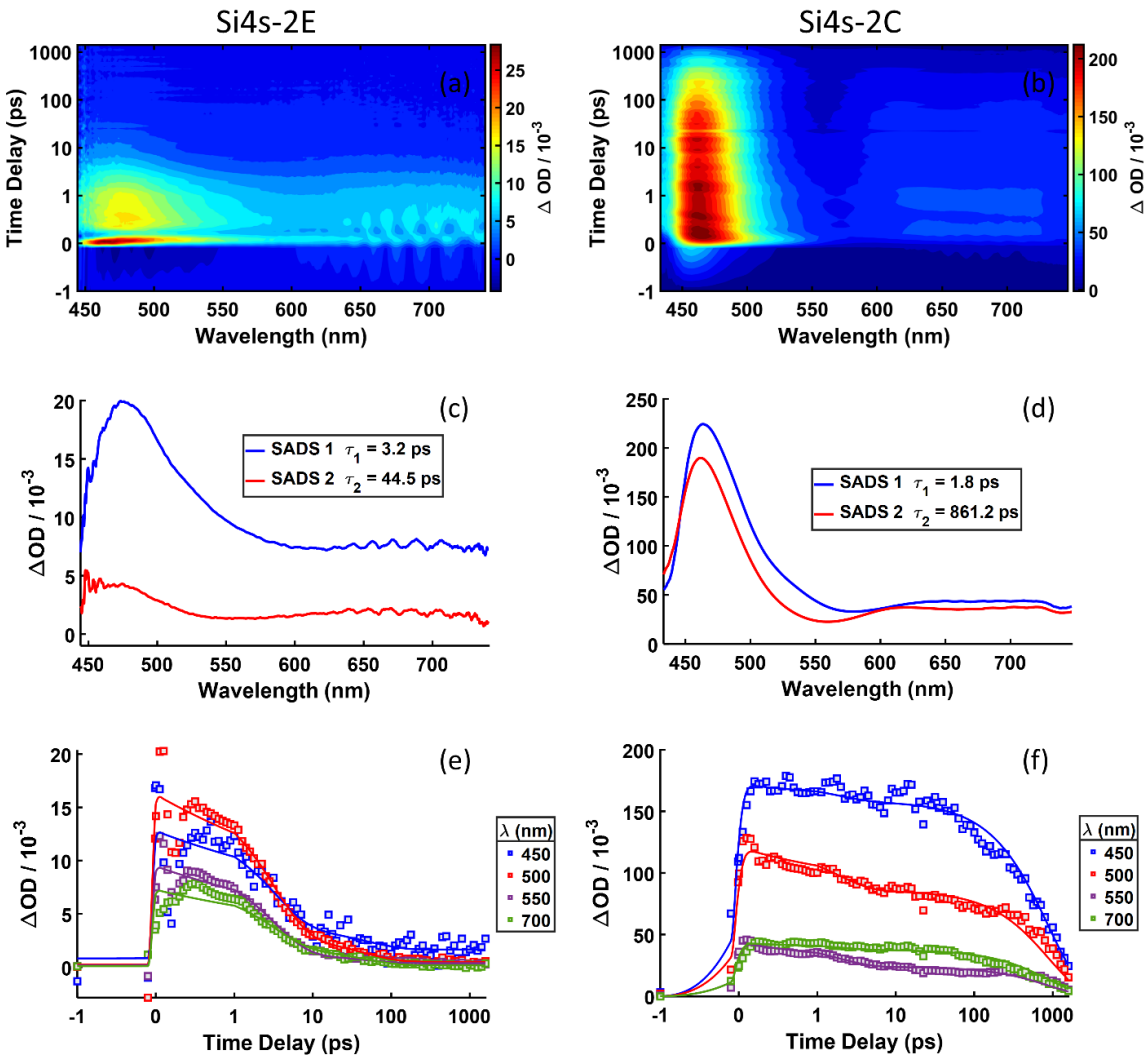

Figure 5.5. Transient absorption of **Si4s-2E** (left panel) and **Si4s-2C** (right panel) dissolved in CH excited at 360 nm. Contour plots of TA data for **Si4s-2E** (a) and **Si4s-2C** (b). SADS for **Si4s-2E** (c) and **Si4s-2C** (d), and fits to kinetic traces at selected probe wavelengths for **Si4s-2E** (e) and **Si4s-2C** (f), obtained from global analysis with the kinetic model presented in Equation 5.2.

We fit each set of data globally according to the kinetic model in Equation 5.2. Lifetimes obtained from these fits are presented in Table 5.3. The marked decrease in the charge recombination lifetime for **Si2s-E,C** (680 vs. 47.8 ps) when going from DCM to CH was highly surprising, as we anticipated that the rate of electron transfer should decrease for a decrease in total reorganization energy (i.e. CH < DCM). In our previous work, increasing the solvent polarity (and

nominally reorganization energy for the nascent charge-separated pair) amongst a set of moderately to strongly polar solvents (DCM, chloroform, acetonitrile) resulted in the expected increase in back-electron transfer rate in the inverted regime. Thus, we conclude that the faster recombination observed for **Si*n*s-E,C** in CH vs. DCM reveals that the solvent impacts both the reorganization energy and electronic coupling strength for charge recombination for these compounds. In short, nonpolar CH is much less effective at screening separated charge pairs, resulting in much faster recombination than would be expected based on variation in reorganization energy.

Table 5.3. Excited state relaxation (τ_1) and charge recombination (τ_2) for **Si2s** and **Si4s** organosilanes dissolved in cyclohexane under 360 nm excitation. Timescales were obtained from global fitting data to the kinetic model summarized in Equation 5.2.

Compound	τ_1 (ps)	τ_2 (ps)
Si2s-E,C	1.2 ± 0.2	48 ± 5
Si4s-2E	3.2 ± 0.7	45 ± 30
Si2s-2C	2.4 ± 0.5	137 ± 8
Si4s-2C	1.8 ± 0.4	860 ± 40

We applied the same calculational approaches used above to rationalize the relative timescales (τ_2) for BET in CH; results are summarized in Table 5.2. Here the intramolecular reorganization energy was used also for the total reorganization energy. We see similar qualitative structure-dependent variation in V as was obtained for BET in DCM: The rapid recombination rate observed for **Si4s-2E** requires very strong coupling. Recombination rates for **2C** structures are consistent with weaker coupling; we find that the magnitude of V obtained is sensitive to our

Franck-Condon weighting procedure, but in both cases predicts much weaker coupling for **Si4s-2C** than **Si2s-2C**. The overall increase in V from DCM to CH solvent environments indicates that solvent-solute interactions have a significant impact on the magnitude of electronic coupling and is consistent with the dramatic increase in recombination rate observed for **Si2s-E,C** in CH.

Importantly, the combination of strong donor-acceptor pairs (**Si4s-2C**) is observed to produce an extended charge-separation lifetime in CH, 861.2 ps, compared to DCM, 177.4 ps. However, we do not see an enhancement in the charge-recombination lifetime for **Si2s-2C** in CH, 137.2 ps compared to 237.1 ps in DCM. This difference is attributable to increased electronic coupling in **Si2s-2C**, which is exacerbated by the weaker charge-screening solvent environment in cyclohexane, thereby favoring faster charge recombination. For **Si4s-2C**, greater charge-pair separation lowers the electronic coupling, such that the very low reorganization energy of cyclohexane (relative to DCM and other weakly to moderately polar solvents) places back-electron transfer even further into the inverted regime, with a resultant increase in charge recombination lifetime. Hence, when stronger silane donors are combined with strong organic acceptors, charge-recombination rates (and therefore charge-separation lifetimes) exhibit the decrease (dilation) predicted by Marcus theory with decreasing solvent reorganization energy.

Finally, we note that there is a significant drop in the transient spectral intensity on τ_1 for the organosilanes that exhibit larger values of V for BET in CH. Specifically, **Si4s-2E** in CH exhibits a ~ 75% decrease in spectral intensity (Figure 5.5c) on a timescale of 3.2 ps, whereas **Si2s-E,C** in CH exhibits a ~ 50% decrease in spectral intensity (Figure 5.4c) on a timescale of 1.2 ps. Similar deactivation is observed for **Si2s-2E** in chloroform; Figure A3.10 presents transient absorption spectra with results from global analysis, where a >50% decay in spectral intensity is observed on a timescale of 2.5 ps. Emission from organosilanes in CH and other low polarity

solvents occurs between 400 and 500 nm, such that this could arise in part from a strong overlap between the ESA and stimulated emission from the relaxed excited-state configuration. However, dramatic decreases in spectral intensity on a fast timescale are not observed for **Si2s-2C** or **Si4s-2C** in CH, both of which also have ESA and emission features that strongly overlap. We therefore ascribe this excited-state signal decay to a significant rapid component to back-electron transfer within the strongly-coupled limit. Biphasic electron transfer is plausible within the adiabatic limit, in which electron transfer occurs by barrier crossing: Prior to a complete structural relaxation, the nascent excited organosilane has sufficient energy to overcome the adiabatic barrier for electron transfer. Following this initial dissipation of excess energy, subsequent ET must occur from a relaxed state, such that crossing the adiabatic barrier will occur at a slower rate. In summary, while the timescale τ_1 is likely associated with solvent and structural reorganization for all photoexcited organosilanes regardless of the magnitude of V for BET, rapid charge-recombination occurs in parallel with this reorganization in organosilanes that are characterized by strong-coupling conditions (i.e. organosilanes with weak to moderate strength acceptors (**Si*n*s-2E** and **Si*n*s-E,C**) dissolved in weakly polar solvents (CH)).

5.5 Conclusion

In summary, we have characterized the photophysics of dicyanovinyl and diestervinyl end-capped organosilanes in weakly polar solvents. Steady-state UV-Vis and excited-state transient absorption spectra collected with **Si*n*s-2E** and **Si*n*s-2C** exhibit spectral features that are qualitatively similar to those previously observed for **Si*n*s-E,C**. Spectral dynamics observed by ultrafast TA therefore are attributed to a common sequence of deactivation processes: excited-state relaxation followed by charge recombination to the ground state. We have shown that

relaxation of the "hot" charge-separated excited state depends on dipole-dipole interactions between solvent and polar acceptor groups, where relaxation lifetimes in **Si2s** and **Si4s** structures scale with increasing polarity (i.e. **Si*n*s-2E** < **Si*n*s-E,C** < **Si*n*s-2C**). In weakly polar solvents (DCM) the choice of electron acceptor determines whether electronic coupling dominates driving force to control the charge recombination rate: organosilanes with weak acceptors (**Si*n*s-2E**) possess poorly stabilized charge-separated excited states with increased electronic coupling to the neutral ground state, whereas organosilanes with strong acceptors (**Si*n*s-2C**) form very stable charge-separated states with weaker electronic coupling.

Furthermore, in contrast to predictions for electron-transfer rates via Marcus theory, weak- and moderate-strength donor-acceptor pairings (**Si*n*s-2E** and **Si*n*s-E,C**) exhibit faster recombination with a decrease in solvent reorganization energy (i.e. $\lambda_{CH} < \lambda_{DCM}$). We attribute this faster recombination to a larger electronic coupling as the charge pairs are poorly screened by nonpolar solvents. In these cases, a significant decay of transient spectral intensity (and therefore excited-state population) is observed on very rapid timescales, indicating very fast charge recombination for weaker donor-acceptor pairs (i.e. occurring in parallel with excited-state relaxation) that is consistent with BET in the adiabatic limit. This behavior is not observed in the strongest donor-acceptor pairs, **Si4s-2C**, where the electronic coupling is much smaller and the charge-separation lifetime can be increased in nonpolar chemical environments that have very low reorganization energies. Together these results aid in our understanding of organosilane structure-function relationships to help guide the design of molecules for which intramolecular charge transfer may be tuned to generate long-lived charge-separated states with potential material applications in molecular- and opto-electronics.

Supporting Information

Additional transient absorption and steady-state emission data and analysis for **Si2s-2E**, **Si4s-2E**, **Si2s-2C**, and **Si4s-2C** organosilanes. This material is presented in Appendix 3.

Acknowledgements

Spectroscopic studies presented in this work were supported by the National Science Foundation (NSF), CHE-1455009 (A. E. B.). R. S. K. thanks the Alfred P. Sloan Foundation for a Sloan Research Fellowship.

5.6 References

1. Yuvaraja, S.; Nawaz, A.; Liu, Q.; Dubal, D.; Surya, S. G.; Salama, K. N.; Sonar, P., Organic Field-Effect Transistor-Based Flexible Sensors. *Chem. Soc. Rev.* **2020**, *49*, 3423-3460.

2. Liu, Y. C.; Li, C. S.; Ren, Z. J.; Yan, S. K.; Bryce, M. R., All-Organic Thermally Activated Delayed Fluorescence Materials for Organic Light-Emitting Diodes. *Nat. Rev. Mater.* **2018**, *3*, 18020.

3. Inganas, O., Organic Photovoltaics over Three Decades. *Adv. Mater.* **2018**, *30*, 1800388.

4. Lou, A. J. T.; Marks, T. J., A Twist on Nonlinear Optics: Understanding the Unique Response of Pi-Twisted Chromophores. *Acc. Chem. Res.* **2019**, *52*, 1428-1438.

5. Ostroverkhova, O., Organic Optoelectronic Materials: Mechanisms and Applications. *Chem. Rev.* **2016**, *116*, 13279-13412.

6. Fogarty, H. A.; Casher, D. L.; Imhof, R.; Schepers, T.; Rooklin, D. W.; Michl, J., Sigma Bonds: Electronic Structure, Photophysics, and Photochemistry of Oligosilanes. *Pure Appl. Chem.* **2003**, *75*, 999-1020.

7. Gilman, H.; Atwell, W. H.; Schwebke, G. L., Ultraviolet Properties of Compounds Containing the Silicon-Silicon Bond. *J. Organomet. Chem.* **1964**, *2*, 369-371.

8. Klausen, R. S.; Widawsky, J. R.; Steigerwald, M. L.; Venkataraman, L.; Nuckolls, C., Conductive Molecular Silicon. *J. Am. Chem. Soc.* **2012**, *134*, 4541-4544.

9. Li, H. X., et al., Large Variations in the Single-Molecule Conductance of Cyclic and Bicyclic Silanes. *J. Am. Chem. Soc.* **2018**, *140*, 15080-15088.

10. Su, T. A.; Li, H. X.; Klausen, R. S.; Kim, N. T.; Neupane, M.; Leighton, J. L.; Steigerwald, M. L.; Venkataraman, L.; Nuckolls, C., Silane and Germane Molecular Electronics. *Acc. Chem. Res.* **2017**, *50*, 1088-1095.

11. Okumoto, H.; Yatabe, T.; Richter, A.; Peng, J. B.; Shintomura, M.; Kaito, A.; Minami, N., A Strong Correlation between the Hole Mobility and Silicon Chain Length in Oligosilane Self-Organized Thin Films. *Adv. Mater.* **2003**, *15*, 716-720.

12. Miller, R. D.; Michl, J., Polysilane High Polymers. *Chem. Rev.* **1989**, *89*, 1359-1410.

13. Karatsu, T., Photochemistry and Photophysics of Organomonosilane and Oligosilanes: Updating Their Studies on Conformation and Intramolecular Interactions. *J. Photochem. Photobiol., C* **2008**, *9*, 111-137.

14. Traven, V. F.; West, R., Charge-Transfer Complexing between Permethylpolysilanes and Tetracyanoethylene. *J. Am. Chem. Soc.* **1973**, *95*, 6824-6826.

15. vanHutten, P. F.; Hadziioannou, G.; Burst, R.; Feil, D., Calculation of the Hyperpolarizabilities of Silicon-Based Donor-Acceptor Compounds for Nonlinear Optics. *J. Phys. Chem.* **1996**, *100*, 85-94.

16. Usuki, T.; Shimada, M.; Yamanoi, Y.; Ohto, T.; Tada, H.; Kasai, H.; Nishibori, E.; Nishihara, H., Aggregation-Induced Emission Enhancement from Disilane-Bridged Donor-Acceptor-Donor Luminogens Based on the Triarylamine Functionality. *ACS Appl. Mater. Interfaces* **2018**, *10*, 12164-12172.

17. Shimada, M.; Tsuchiya, M.; Sakamoto, R.; Yamanoi, Y.; Nishibori, E.; Sugimoto, K.; Nishihara, H., Bright Solid-State Emission of Disilane-Bridged Donor-Acceptor-Donor and Acceptor-Donor-Acceptor Chromophores. *Angew. Chem., Int. Ed.* **2016**, *55*, 3022-3026.

18. Cho, Y. J.; Lee, A. R.; Kim, S. Y.; Cho, M. J.; Han, W. S.; Son, H. J.; Cho, D. W.; Kang, S. O., The Influence of Pi-Conjugation on Competitive Pathways: Charge Transfer or Electron Transfer in New D-π-A and D-π-Si-π-A Dyads. *Phys. Chem. Chem. Phys.* **2016**, *18*, 22921-22928.

19. Shimada, M.; Yamanoi, Y.; Matsushita, T.; Kondo, T.; Nishibori, E.; Hatakeyama, A.; Sugimoto, K.; Nishihara, H., Optical Properties of Disilane-Bridged Donor Acceptor Architectures: Strong Effect of Substituents on Fluorescence and Nonlinear Optical Properties. *J. Am. Chem. Soc.* **2015**, *137*, 1024-1027.

20. Folster, C. P.; Nguyen, P. N.; Siegler, M. A.; Klausen, R. S., Tunable Sin Hybrid Conjugated Materials. *Organometallics* **2019**, *38*, 2902-2909.

21. Purkait, T. K.; Press, E. M.; Marro, E. A.; Siegler, M. A.; Klausen, R. S., Low-Energy Electronic Transition in Sib Rings. *Organometallics* **2019**, *38*, 1688-1698.

22. Surampudi, S.; Yeh, M. L.; Siegler, M. A.; Hardigree, J. F. M.; Kasl, T. A.; Katz, H. E.; Klausen, R. S., Increased Carrier Mobility in End-Functionalized Oligosilanes. *Chem. Sci.* **2015**, *6*, 1905-1909.

23. Zhou, J. W.; Folster, C. P.; Surampudi, S. K.; Jimenez, D.; Klausen, R. S.; Bragg, A. E., Asymmetric Charge Separation and Recombination in Symmetrically Functionalized Sigma-Pi Hybrid Oligosilanes. *Dalton Trans.* **2017**, *46*, 8716-8726.

24. Zhou, J. W.; Surampudi, S. K.; Bragg, A. E.; Klausen, R. S., Photoinduced Charge Separation in Molecular Silicon. *Chem. - Eur. J.* **2016**, *22*, 6204-6207.

25. Wasielewski, M. R.; Niemczyk, M. P.; Svec, W. A.; Pewitt, E. B., Dependence of Rate Constants for Photoinduced Charge Separation and Dark Charge Recombination on the Free-Energy of Reaction in Restricted-Distance Porphyrin Quinone Molecules. *J. Am. Chem. Soc.* **1985**, *107*, 1080-1082.

26. Marcus, R. A., On the Theory of Oxidation-Reduction Reactions Involving Electron Transfer 1. *J. Chem. Phys.* **1956**, *24*, 966-978.

27. Cody, J.; Mandal, S.; Yang, L. C.; Fahrni, C. J., Differential Tuning of the Electron Transfer Parameters in 1,3,5-Triarylpyrazolines: A Rational Design Approach for Optimizing the Contrast Ratio of Fluorescent Probes. *J. Am. Chem. Soc.* **2008**, *130*, 13023-13032.

28. Akbarimoosavi, M.; Rohwer, E.; Rondi, A.; Hankache, J.; Geng, Y.; Decurtins, S.; Hauser, A.; Liu, S. X.; Feurer, T.; Cannizzo, A., Tunable Lifetimes of Intramolecular Charge-Separated States in Molecular Donor-Acceptor Dyads. *J. Phys. Chem. C* **2019**, *123*, 8500-8511.

29. Hyun, B. R.; Bartnik, A. C.; Lee, J. K.; Imoto, H.; Sun, L. F.; Choi, J. J.; Chujo, Y.; Hanrath, T.; Ober, C. K.; Wise, F. W., Role of Solvent Dielectric Properties on Charge Transfer from Pbs Nanocrystals Molecules. *Nano Lett.* **2010**, *10*, 318-323.

30. Ratera, I.; Sporer, C.; Ruiz-Molina, D.; Ventosa, N.; Baggerman, J.; Brouwer, A. M.; Rovira, C.; Veciana, J., Solvent Tuning from Normal to Inverted Marcus Region of Intramolecular Electron Transfer in Ferrocene-Based Organic Radicals. *J. Am. Chem. Soc.* **2007**, *129*, 6117-6129.

31. Benniston, A. C.; Harriman, A., Charge on the Move: How Electron-Transfer Dynamics Depend on Molecular Conformation. *Chem. Soc. Rev.* **2006**, *35*, 169-179.

32. Gust, D.; Moore, T. A.; Moore, A. L., Molecular Mimicry of Photosynthetic Energy and Electron-Transfer. *Acc. Chem. Res.* **1993**, *26*, 198-205.

33. Molloy, M. S.; Snyder, J. A.; Bragg, A. E., Structural and Solvent Control of Nonadiabatic Photochemical Bond Formation: Photocyclization of O-Terphenyl in Solution. *J. Phys. Chem. A* **2014**, *118*, 3913-3925.

34. Yu, W. J.; Magnanelli, T. J.; Zhou, J. W.; Bragg, A. E., Structural Heterogeneity in the Localized Excited States of Poly(3-Hexylthiophene). *J. Phys. Chem. B* **2016**, *120*, 5093-5102.

35. Dereka, B.; Rosspeintner, A.; Li, Z.; Liska, R.; Vauthey, E., Direct Visualization of Excited-State Symmetry Breaking Using Ultrafast Time-Resolved Infrared Spectroscopy. *J. Am. Chem. Soc.* **2016**, *138*, 4643-4649.

36. Niu, A.; Kuang, Z.; Planells, M.; Guo, Y.; Robertson, N.; Xia, A., Electron-Donating Strength Dependent Symmetry Breaking Charge Transfer Dynamics of Quadrupolar Molecules. *Phys. Chem. Chem. Phys.* **2020**, *22*, 15743-15750.

37. Brinkmann, N. R.; Schaefer, H. F.; Sanderson, C. T.; Kutal, C., Can the Radical Anion of Alkyl-2-Cyanoacrylates Initiate Anionic Polymerization of These Instant Adhesive Monomers? *J. Phys. Chem. A* **2002**, *106*, 847-853.

38. Zhang, X. X.; Tang, X.; Bowen, K., Photoelectron Spectroscopic Study of the Ethyl Cyanoacrylate Anion. *Chem. Phys. Lett.* **2013**, *582*, 21-23.

39. Chowdhury, S.; Kebarle, P., Electron-Affinities of Dicyanoethylene and Tetracyanoethylene and Cyanobenzenes Based on Measurements of Gas-Phase Electron-Transfer Equilibria. *J. Am. Chem. Soc.* **1986**, *108*, 5453-5459.

40. Jortner, J., Temperature Dependent Activation Energy for Electron Transfer between Biological Molecules. *J. Chem. Phys.* **1976**, *64*, 4860-4867.

41. Barbara, P. F.; Meyer, T. J.; Ratner, M. A., Contemporary Issues in Electron Transfer Research. *J. Phys. Chem.* **1996**, *100*, 13148-13168.

42. Solís, C.; Grosso, V.; Faggioli, N.; Cosa, G.; Romero, M.; Previtali, C.; Montejano, H.; Chesta, C., Estimation of the Solvent Reorganization Energy and the Absolute Energy of Solvation of Charge-Transfer States from Their Emission Spectra. *Photochem. Photobiol. Sci.* **2010**, *9*, 675-686.

43. Newton, M. D.; Sutin, N., Electron Transfer Reaction in Condensed Phases. *Annu. Rev. Phys. Chem.* **1984**, *35*, 437-480.

44. Lippert, E., Spektroskopische Bestimmung Des Dipolmomentes Aromatischer Verbindungen Im Ersten Angeregten Singulettzustand. *Ber. Bunsen. Phys. Chem.* **1957**, *61*, 962–975.

45. Mataga, N.; Kaifu, Y.; Koizumi, M., Fluorescence Spectra and the Dipolemoments of Excited Molecules. *Bull. Chem. Soc. Jpn.* **1956**, *29*, 465-470.

Appendix 1

Supporting Information for Chapter 3

Solvent Effects on Formation of Donor-Acceptor Charge-Transfer Complexes: N,N'-Diphenyl-N-N'-di-p-tolylbenzene-1,4-diamine (MPDA) and 2,3,5,6-tetrafluoro-7,7,8,8-tetracyanoquinodimethane (F_4TCNQ)

Table A1.1. Donor and acceptor concentrations for samples dissolved in 1,2-Dichloroethane with corresponding absorbance at 750 nm. Measurements collected at room temperature.

[F_4TCNQ] × 10^{-5} (M)	[MPDA] × 10^{-5} (M)	OD (750 nm)
3.47	4.36	0.583
3.47	5.81	0.662
3.47	7.26	0.722
3.47	8.72	0.759
3.47	10.2	0.783
3.47	11.6	0.774
3.47	13.1	0.801
3.47	14.5	0.812
3.47	16.0	0.825
3.47	17.4	0.805
3.47	18.9	0.832
3.47	20.3	0.821
3.47	21.8	0.829
3.47	23.2	0.802
3.47	24.7	0.794

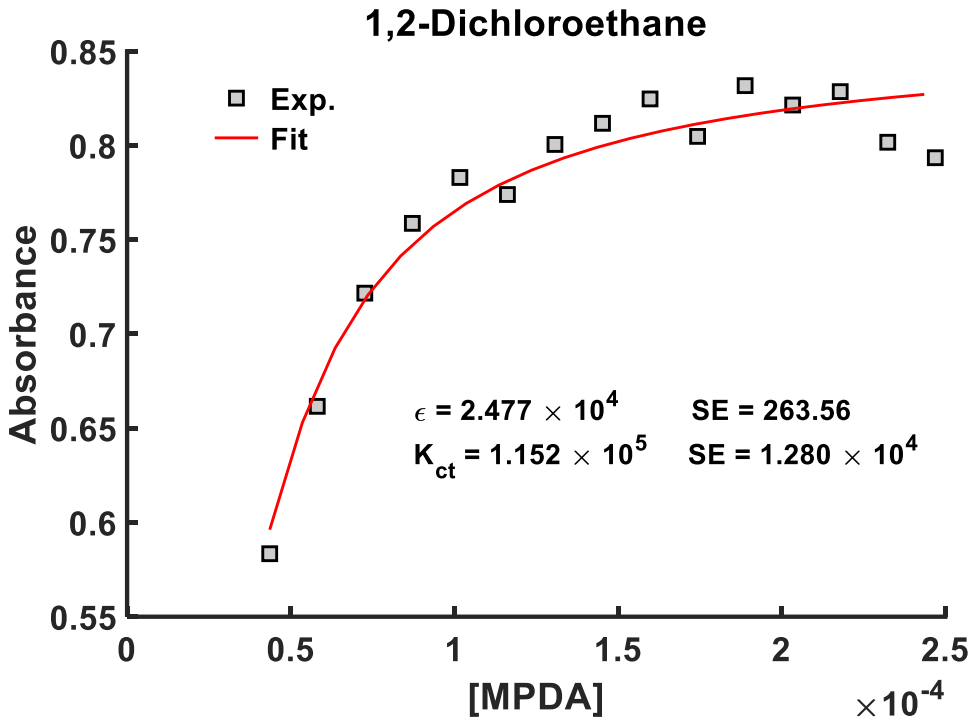

Figure A1.1. Absorption trace at 750 nm for data in Table A1.1 of $F_4TCNQ^{\cdot-}$:$MPDA^+$ CTC solutions dissolved in 1,2-Dichloroethane. Nonlinear fit according to Equation 3.3. Measurements collected at room temperature.

Table A1.2. Donor and acceptor concentrations for samples dissolved in 1,2-Dichlorobenzene with corresponding absorbance at 750 nm. Measurements collected at room temperature.

[F_4TCNQ] × 10^{-5} (M)	[MPDA] × 10^{-5} (M)	OD (750 nm)
1.99	1.45	0.209
1.99	2.18	0.265
1.99	2.91	0.269
1.99	3.64	0.305
1.99	4.36	0.326
1.99	5.09	0.328
1.99	5.82	0.334
1.99	6.54	0.352
1.99	7.27	0.361
1.99	8.00	0.362
1.99	8.72	0.376
1.99	9.45	0.388
1.99	10.2	0.380
1.99	10.9	0.385
1.99	11.6	0.391
1.99	12.4	0.397

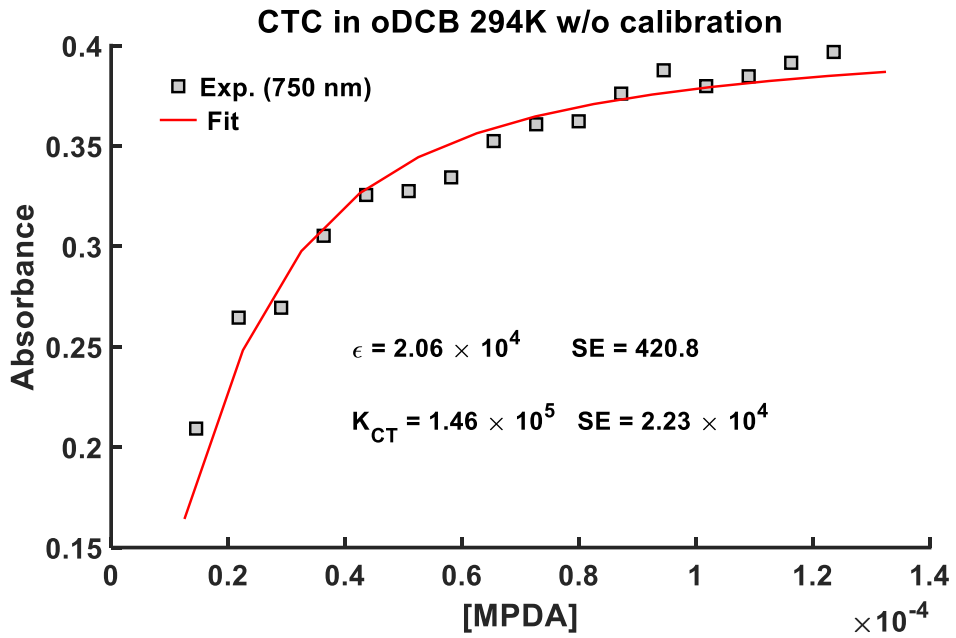

Figure A1.2. Absorption trace at 750 nm for data in Table A1.2 of $F_4TCNQ^{\cdot-}$:$MPDA^+$ CTC solutions dissolved in 1,2-Dichlorobenzene. Nonlinear fit according to Equation 3.3. Measurements collected at room temperature.

Table A1.3. Donor and acceptor concentrations for samples dissolved in Chlorobenzene with corresponding absorbance at 750 nm. Measurements collected at room temperature.

[F_4TCNQ] × 10^{-5} (M)	[MPDA] × 10^{-5} (M)	OD (750 nm)
5.98	4.24	0.020
5.98	6.36	0.031
5.98	8.48	0.043
5.98	10.6	0.050
5.98	12.7	0.056
5.98	14.8	0.062
5.98	17.0	0.068
5.98	19.1	0.073
5.98	21.2	0.078
5.98	23.3	0.084
5.98	25.5	0.096
5.98	27.6	0.100
5.98	29.7	0.107
5.98	31.8	0.112
5.98	33.9	0.118
5.98	36.1	0.123

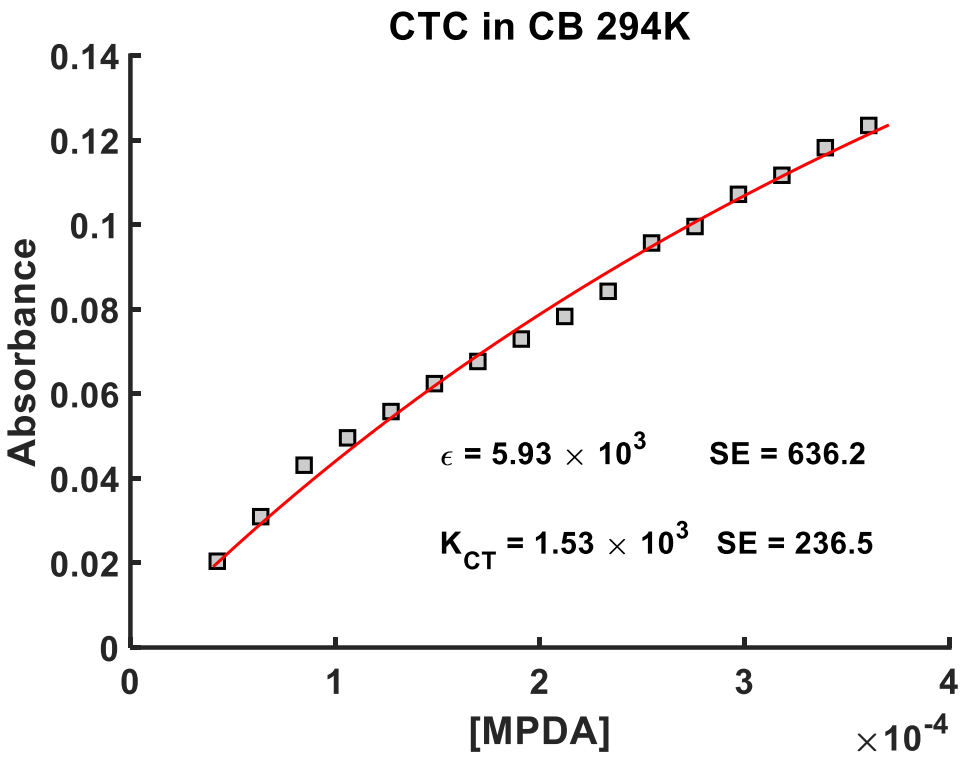

Figure A1.3. Absorption trace at 750 nm for data in Table A1.3 of $F_4TCNQ^{\cdot-}$:$MPDA^+$ CTC solutions dissolved in Chlorobenzene. Nonlinear fit according to Equation 3.3. Measurements collected at room temperature.

Table A1.4. Donor and acceptor concentrations for samples dissolved in Chloroform with corresponding absorbance at 750 nm. Measurements collected at room temperature.

[F_4TCNQ] × 10^{-5} (M)	[MPDA] × 10^{-5} (M)	OD (750 nm)
2.94	3.06	0.145
2.94	4.09	0.184
2.94	5.11	0.212
2.94	6.13	0.239
2.94	7.15	0.265
2.94	8.17	0.292
2.94	9.19	0.307
2.94	10.2	0.331
2.94	11.2	0.349
2.94	12.3	0.369
2.94	13.3	0.390
2.94	14.3	0.401
2.94	15.3	0.420
2.94	16.3	0.433
2.94	17.4	0.448
2.94	30.6	0.145

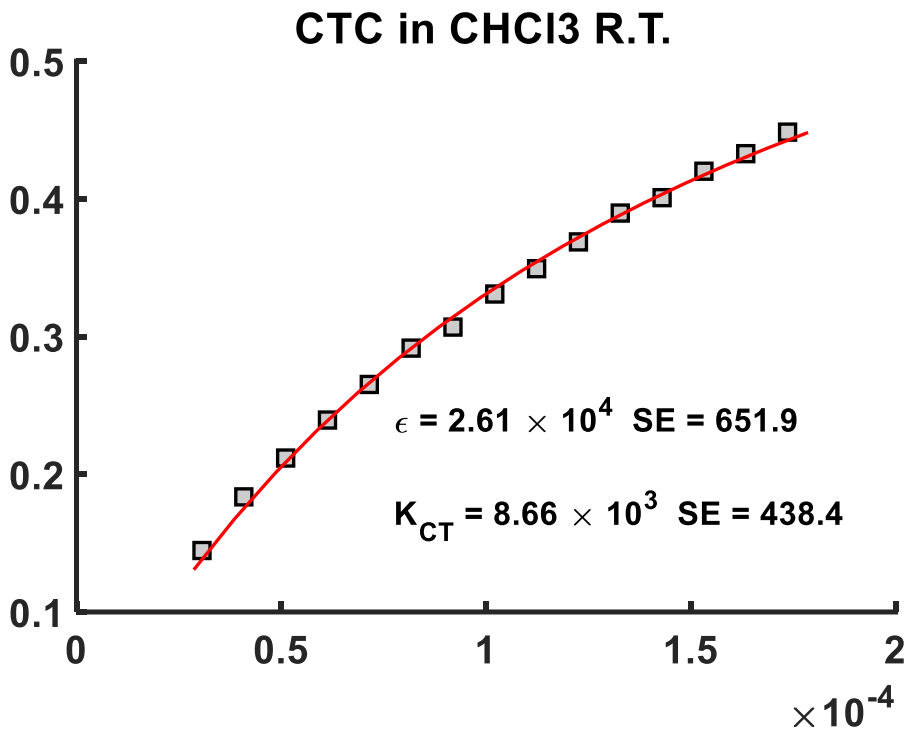

Figure A1.4. Absorption trace at 750 nm for data in Table A1.4 of $F_4TCNQ^{\cdot-}$:$MPDA^+$ CTC solutions dissolved in Chloroform. Nonlinear fit according to Equation 3.3. Measurements collected at room temperature.

Table A1.5. Donor and acceptor concentrations for samples dissolved in 1,2-Dichlorobenzene with corresponding absorbance at 750 nm. Measurements collected at labeled temperatures.

[F_4TCNQ] × 10^{-5} (M)	[MPDA] × 10^{-5} (M)	OD R.T.	OD 35°C	OD 45°C	OD 55°C	OD 65°C
1.99	1.45	0.209	0.145	0.129	0.114	0.104
1.99	2.18	0.265	0.214	0.189	0.161	0.144
1.99	2.91	0.269	0.233	0.210	0.180	0.163
1.99	3.64	0.305	0.261	0.235	0.203	0.182
1.99	4.36	0.326	0.268	0.241	0.215	0.194
1.99	5.09	0.328	0.279	0.250	0.223	0.200
1.99	5.82	0.334	0.282	0.261	0.231	0.210
1.99	6.54	0.352	0.292	0.272	0.246	0.221
1.99	7.27	0.361	0.307	0.281	0.253	0.232
1.99	8.00	0.362	0.312	0.288	0.261	0.237
1.99	8.72	0.376	0.325	0.299	0.271	0.249
1.99	9.45	0.388	0.339	0.314	0.284	0.263
1.99	10.2	0.380	0.333	0.308	0.284	0.263
1.99	10.9	0.385	0.344	0.316	0.292	0.268
1.99	11.6	0.391	0.348	0.325	0.290	0.274
1.99	12.4	0.397	0.350	0.328	0.298	0.284

Table A1.6. Donor and acceptor concentrations for samples dissolved in Chlorobenzene with corresponding absorbance at 750 nm. Measurements collected at labeled temperatures.

[F_4TCNQ] × 10^{-5} (M)	[MPDA] × 10^{-5} (M)	OD R.T.	OD 35°C	OD 55°C	OD 65°C
5.98	4.24	0.020	0.021	0.017	0.017
5.98	6.36	0.031	0.030	0.020	0.022
5.98	8.48	0.043	0.034	0.026	0.028
5.98	10.6	0.050	0.039	0.028	0.032
5.98	12.7	0.056	0.045	0.031	0.038
5.98	14.8	0.062	0.048	0.038	0.039
5.98	17.0	0.068	0.052	0.039	0.043
5.98	19.1	0.073	0.059	0.045	0.047
5.98	21.2	0.078	0.064	0.048	0.047
5.98	23.3	0.084	0.066	0.052	0.052
5.98	25.5	0.096	0.074	0.056	0.056
5.98	27.6	0.100	0.081	0.059	0.063
5.98	29.7	0.107	0.086	0.061	0.058
5.98	31.8	0.112	0.089	0.062	0.062
5.98	33.9	0.118	0.092	0.068	0.068
5.98	36.1	0.123	0.098	0.069	0.070

Table A1.7. Temperature Dependent fit parameters for CTC solutions dissolved in Chlorobenzene according to Equation 3.3 in the text.

Temperature (K)	K_{CT} (M^{-1})	ε (cm^{-1} M^{-1})
294	1.53×10^3	5.93×10^3
308	1.78×10^3	4.25×10^3
328	2.44×10^3	2.55×10^3
338	3.99×10^3	1.99×10^3

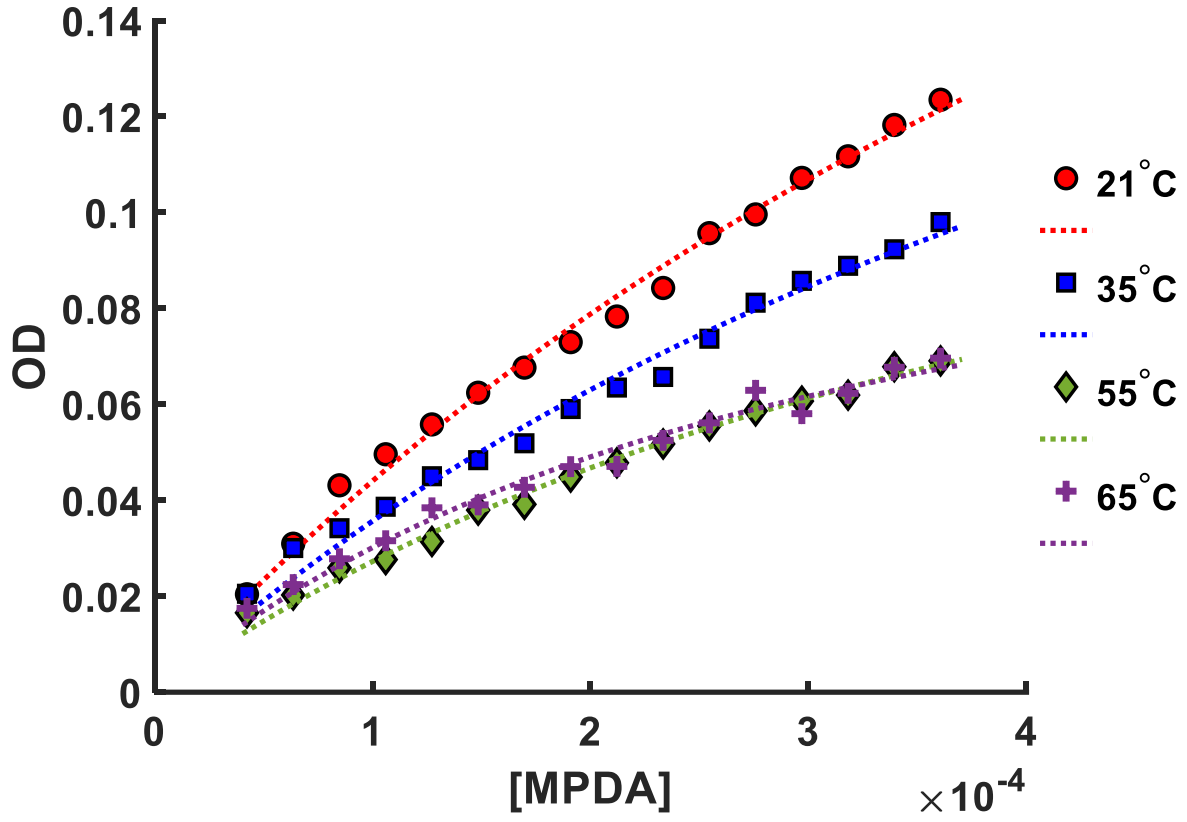

Figure A1.5. Temperature dependent curves for $F_4TCNQ^{\cdot -}$:$MPDA^+$ CTC's dissolved in Chlorobenzene according to Equation 3.3 in the text and fit to the data provided in Table A1.6.

Table A1.8. Donor and acceptor concentrations for samples dissolved in Chloroform with corresponding absorbance at 750 nm. Measurements collected at labeled temperatures.

[F_4TCNQ] × 10^{-5} (M)	[MPDA] × 10^{-5} (M)	OD R.T.	OD 30°C	OD 35°C
2.94	3.06	0.145	0.101	0.088
2.94	4.09	0.184	0.129	0.110
2.94	5.11	0.212	0.151	0.130
2.94	6.13	0.239	0.174	0.148
2.94	7.15	0.265	0.195	0.169
2.94	8.17	0.292	0.216	0.188
2.94	9.19	0.307	0.232	0.200
2.94	10.2	0.331	0.248	0.216
2.94	11.2	0.349	0.266	0.233
2.94	12.3	0.369	0.282	0.245
2.94	13.3	0.390	0.307	0.260
2.94	14.3	0.401	0.308	0.273
2.94	15.3	0.420	0.322	0.281
2.94	16.3	0.433	0.337	0.299
2.94	17.4	0.448	0.348	0.311

Table A1.9. Temperature Dependent fit parameters for CTC solutions dissolved in Chloroform according to Equation 3.3 in the text.

Temperature (K)	K_{CT} (M^{-1})	ε (cm^{-1} M^{-1})
294	8.66×10^3	2.61×10^4
303	6.02×10^3	2.40×10^4
308	5.23×10^3	2.28×10^4

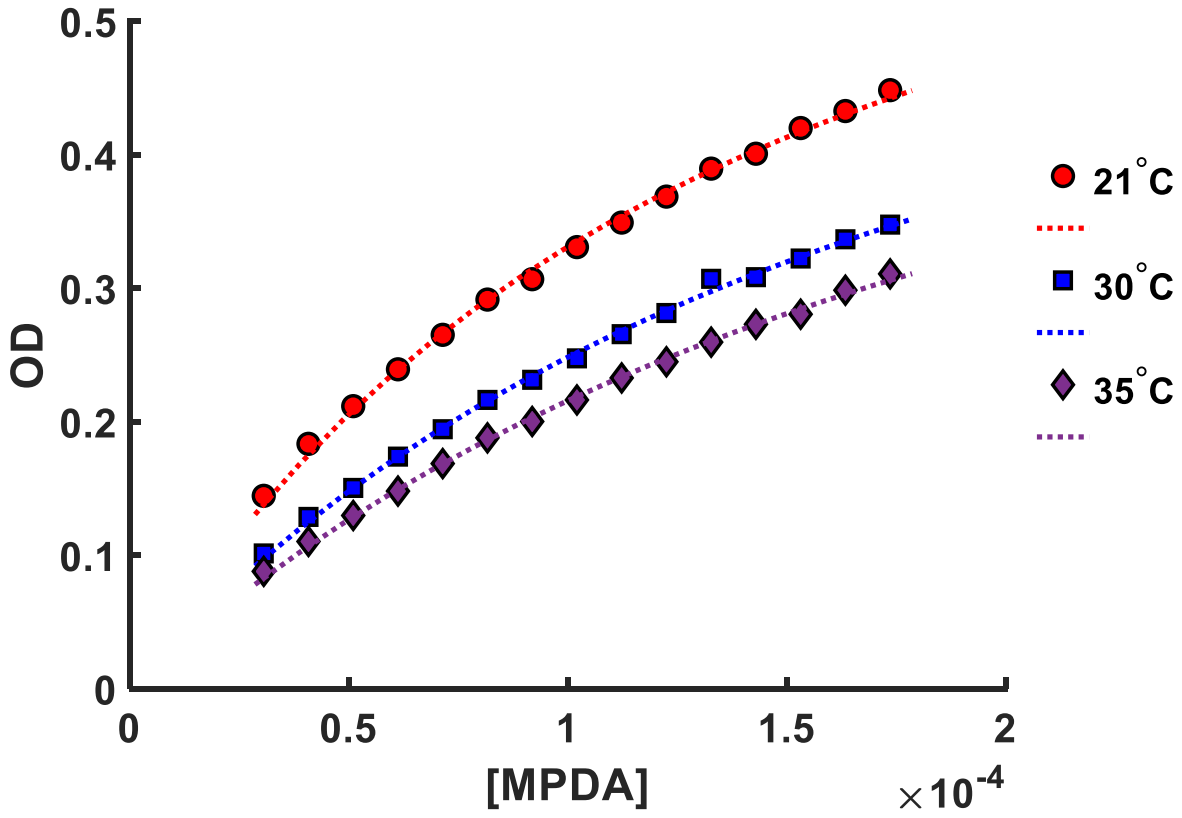

Figure A1.6. Temperature dependent curves for $F_4TCNQ^{\cdot -}$:$MPDA^+$ CTC's dissolved in Chloroform according to Equation 3.3 in the text and fit to the data provided in Table A1.7.

Appendix 2

Supporting Information for Chapter 4

Spectroscopic Studies of Charge-Transfer Character and Photoresponses of F_4TCNQ-based Donor-Acceptor Complexes

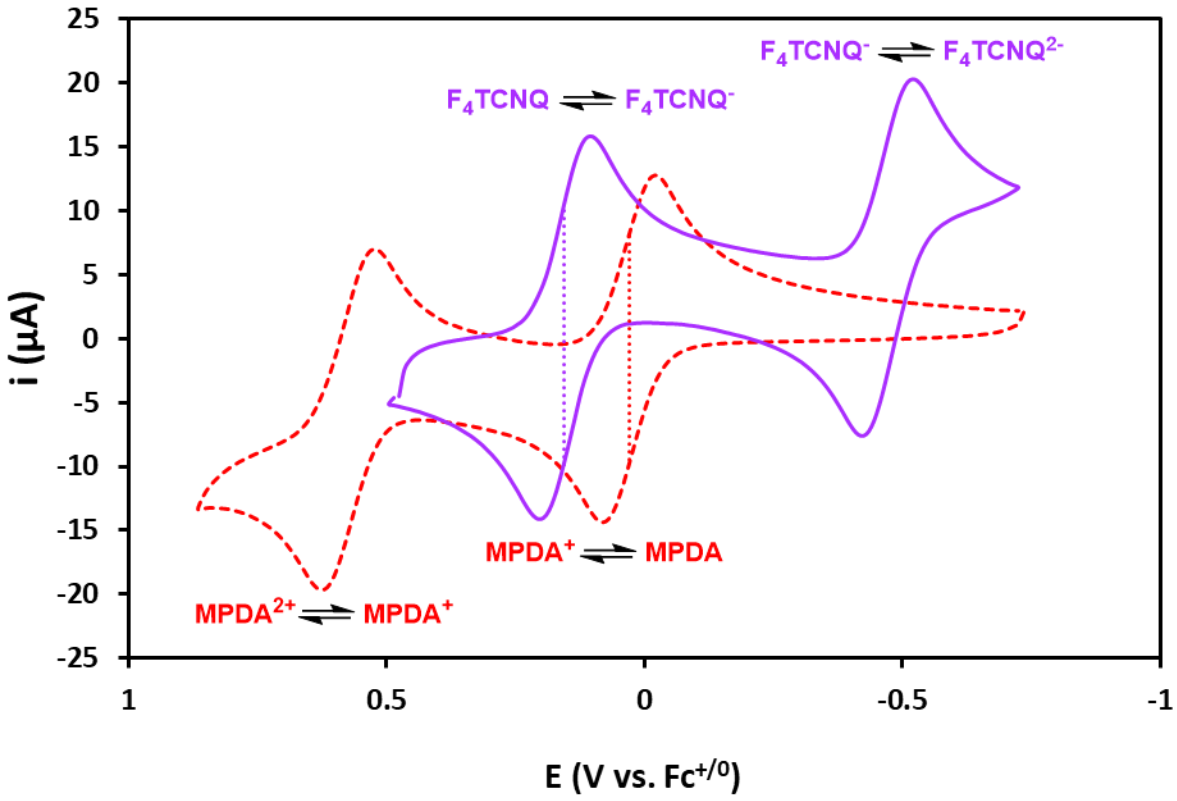

Figure A2.1. Cyclic voltammograms of 1 mM F_4TCNQ (purple) and 1 mM MPDA (red dashed) in dichloroethane, under N_2 atmosphere, with 100 mM $TBAPF_6$ as supporting electrolyte. $E_{1/2}$ values relevant to charge transfer to generated CTCs are indicated with dotted lines.

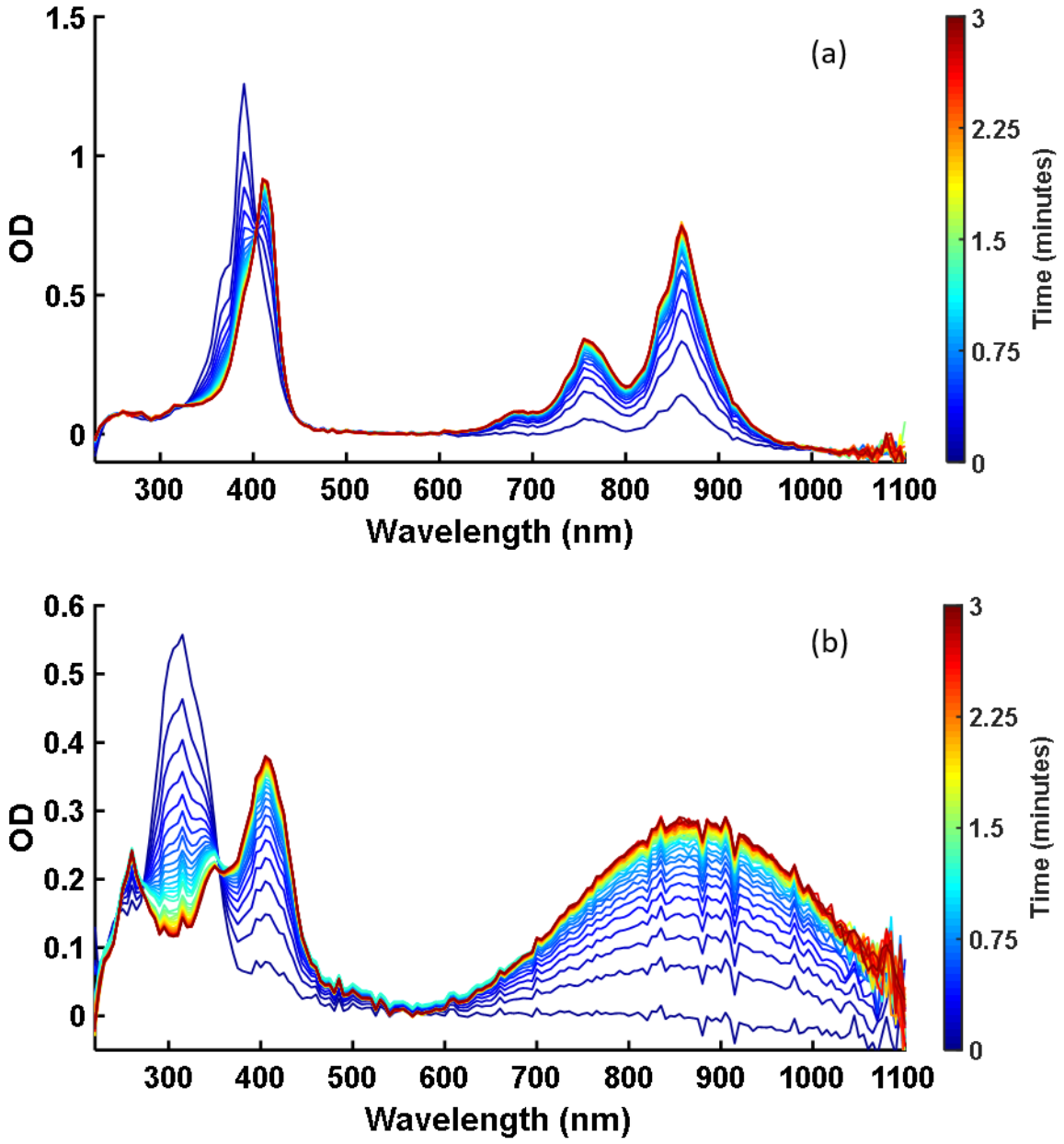

Figure A2.2. Spectroelectrochemistry of (a) F_4TCNQ (0.13 mM) and (b) MPDA (0.092 mM) dissolved in dichloroethane under controlled potential electrolysis (CPE) for 3 min. CPE was conducted at -0.150 and 0.220 V vs. Fc/Fc^+, respectively, both of which result in nearly complete conversion to the corresponding anion and cation species, respectively, on this timescale.

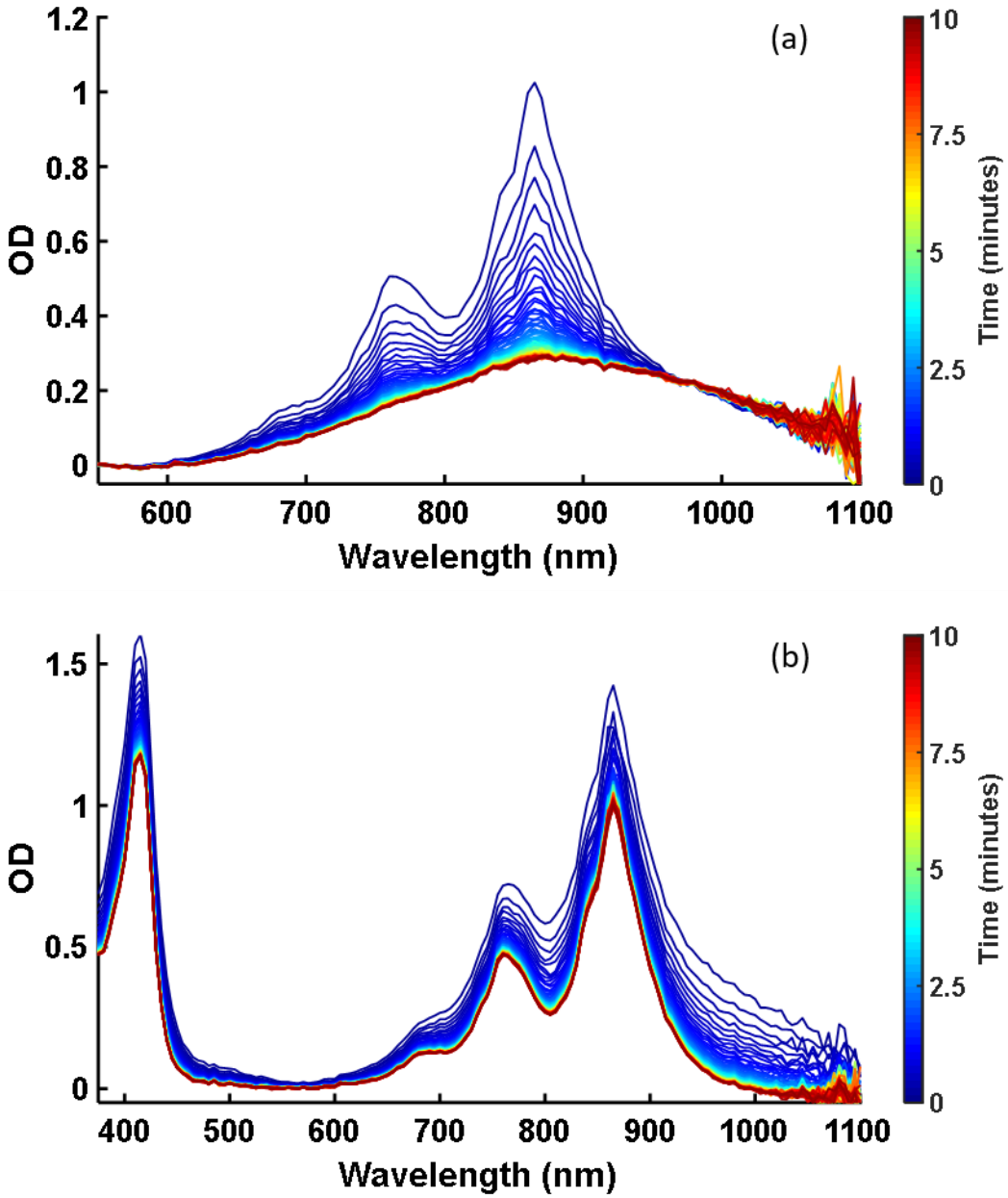

Figure A2.3. Spectroelectrochemistry of CT complexes dissolved in dichloroethane. (a) 0.091 mM MPDA with excess F_4TCNQ and (b) 0.12 mM F_4TCNQ with excess MPDA under controlled potential electrolysis for 10 min. CPE was conducted at 0.410 and -0.090 V vs. Fc/Fc^+, respectively, both of which result in neutralizing the corresponding anion or cation species, respectively, on this timescale. These confirm that the extinction of $F_4TCNQ^{\cdot -}$ is roughly twice that of $MPDA^+$ at 750 nm.

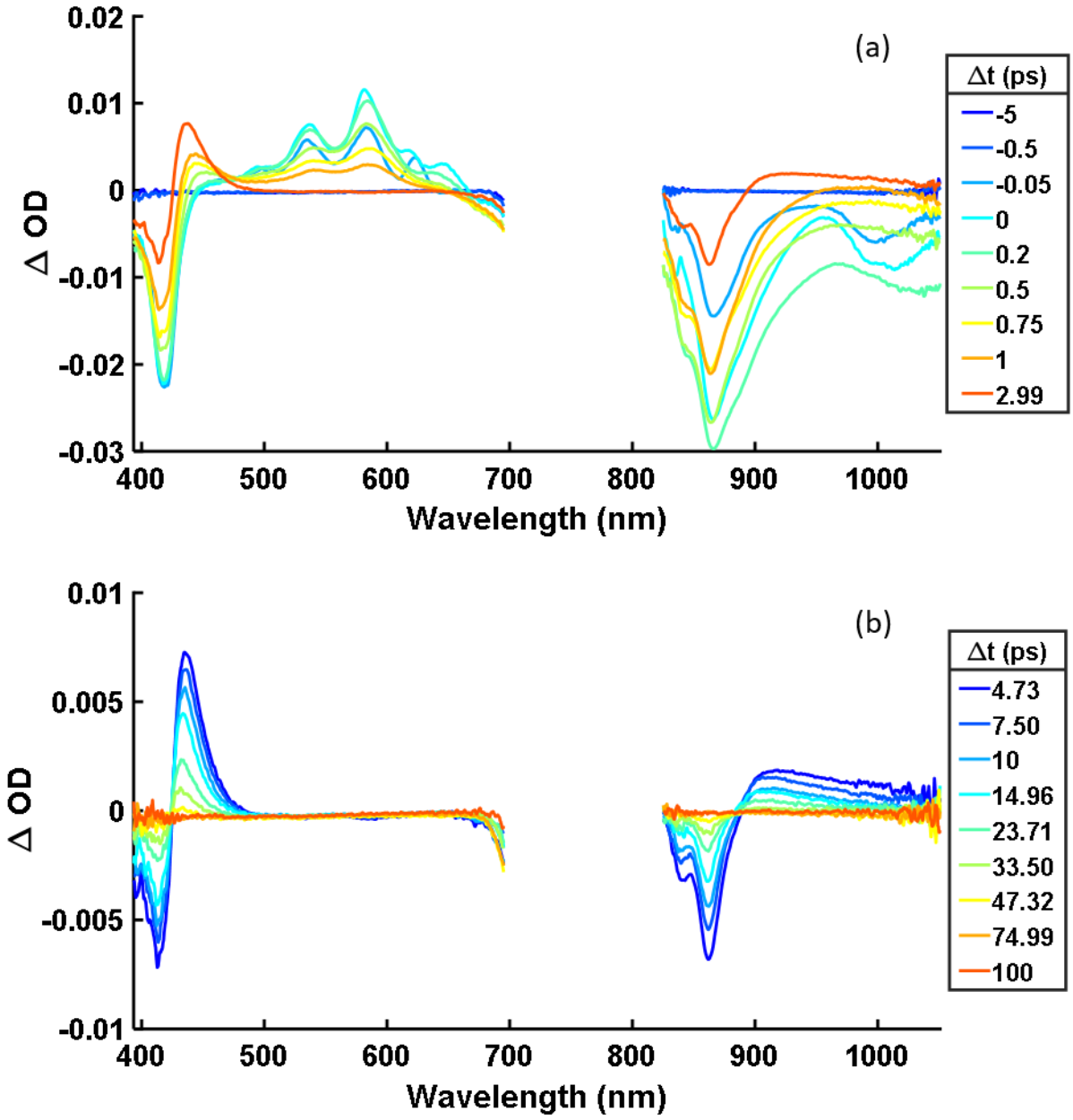

Figure A2.4. Transient absorption spectra of $F_4TCNQ^{\cdot -}$ in dichloroethane excited at 750 nm. $F_4TCNQ^{\cdot -}$ was generated by controlled potential electrolysis at -0.310 V vs. Fc/Fc+. Transient absorption spectra (a) before and (b) after 3 ps.

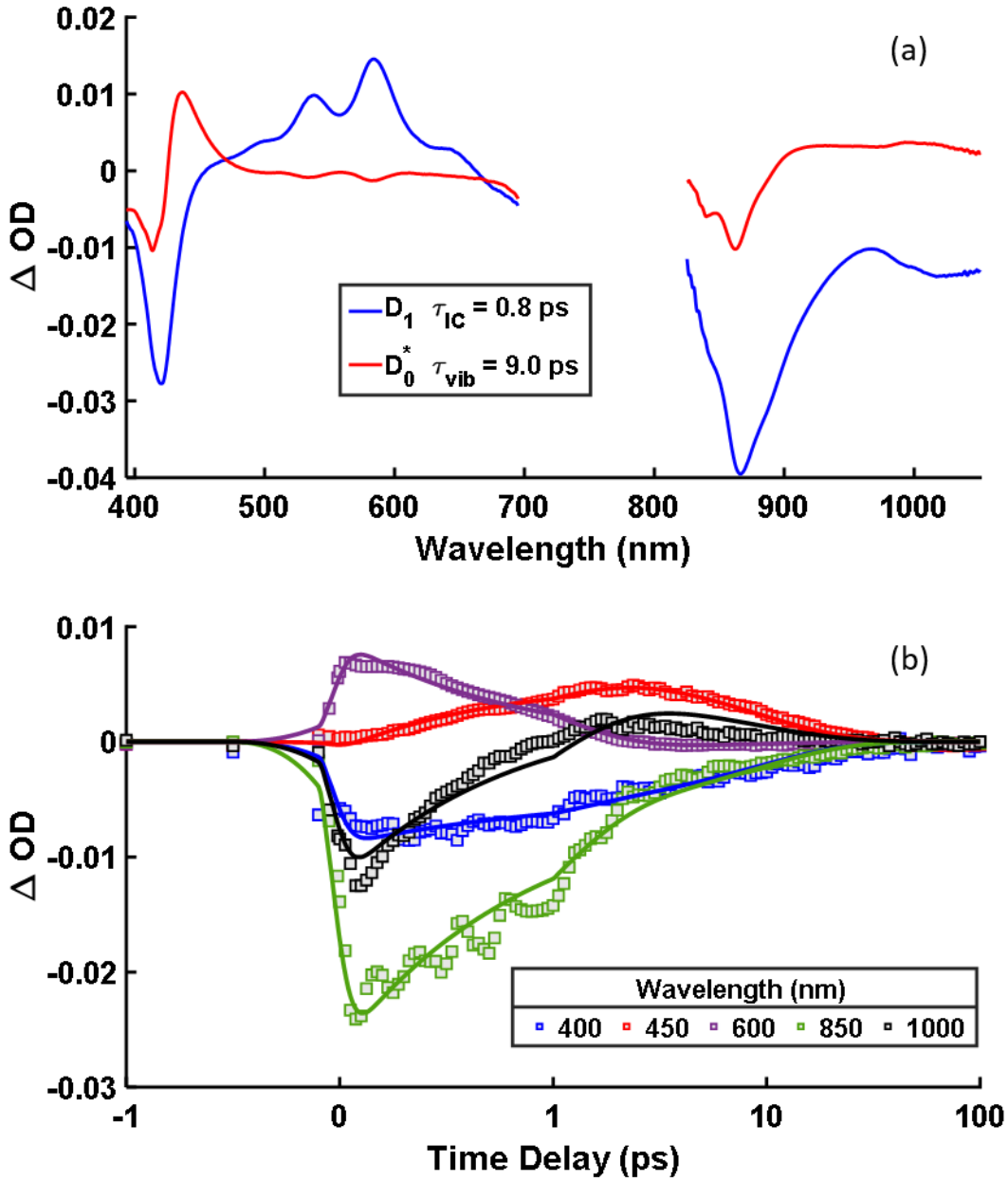

Figure A2.5. Global analysis of transient absorption spectra in Figure A2.4, obtained with $F_4TCNQ^{\cdot -}$ in dichloroethane excited at 750 nm. $F_4TCNQ^{\cdot -}$ was generated by controlled potential electrolysis at -0.310 V vs. Fc/Fc+. (a) Species associated spectra and (b) selected fits to kinetic traces from global analysis.

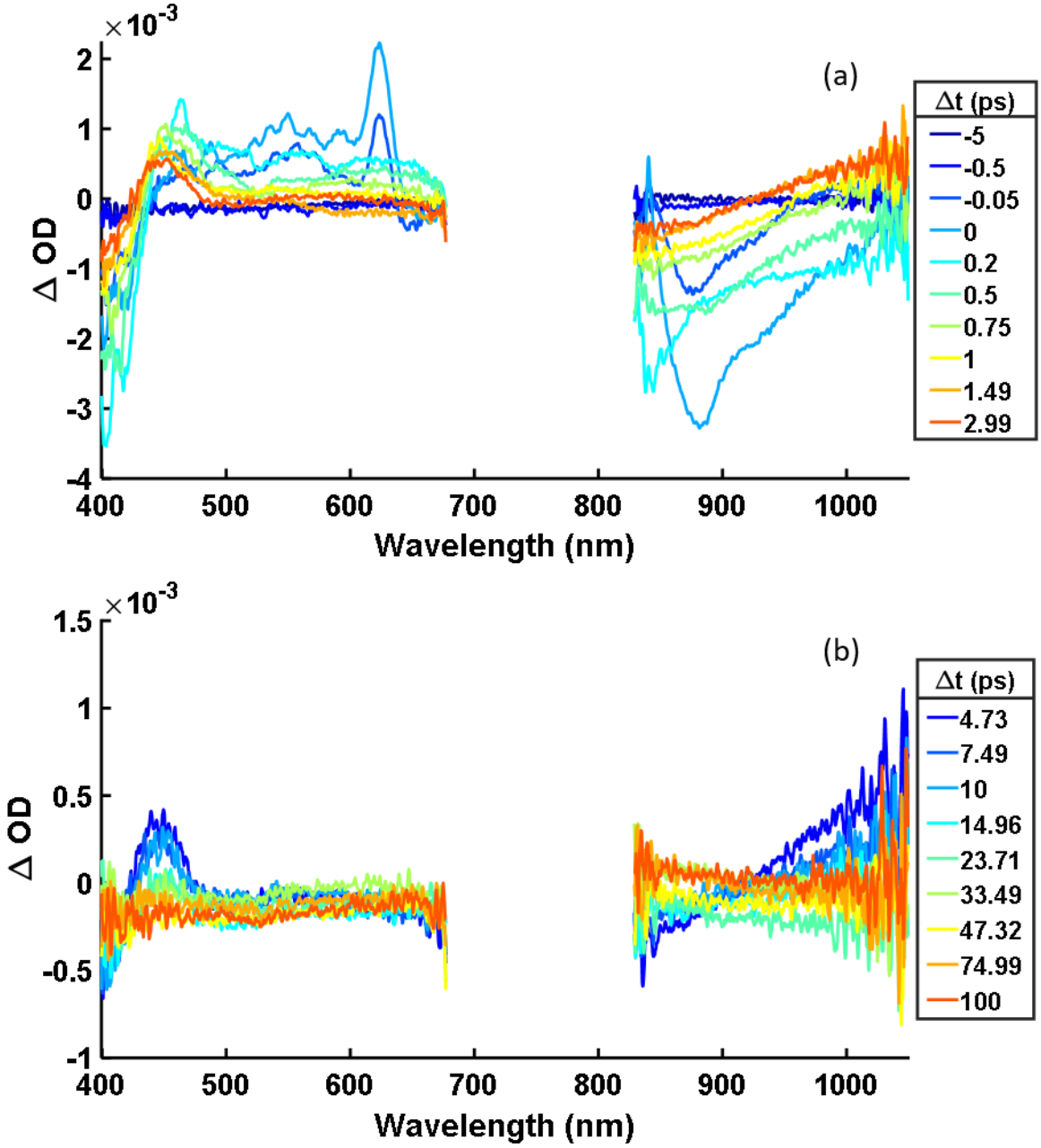

Figure A2.6. Transient absorption spectra of $MPDA^+$ in dichloroethane excited at 750 nm. $MPDA^+$ was generated by controlled potential electrolysis at 0.190 V vs. Fc/Fc+. Transient absorption spectra (a) before and (b) after 3 ps.

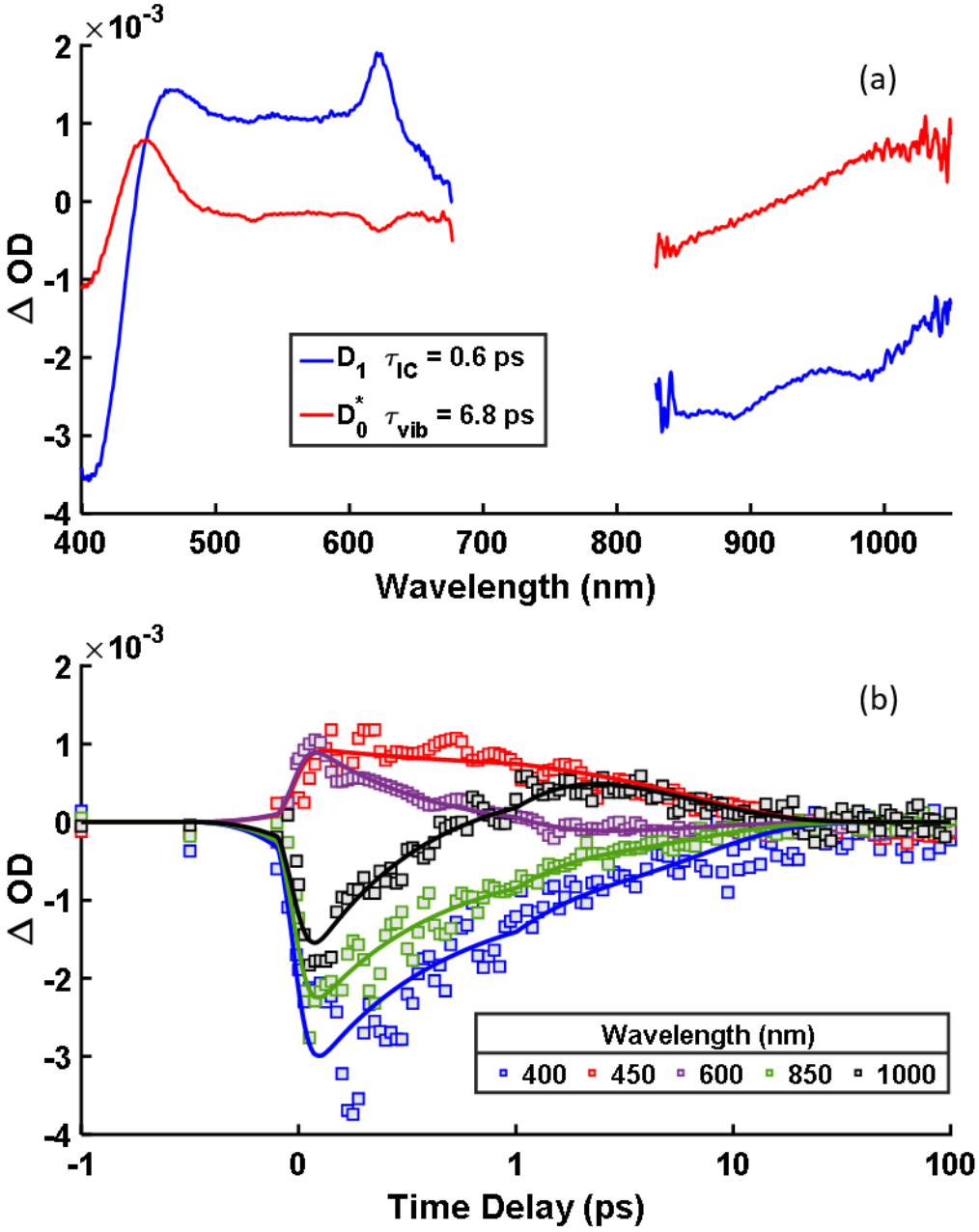

Figure A2.7. Global analysis of transient absorption spectra in Figure A2.6 obtained with $MPDA^+$ in dichloroethane excited at 750 nm. $MPDA^+$ was generated by controlled potential electrolysis at 0.190 V vs. Fc/Fc+. (a) Species associated spectra and (b) selected fits to kinetic traces from global analysis.

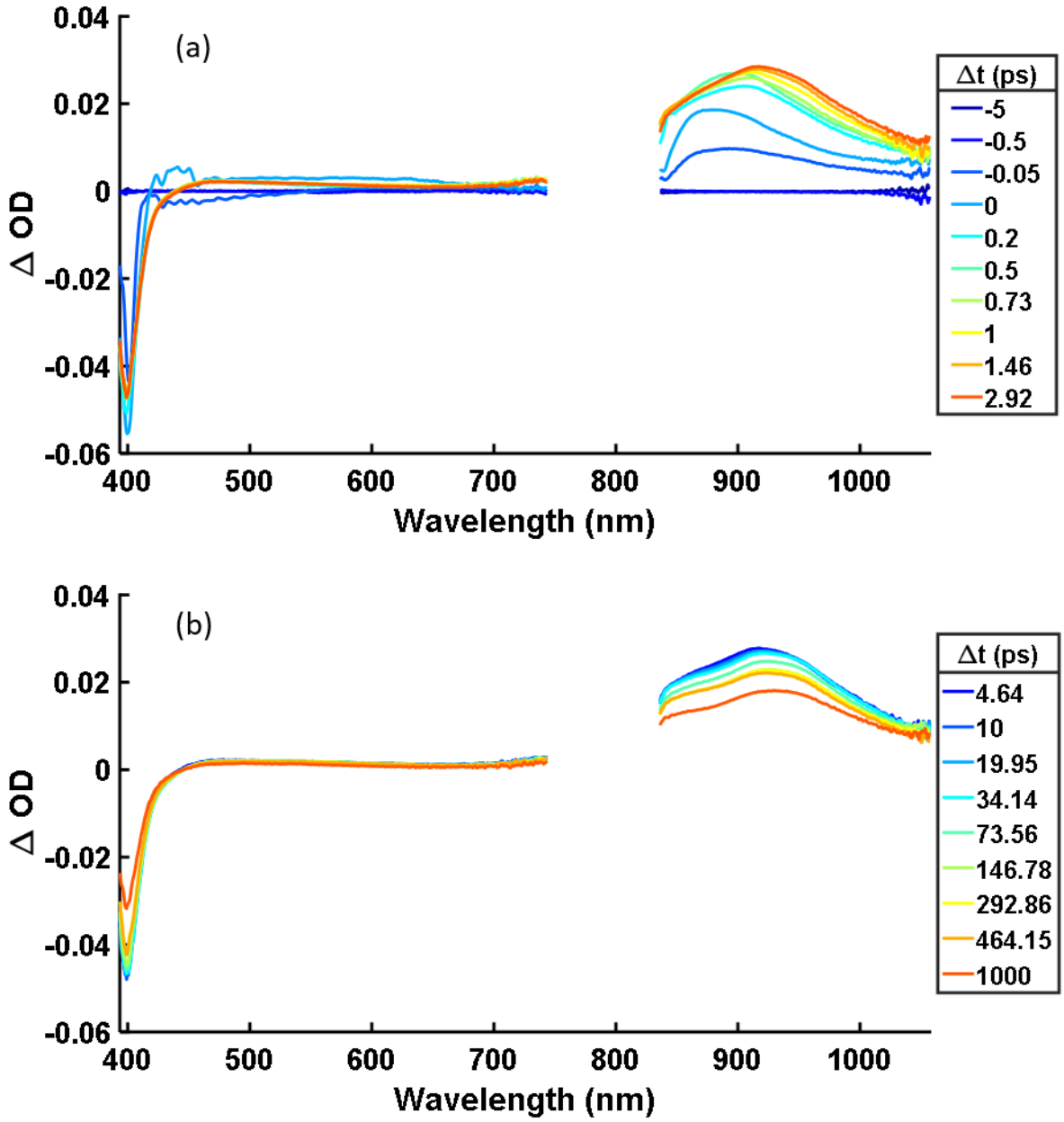

Figure A2.8. Transient absorption spectra of neutral F_4TCNQ dissolved in dichloroethane with 400-nm excitation. Transient absorption spectra (a) before and (b) after 3 ps.

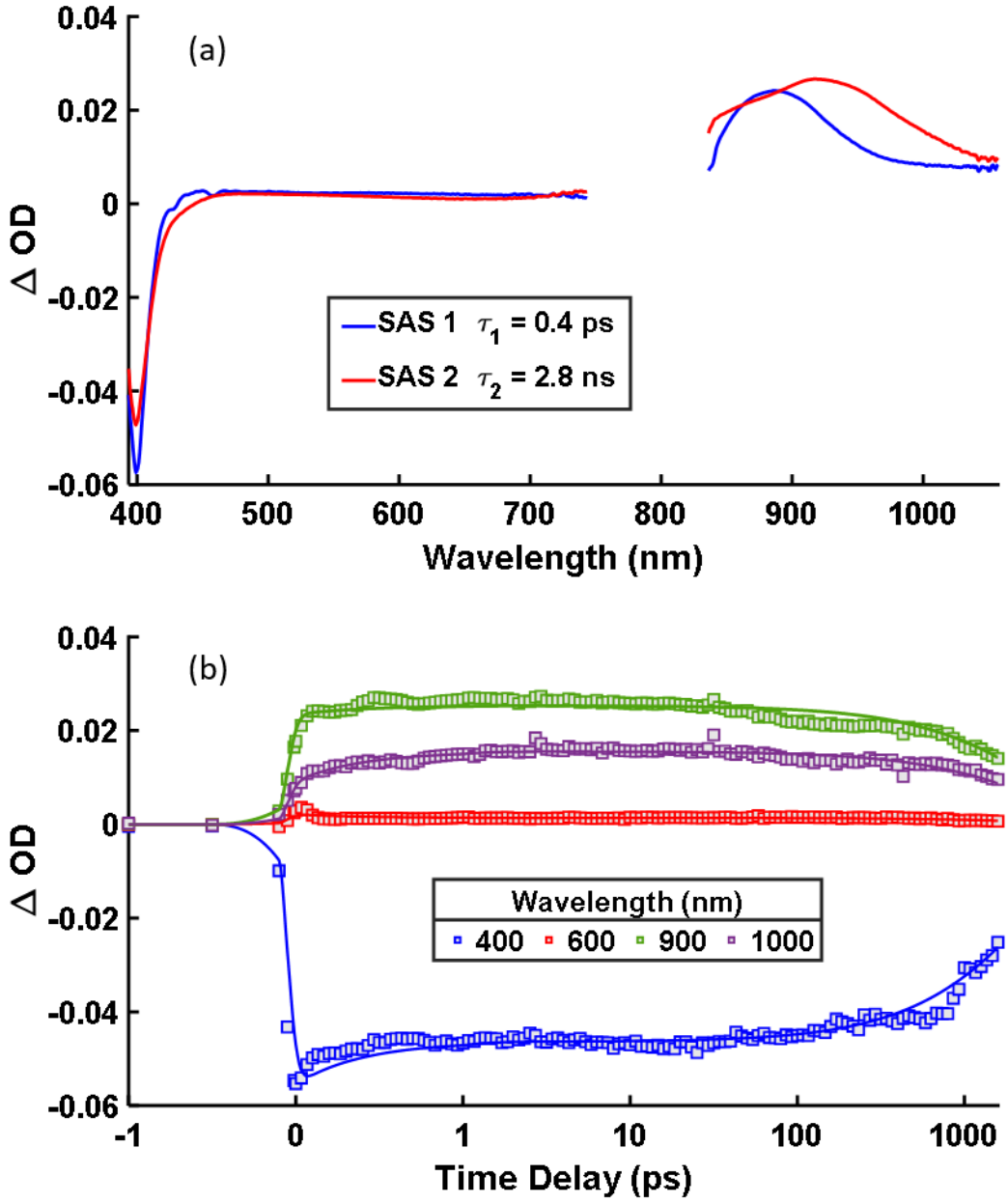

Figure A2.9. Global spectral analysis of transient absorption collected for neutral F_4TCNQ dissolved in dichloroethane with 400-nm excitation. (a) Species associated spectra and (b) selected fits to kinetic traces from global analysis.

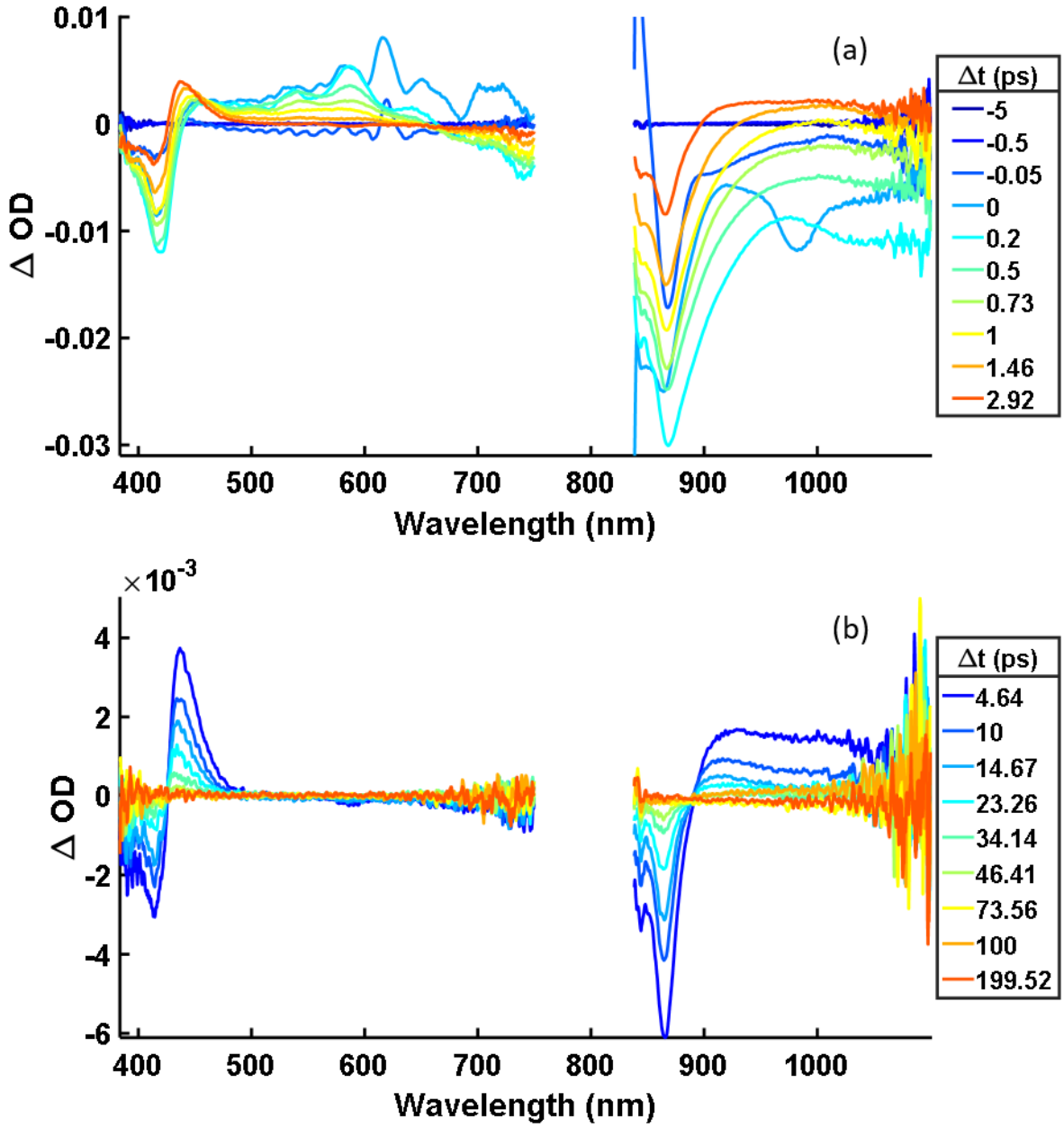

Figure A2.10. Transient absorption spectra of $F_4TCNQ^{\cdot-}$:PDA^+ dissolved in dichloroethane at 750 nm excitation. Transient absorption spectra (a) before and (b) after 3 ps.

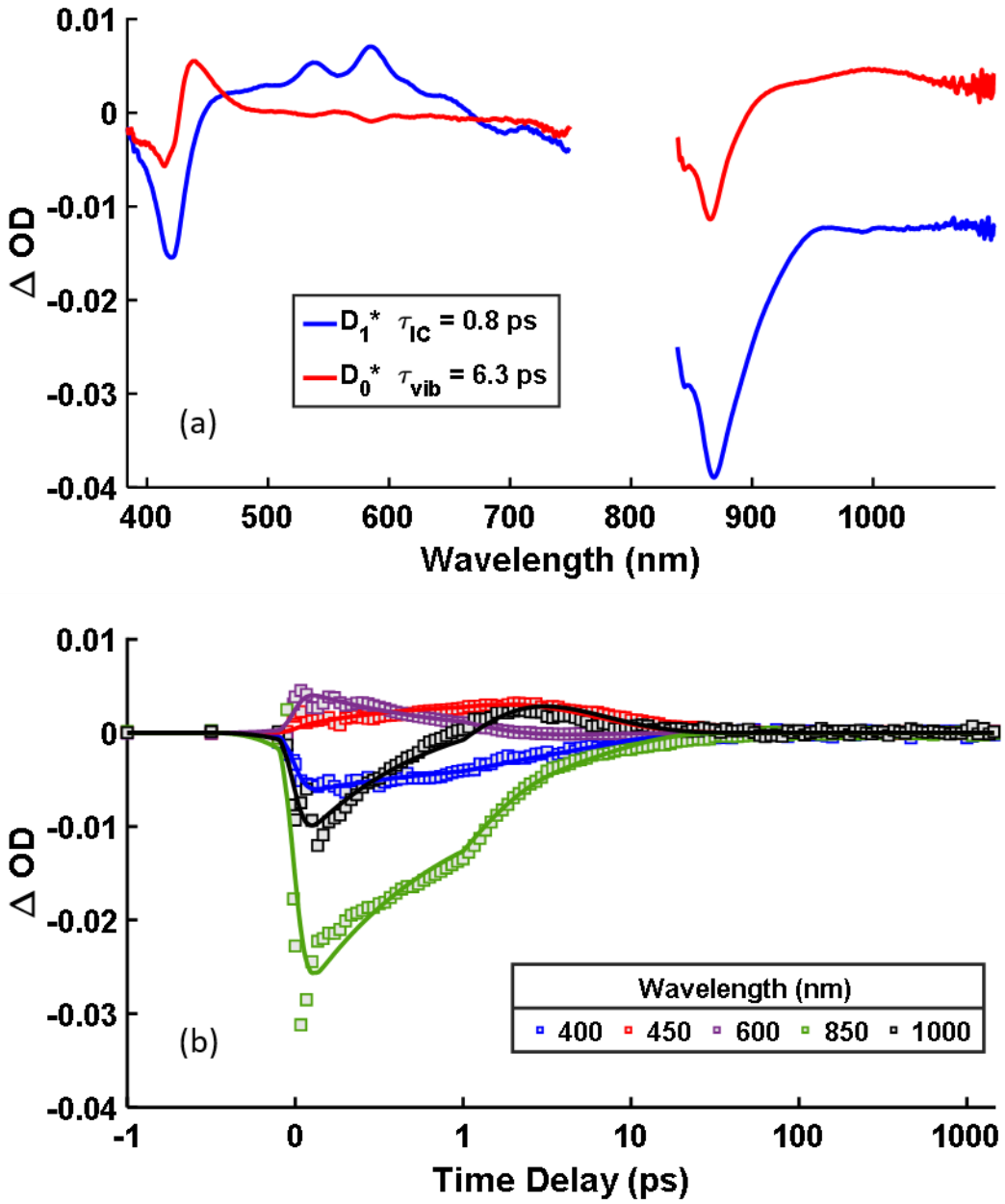

Figure A2.11. Global analysis of transient absorption spectra in Figure A2.10 collected for $F_4TCNQ^{\cdot-}$:PDA^+ dissolved in dichloroethane with 750 nm excitation. (a) Species associated spectra and (b) selected fits to kinetic traces from global analysis.

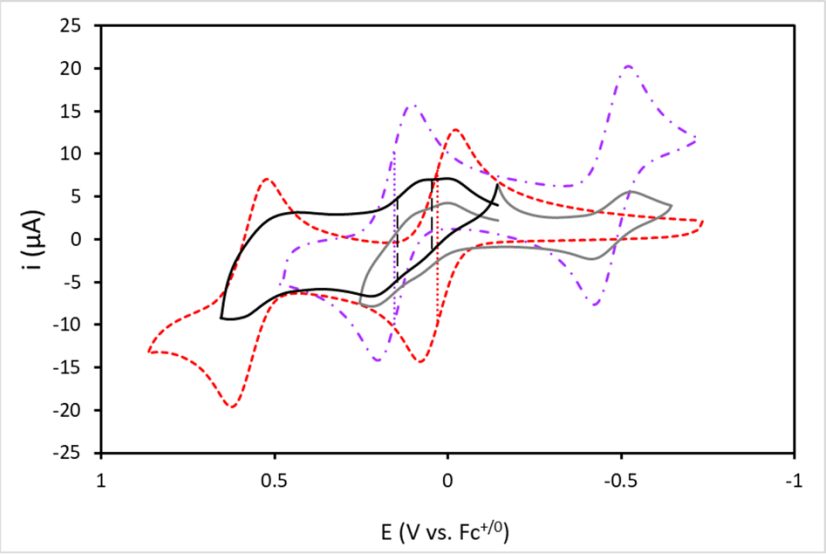

Figure A2.12. Comparison of CVs for MPDA, F_4TCNQ, and their CT complex. CVs for MPDA and F_4TCNQ taken with a glassy carbon electrode (red and purple) or their CTC taken with a Au honeycomb electrode (black and gray), in acetonitrile with 100 mM $TBAPF_6$ supporting electrolyte. The F_4TCNQ reduction potential shifts negatively between free F_4TCNQ and F_4TCNQ in a CTC (from 0.155 to 0.145 V, respectively); the $MPDA^+$ reduction potential shifts positively between free $MPDA^+$ and $MPDA^+$ in a CTC (0.030 to 0.045 eV, respectively). $E_{1/2}$ values were determined from the derivative of CVs for CTCs. These voltammetric shifts indicate the presence of an ion-pair binding interaction.

Appendix 3

Supporting Information for Chapter 5

Intramolecular Photoinduced Charge Transfer and Recombination Dynamics in Vinylarene Terminated Organosilanes

Transient absorption and steady-state emission data and analysis for Si2s-2E, Si4s-2E, Si2s-2C, and Si4s-2C organosilanes

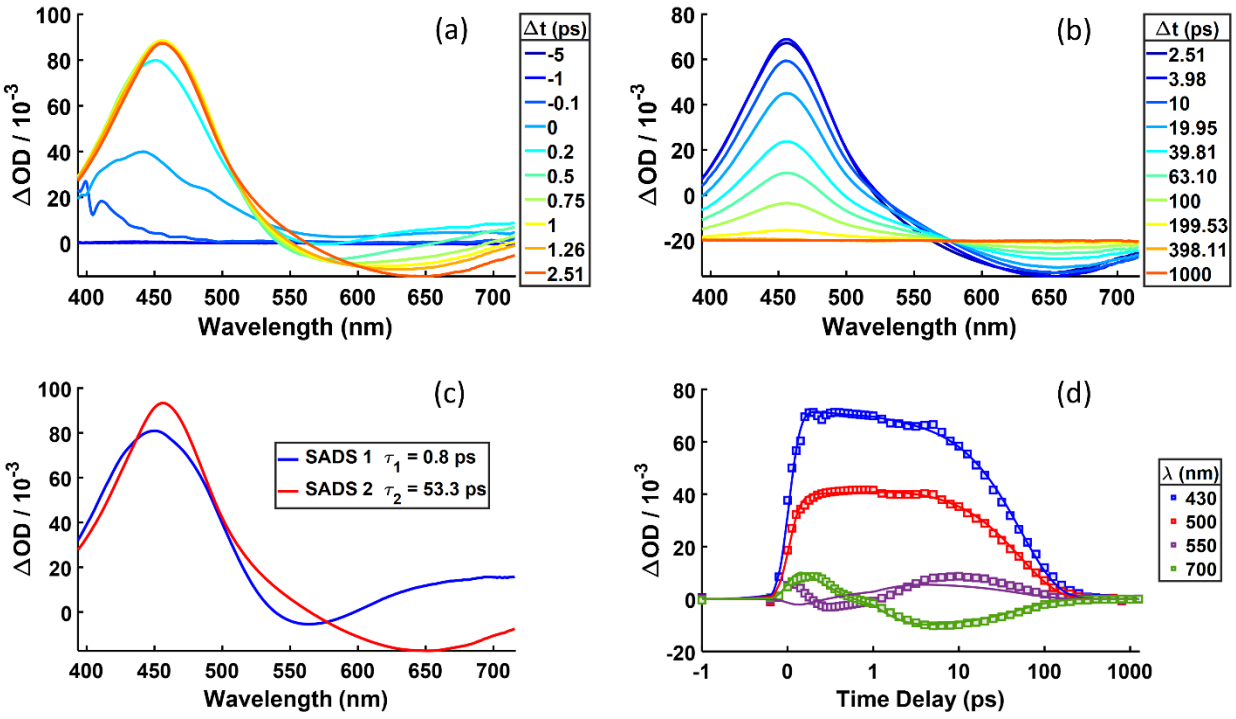

Figure A3.1. Transient absorption of **Si4s-2E** dissolved in DCM excited at 360 nm (a) before and (b) after 3 ps. (c) species associated difference spectra and (d) temporal traces at selected probe wavelengths plotted with fits, obtained from global analysis with the kinetic model presented in Equation 5.2 in the main text.

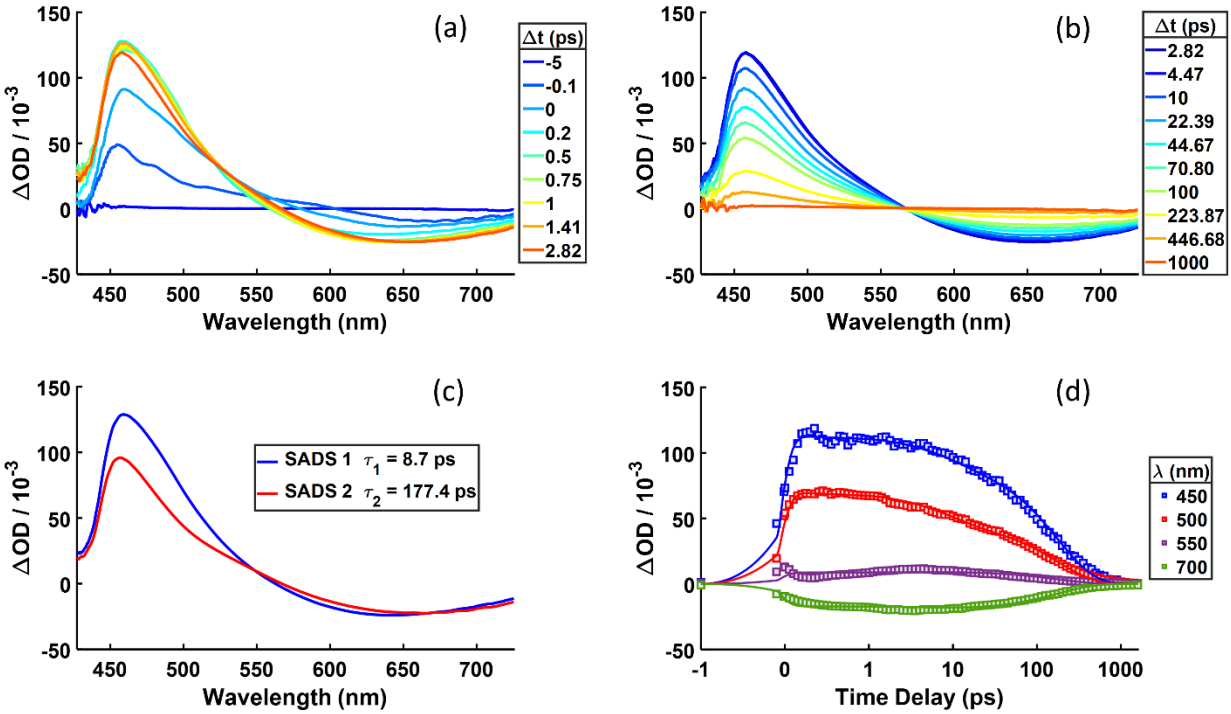

Figure A3.2. Transient absorption of **Si4s-2C** dissolved in DCM excited at 360 nm (a) before and (b) after 3 ps. (c) species associated difference spectra and (d) temporal traces at selected probe wavelengths plotted with fits, obtained from global analysis with the kinetic model presented in Equation 5.2 in the main text.

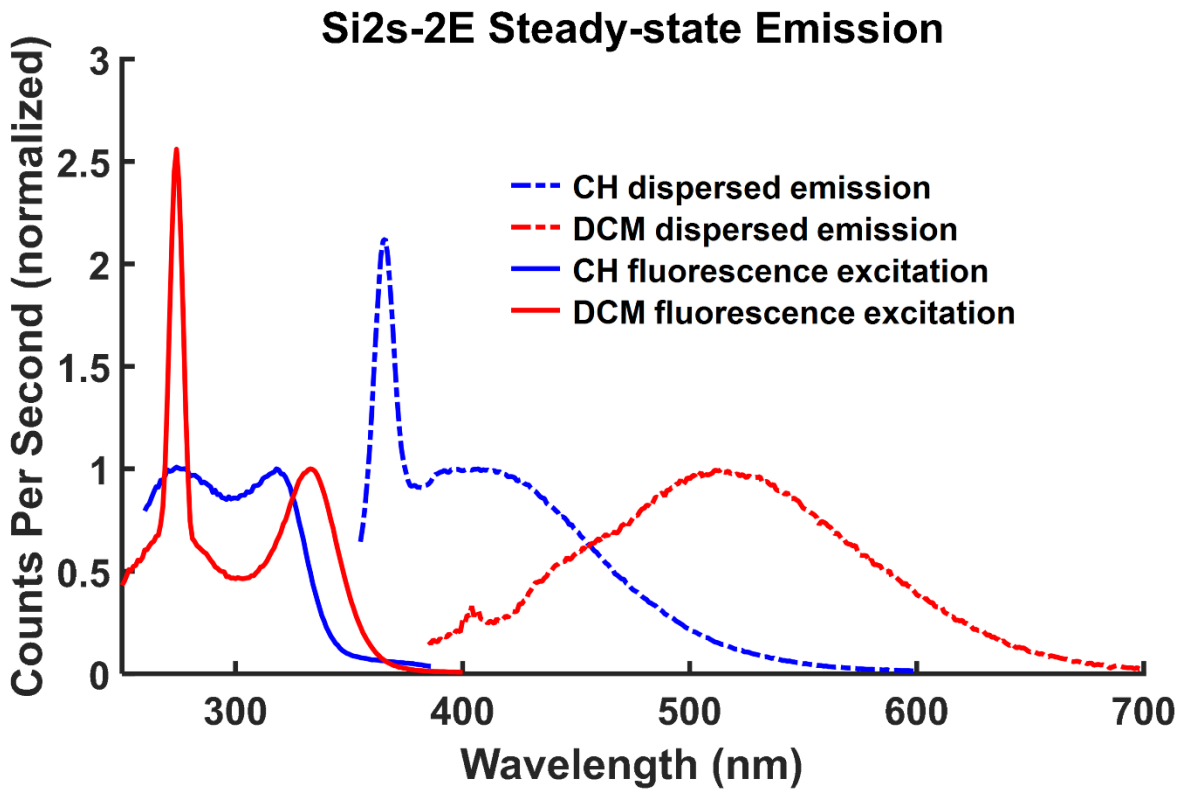

Figure A3.3. Steady-state emission spectra of **Si2s-2E** dissolved in cyclohexane (dispersed emission shown in dashed blue, fluorescence excitation shown in solid blue) and dichloromethane (dispersed emission shown in dashed red, fluorescence excitation shown in solid red).

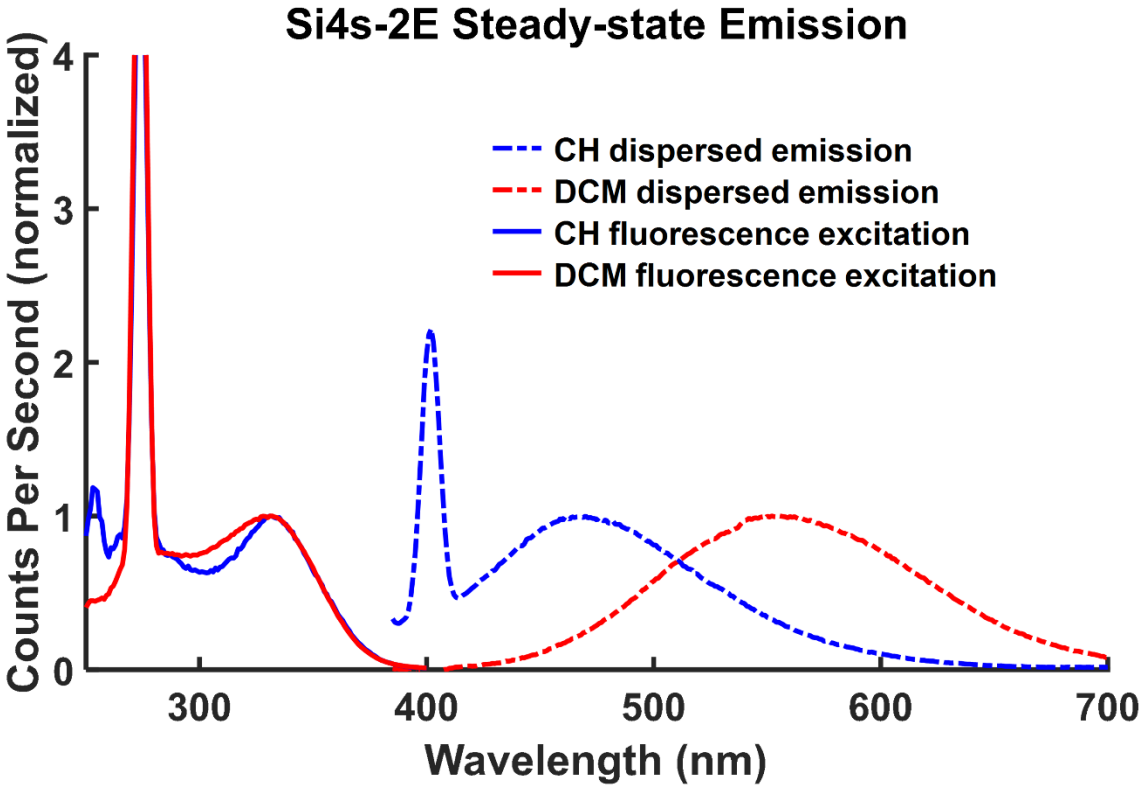

Figure A3.4. Steady-state emission spectra of **Si4s-2E** dissolved in cyclohexane (dispersed emission shown in dashed blue, fluorescence excitation shown in solid blue) and dichloromethane (dispersed emission shown in dashed red, fluorescence excitation shown in solid red).

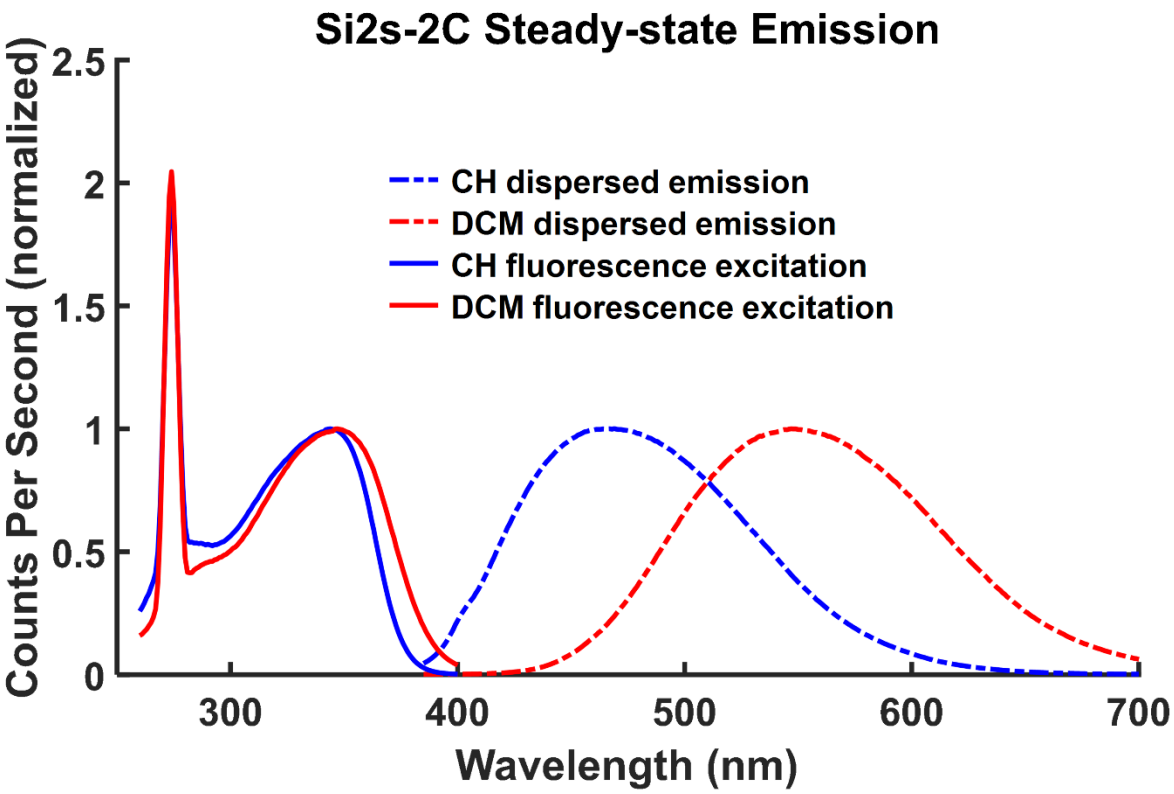

Figure A3.5. Steady-state emission spectra of **Si2s-2C** dissolved in cyclohexane (dispersed emission shown in dashed blue, fluorescence excitation shown in solid blue) and dichloromethane (dispersed emission shown in dashed red, fluorescence excitation shown in solid red).

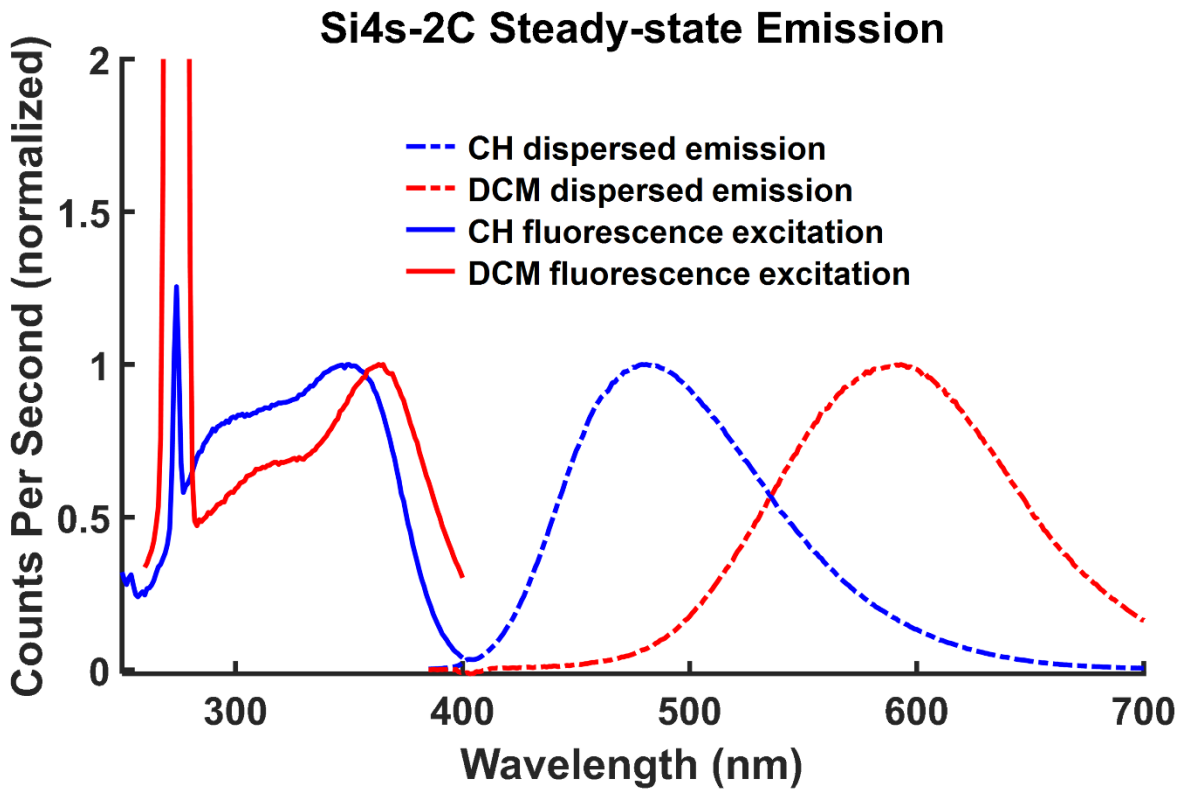

Figure A3.6. Steady-state emission spectra of **Si4s-2C** dissolved in cyclohexane (dispersed emission shown in dashed blue, fluorescence excitation shown in solid blue) and dichloromethane (dispersed emission shown in dashed red, fluorescence excitation shown in solid red).

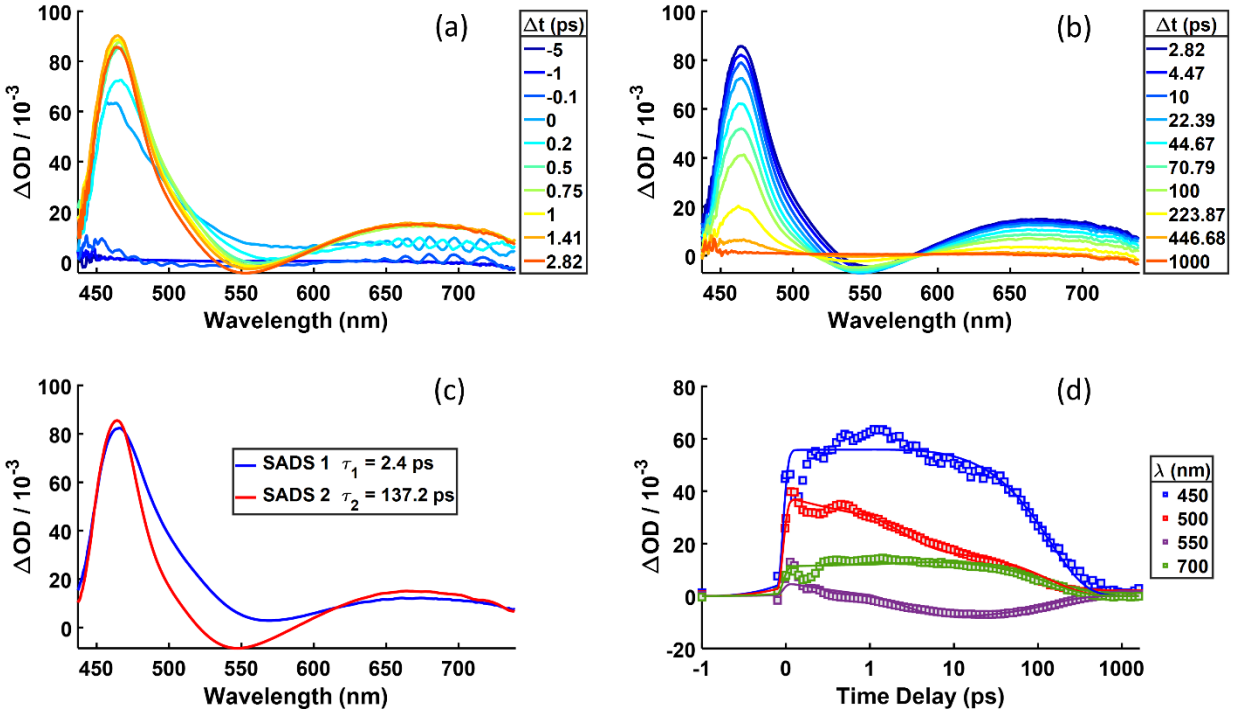

Figure A3.7. Transient absorption of **Si2s-2C** dissolved in CH excited at 360 nm (a) before and (b) after 3 ps. (c) species associated difference spectra and (d) temporal traces at selected probe wavelengths plotted with fits, obtained from global analysis with the kinetic model presented in Equation 5.2 in the main text.

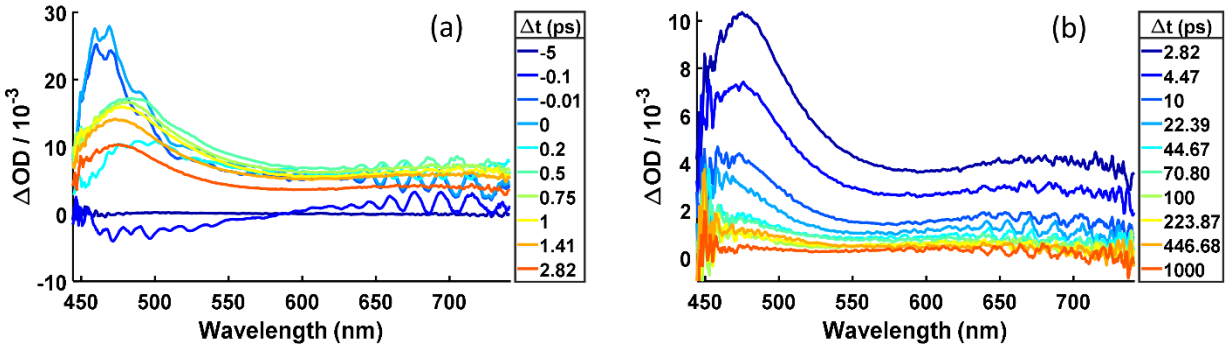

Figure A3.8. Transient absorption of **Si4s-2E** dissolved in CH excited at 360 nm (a) before and (b) after 3 ps.

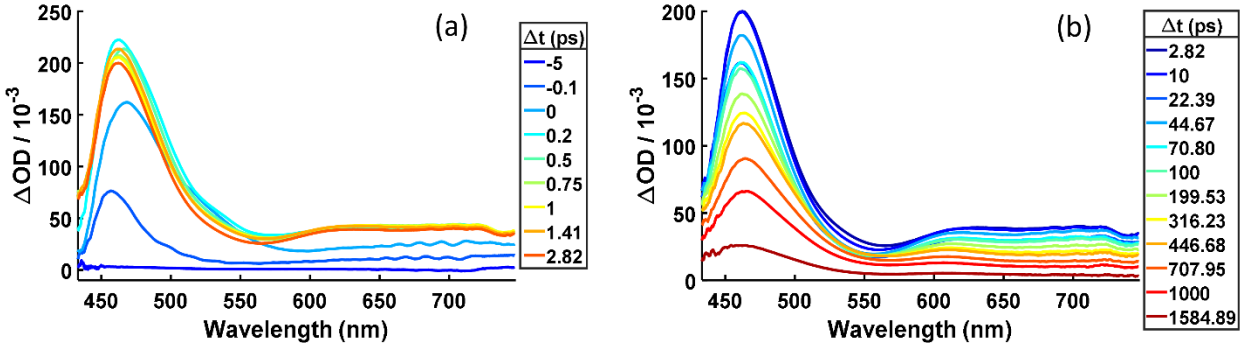

Figure A3.9. Transient absorption of **Si4s**-2C dissolved in CH excited at 360 nm (a) before and (b) after 3 ps.

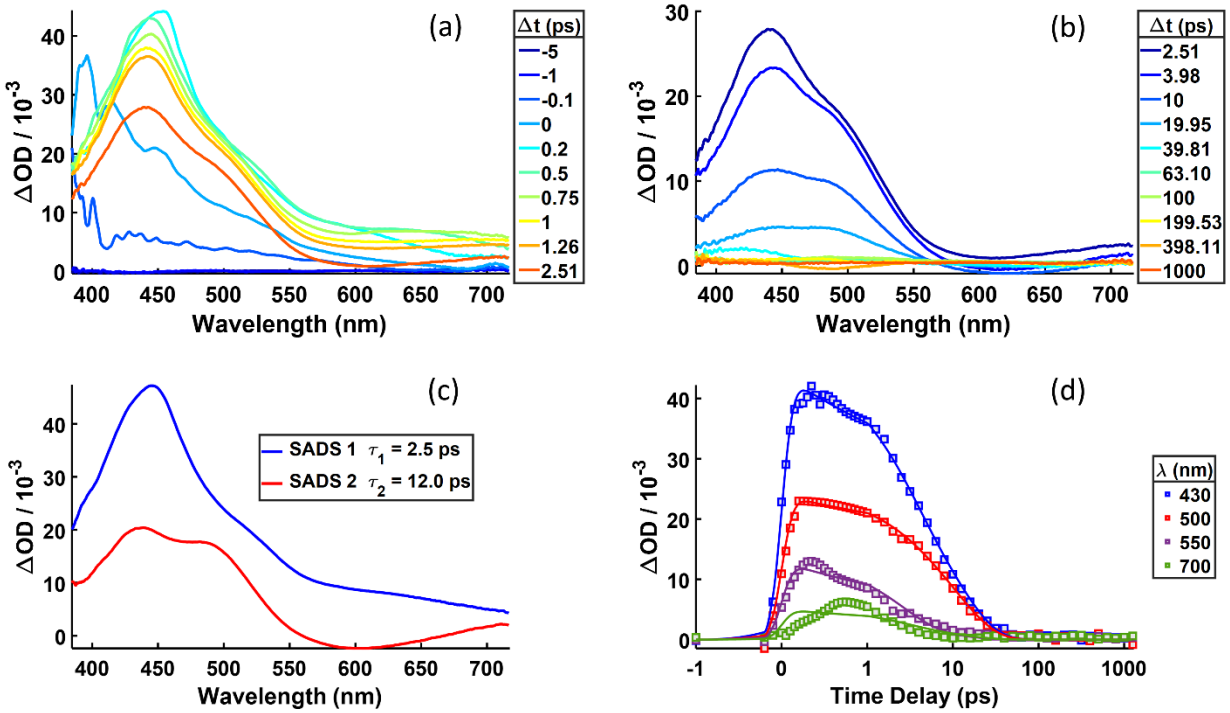

Figure A3.10. Transient absorption of **Si2s-2E** dissolved in $CHCl_3$ excited at 360 nm (a) before and (b) after 3 ps. (c) species associated difference spectra and (d) temporal traces at selected probe wavelengths plotted with fits, obtained from global analysis with the kinetic model presented in Equation 5.2 in the main text.

Independent estimations of solvent reorganization energies from Lippert analysis of solvent-dependent emission (Si2s-E,C and Si4s-E,C).

We obtained and analyzed emission and absorption data for the **E,C** end-capped compounds in various solvents as part of previously published work.[1] We used a Lippert analysis of this data to assess the difference in dipole moment ($\Delta\mu$) in the excited vs. ground states of these molecules; this involves fitting the emission Stokes' shift ($\Delta\overline{\nu}$) as a linear function of the solvent orientation polarizability Δf:[2-3]

$$\Delta\overline{\nu} = \frac{2\Delta\mu^2\Delta f}{hca^3} + \Delta\overline{\nu}_0 \qquad \text{(A3.1a)}$$

$$\Delta f = \frac{\varepsilon - 1}{2\varepsilon + 1} - \frac{n^2 - 1}{2n^2 + 1} \qquad \text{(A3.1b)}$$

Here a denotes the radius of the solvation cavity, ε is the static dielectric constant of the solvent and n is the solvent's refractive index. For dipolar solvation, which is expected in the formation of a intramolecular charge-separated state, the solvent reorganization energy can be approximated by the first term in Equation A3.1a. For DCM, Δf=0.217. The slopes of our Lippert plots for **Si2s-E,C** and **Si4s-E,C** were 6990 ± 1730 and 6880 ± 2710, respectively. We therefore estimate solvent reorganization energies of 0.19 ± 0.05 eV and 0.19 ± 0.07 eV, which are comparable to the values estimated from our analyses presented in the text with the larger set of organosilane structures. We note that in the Lippert analysis we used the absorption onset in our calculation of the Stokes' shift, rather than the peak of the fluorescence excitation we use in the rate analyses presented here; this should not impact the slopes of best fit lines used to determine the solvation energy (only the intercepts).

For an emissive charge-separated state, we can also estimate the solvent reorganization energy from the difference in peak emission in DCM vs. CH.[3] This approach similarly assumes that the solvent reorganization energy in CH is negligible and corrects for contributions from intramolecular reorganization energy (which are assumed the same in the two solvent environments). Using the peak emission energies presented in Table 5.2, this approach predicts solvent reorganization energies of 0.317, 0.196, 0.243, and 0.194 eV for **Si2s-2E**, **Si4s-2E**, **Si4s-2C** and **Si2s-2C**, respectively. There is no obvious trend in solvent reorganization with structure with an average value of 0.24 ± 0.06 eV across the set of compounds. [0.21 ± 0.02 eV if you exclude **Si2s-2E**; the value for **Si2s-2E** is an outlier, possibly due to the difficulty of assessing the emission peak position in CH, see Figure A3.3.] In contrast, if we use the total and intramolecular reorganization energies reported in Table 5.2 of the main text, we obtain solvent reorganization energies of 0.229, 0.190, 0.180, and 0.179 eV for **Si2s-2E**, **Si4s-2E**, **Si4s-2C** and **Si2s-2C**, respectively (average of 0.19 ± 0.02 eV).

In total, these various estimations of solvent-reorganization energies reflect internal consistency in the estimations of total and intramolecular reorganization energies presented in the text for our BET rate analyses.

References

1. Zhou, J. W.; Folster, C. P.; Surampudi, S. K.; Jimenez, D.; Klausen, R. S.; Bragg, A. E., Asymmetric Charge Separation and Recombination in Symmetrically Functionalized Sigma-Pi Hybrid Oligosilanes. *Dalton Trans.* **2017**, *46*, 8716-8726.

2. Lippert, E., Spektroskopische Bestimmung Des Dipolmomentes Aromatischer Verbindungen Im Ersten Angeregten Singulettzustand. *Ber. Bunsen. Phys. Chem.* **1957**, *61*, 962–975.

3. Solís, C.; Grosso, V.; Faggioli, N.; Cosa, G.; Romero, M.; Previtali, C.; Montejano, H.; Chesta, C., Estimation of the Solvent Reorganization Energy and the Absolute Energy of Solvation of Charge-Transfer States from Their Emission Spectra. *Photochem. Photobiol. Sci.* **2010**, *9*, 675-686.